Wind Turbine Wake in Atmospheric Turbulence

Rethore, Pierre-Elouan

Wind Turbine Wake
in Atmospheric Turbulence

PhD Thesis

Pierre-Elouan Réthoré

AALBORG UNIVERSITY

Department of Civil Engineering

Scientific Publications at the Department of Civil Engineering

Technical Reports are published for timely dissemination of research results and scientific work carried out at the Department of Civil Engineering (DCE) at Aalborg University. This medium allows publication of more detailed explanations and results than typically allowed in scientific journals.

Technical Memoranda are produced to enable the preliminary dissemination of scientific work by the personnel of the DCE where such release is deemed to be appropriate. Documents of this kind may be incomplete or temporary versions of papers—or part of continuing work. This should be kept in mind when references are given to publications of this kind.

Contract Reports are produced to report scientific work carried out under contract. Publications of this kind contain confidential matter and are reserved for the sponsors and the DCE. Therefore, Contract Reports are generally not available for public circulation.

Lecture Notes contain material produced by the lecturers at the DCE for educational purposes. This may be scientific notes, lecture books, example problems or manuals for laboratory work, or computer programs developed at the DCE.

Theses are monograms or collections of papers published to report the scientific work carried out at the DCE to obtain a degree as either PhD or Doctor of Technology. The thesis is publicly available after the defence of the degree.

Latest News is published to enable rapid communication of information about scientific work carried out at the DCE. This includes the status of research projects, developments in the laboratories, information about collaborative work and recent research results.

Aalborg University
Department of Civil Engineering
-
Risø DTU - National Laboratory for Sustainable Energy
Wind Energy Division

DCE Thesis No. 22

Wind Turbine Wake in Atmospheric Turbulence

PhD Thesis

by

Pierre-Elouan Réthoré

October 2009

Abstract

This thesis describes the different steps needed to design a steady-state computational fluid dynamics (CFD) wind farm wake model. The ultimate goal of the project was to design a tool that could analyze and extrapolate systematically wind farm measurements to generate wind maps in order to calibrate faster and simpler engineering wind farm wake models. The most attractive solution was the actuator disc method with the steady state k-ε turbulence model.

The first step to design such a tool is the treatment of the forces. This thesis presents a computationally inexpensive method to apply discrete body forces into the finite-volume flow solver with collocated variable treatment (EllipSys), which avoids the pressure-velocity decoupling issue.

The second step is to distribute the body forces in the computational domain accordingly to rotor loading. This thesis presents a generic flexible method that associates any kind of shapes with the computational domain discretization. The special case of the actuator disc performs remarkably well in comparison with Conway's heavily loaded actuator disc analytical solution and a CFD full rotor computation, even with a coarse discretization.

The third step is to model the atmospheric turbulence. The standard k-ε model is found to be unable to model at the same time the atmospheric turbulence and the actuator disc wake and performs badly in comparison with single wind turbine wake measurements. A comparison with a Large Eddy Simulation (LES) shows that the problem mainly comes from the assumptions of the eddy-viscosity concept, which are deeply invalidated in the wind turbine wake region. Different models that intent to correct the k-ε model's issues are investigated, of which none of them is found to be adequate. The mixing of the wake in the atmosphere is a deeply non-local phenomenon that is not handled correctly by an eddy-viscosity model such as k-ε .

Acknowledgments

Contents

Publications During the PhD Period

Pressure Jump Correction

1 **Réthoré, P.-E.**, Sørensen, N.N., *Modification of a Rhie-Chow/SIMPLE Pressure Correction Algorithm to Handle a Pressure Jump.* 3rd EAWE Seminar, CENER, Pamplona, Spain, October 2007. [Link]

2 **Réthoré, P.-E.**, Sørensen, N.N., *Actuator Disc Model Using a Modified Rhie-Chow/SIMPLE Pressure Correction Algorithm: Comparison to Analytical Solutions.* EWEC Brussels, April 2008. [Link]

Actuator Shape Model

3 Gilling, Lasse, Sørensen, N.N., **Réthoré, P.-E.**, *Cost Reduction of Large Eddy Simulation of Airfoils in Turbulent Inflow.* EWEC Marseille, March 2009. [Link]

Atmospheric and Wind Turbine Wake Turbulence

4 **Réthoré, P.-E.**, Sørensen, N.N., Bechmann, A., Zahle, F., *Study of the Atmospheric Wake Turbulence of a CFD Actuator Disc Model.* EWEC Marseille, March 2009. [Link]

Wind Farm Measurements

5 Barthelmie, R.J., Frandsen, S.T., Nielsen, N.M., Pryor, S.C., **Réthoré, P.-E.**, Jøregensen, H.E., *Modelling and Measurements of Power Losses and Turbulence Intensity in Wind Turbine Wakes at Middelgrunden Offshore Wind Farm.* Wind Energy 10 (6) pp.517-528, 2007. [Link]

6 **Réthoré, P.-E.**, Johansen, N.A., Frandsen, S.T., Barthelmie, R.J., Hansen, K., Jensen, L.E., Bækgaard, M.A.B. and Kristoersen, J.R.,

Systematic Wind Farm Measurement Data Reinforcement Tool for Wake Model Calibration. EOW Conference, Stockholm, September 2009. [Link]

Wind Farm Shadow Effect

7 **Réthoré, P.-E.**, Bechmann, A., Sørensen, N.N., Frandsen, S.T., Mann, J., Jørgensen, H.E., Rathmann, O. and Larsen S.E. 2007: *A CFD Model of the Wake of an Offshore Wind Farm: Using a Prescribed Wake Inflow.* The Science of making Torque from Wind, Second Conference, DTU, August 2007. [Link]

8 Frandsen, S.T., Jørgensen, H.E., Barthelmie, R.J., Rathmann, O., Badger, J., Hansen, K.S, Ott, S., **Réthoré, P.-E.**, Larsen, S.E., Jensen, L.E., *The Making of a Second-generation Wind Farm Efficiency Model Complex.* EWEC Brussels, April 2008. [Link]

9 Frandsen, S.T., Jørgensen, H.E., Barthelmie, R.J., Rathmann, O., Badger, J., Hansen, K.S, Ott, S., **Réthoré, P.-E.**, Larsen, S.E., Jensen, L.E., *The Making of a Second-generation Wind Farm Efficiency Model Complex.* Wind Energy 12(5) pp.445-458, 2009. [Link]

10 Frandsen, S., Barthelmie, R., Rathmann, O., Jørgensen, H. E., Badger, J., Hansen, K., Ott, S., **Réthoré, P.-E.**, Larsen, S. E., Jensen L. E., *Summary report: The Shadow Effect of Large Wind Farms: Measurements, Data Analysis and Modelling.* Technical Report, Risø-R-1615(EN), Risø-DTU, 2009. [Link]

Nomenclature

Abbreviations

Abbreviation	Definition
AD	Actuator Disc
AL	Actuator Line
AS	Actuator Shape
BE	Blade Element
BEM	Blade Element Momentum
BC	Boundary Condition
CDS	Central Difference Schemes
CFD	Computational Fluid Dynamics
DNS	Direct Numerical Simulation
DTU	The Technical University of Denmark
ECN	Energy research Centre of the Netherlands
EVM	Eddy-Viscosity Model (based on RANS)
HAWT	Horizontal Axis Wind Turbine
IEA	International Energy Agency
LES	Large Eddy Simulation
MM, Met. Mast	Meteorological mast
QUICK	Quadratic Upstream Interpolation for Convection Kinematics [52]
RANS	Reynolds-averaged Navier-Stokes
RSM	Reynolds-Stresses Model
SIMPLE	Semi-Implicit Method for Pressure-Linked Equations [65]
TKE	Turbulent Kinetic Energy

Greek Letters

Symbol	Definition
$\alpha_{\eta z}$	Differential areas of the cell faces projected in the Carthesian coordinates
β	Jacobi amplitude
β_p	Production parameter of the Canopy model
β_d	Dissipation parameter of the Canopy model
δ_{ij}	Dirichlet function
Δ	Maximum cell size in all directions
Δx	Cell size in the x-direction
ΔI	Wake interface size
ε	Turbulent kinetic energy dissipation
κ	von Kármán constant
$\Lambda_0(\beta, k)$	Heuman's lambda function
μ	Viscosity
μ_t	Eddy-viscosity
ν	Kinetic viscosity, μ/ρ
ν_t	Kinetic Eddy-viscosity, μ_t/ρ
Ω	Dummy quantity
ω	Vorticity distribution
ω	Specific dissipation rate
Ψ	Stream function
Π_ε	Pressure-strain of rate term in the ε-equation
Π_k	Pressure-strain of rate term in the k-equation
ρ	Density
σ_m	Standard deviation of 10-minute wind speed data
$\Theta^X_{(\lambda,\mu,\nu)}$	Coefficient associated to a function X, $(\lambda, \mu, \nu) \in \mathbb{N}$

Roman Letters

Symbol	Definition
a	Induction factor
A	Area
A^y_x	Coefficient of the cell x relative to the cell y
c	Number of cells on a rotor disc in the y-direction
C_x	Cell face mass fluxes position x
C_T	Thrust coefficient
C_F	Force coefficient (include the thrust coefficient and the torque coefficient)

Symbol	Definition
C_{Swz}	Parameter in the Realizability model
$C_{\varepsilon p}$	Production parameter in the ε-equation of the Canopy model
$C_{\varepsilon d}$	Dissipation parameter in the ε-equation of the Canopy model
C_{Δ}	LES parameter
c/D	Number of cells per rotor diameter
$E(\beta, k)$	Incomplete elliptic integral of the second kind
$\mathbf{E}(k)$	Complete elliptic integral of the second kind
E	East cell center
e	Cell interface between P and E
EE	Second east cell
f_i	Dummy function in i-direction
F_x	Discrete force at position x
$F(\beta, k)$	Incomplete elliptic integral of the first kind
F_{ε}	Source term in the ε-equation accounting for the wind turbine forces
F_k	Source term in the k-equation accounting for the wind turbine forces
$\mathcal{F}$	Function to reduce the eddy-viscosity
g	Dummy function
g	Gravity acceleration
$\mathcal{G}$	Function to smooth locally the effect of the canopy model
$I_{(\lambda, \mu, \nu)}$	Bessel-Laplace integral, $(\lambda, \mu, \nu) \in \mathbb{N}$
$J_{\nu}(z)$	Bessel function of the first kind
$\mathbf{K}(k)$	Complete elliptic integral of the first kind
k	Elliptic modulus
k'	Elliptic complementary modulus ($k' = \sqrt{1 - k^2}$)
k	Turbulent Kinetic Energy (TKE)
k-ε	EVM Turbulence model [50]
k-ω	EVM Turbulence model [98]
$\mathrm{Kn}_{i,j}$	Knudsen number of i-component in j-direction
ℓ	Turbulence length-scale
m	Elliptic parameter ($m = k^2$)
m'	Elliptic complementary parameter ($m' = 1 - m$)
$\mathbf{n}$, n_i	Normal vector
$n_{x,y}$	Normal vector at position x in the y-direction
P	Currently observed cell center
P	Pressure
P_x	Pressure at position x
P_x^j	Pressure jump at position x

Symbol	Definition
P_τ	Production of turbulence
$R_w(z)$	Wake radius at an axial distance z from the wind turbine
R_∞	Ultimate wake radius of the wind turbine
S_{U-mom}	Explicit terms of the momentum equation
S_x	Face surface area at position x
U	Flow velocity in x-direction
U_∞	Inflow velocity
V_x	Cell volume at position x
W	West cell center
w	Cell interface between P and W
WW	Second west cell
D	Rotor Diameter
H	Wind turbine hub height
U_∞	Inflow velocity
$U_{\infty,H}$	Inflow velocity at hub height
$u*$	Friction velocity
R_{ij}	Reynolds Stress
$\boldsymbol{x_p}$	Position vector
$\boldsymbol{x}$	Position vector
x_D	Position of the actuator disc
t_p	Time at position p
t	Time
U	Velocity $U = \overline{U} + u$
u	Velocity fluctuation
$\overline{U}$	Velocity average
$L_{p,j}$	Distance scale in j-direction $L_{p,j} = x_j - x_{p,j}$
z	Height
z_0	Surface roughness height
z_H	Wind turbine hub height

Note that in the current report the notation β, k and k' are used for the parameters of the elliptic functions to be consistent with the notation of Conway [27] and Wrench [99]. It is nonetheless interesting to notice that in most of the cases observed, the elliptic functions are coded using as input the elliptic parameter $m = k^2$ and $m' = 1 - m$, instead of k and k'.

1

Introduction

Contents

1.1 Wind Farm Wake

The purpose of wind turbines and by extension wind farms is to extract energy from the wind and convert it into a usable energy (e.g. electrical, mechanical). From the basic concept of conservation of energy, it is clear that if kinetic energy is extracted from the wind, the kinetic energy left downstream of a wind turbine is decreased compared to the kinetic energy upstream of the wind turbine. It is consequently necessary to model the wind turbine wake in order to estimate how much energy is left for the downstream wind turbines and how much power the wind turbines can produce.

A typical modern wind farm has in general wake losses around 10–20% [7]. As a consequence, one part of the problem of wind farm wake is to estimate how much power a wind farm can produce for a given wind inflow.

In the process of extracting kinetic energy, the wind turbines modify the structure of the wind flow by creating small turbulence structures and by reducing largely the wind velocity. The structure of the wind flow modified by the turbine is transported downstream of the wind turbine. Furthermore, the difference of velocity between the wake region and the free-stream region

generates some turbulent vortex structures at the boundaries of the wake. As the wake interface expands, the induced turbulent vortex structures grow in size and contribute to the wake recovery. The interaction between these different types of structures and the atmospheric turbulence creates a spatial oscillation of the wake called wake meandering, which can be regarded as a large-scale component of the wake turbulence.

The downstream wind turbines, as a consequence, observe a wind inflow modified both in terms of mean velocity and turbulence. These wind fluctuations increase the structural vibrations of the wind turbine, which cause increased fatigue loads. The fatigue loads reduce the wind turbine lifespan and can potentially increase the maintenance cost. Another part of the problem of wind farm wake is then to estimate the fatigue loads caused by the combined wakes.

The wind farm wake effect is an important issue during the whole lifespan of a wind farm. During the planning phase, the wind farm developers want to have a good estimate of how to place the wind turbines to obtain the most power and the least fatigue loads. In this process, the wind farm wake models can be used to optimize the wind farm layout based on the different economical factors (e.g. power production, wind farm lifetime, cables cost, type of soils and water depth). Better wind farm wake models may, therefore, increase the cost benefits of the wind farm.

In the funding phase, the bank requires, among other things, an accurate estimate of the wind farm Annual Energy Production (AEP) and of the maintenance cost. These two numbers are significantly linked to the quality of the wind farm wake analysis. A reduction of the uncertainty on the wake models is linked to a reduction of the investments risks, which might eventually make wind energy a more competitive solution.

In the operational phase, the wind farm operator has to be able to forecast the production of the wind farm in order to bid precisely on the electricity market. Any variation from the initial forecast costs money to the wind farm operator. A good wake model may significantly increase the power production forecast of the wind farm and may reduce its operational cost.

Moreover, it has been argued by Corten and Shaak [29] that a smarter wind farm operational strategy, based on wake models, could reduce the equivalent fatigue loads on the turbines and significantly increase its power output. Finally, as it can become costly to make mistakes in the power production forecasting, more and more wind farm operators implement wind farm regulation control to reduce the power output of the wind farm in order to match the requests of the grid operator. This process also needs to deal with wake, as reducing the power output of a wind turbine means reducing its energy extraction. This might influence the downstream wind turbines production.

Most of the wake models used by the industry nowadays were developed

in the 1980s and early 1990s. Since that time the wind turbines rotor diameter have roughly been multiplied by a factor 2–3 and the wind farms width by 4–6 and is believed, by some, to keep increasing. The wind turbines and wind farms have become so big that they are now believed to have a significant effect on the local meteorology [21]. The net effect of these increases is that the models, which were designed and calibrated for small wind turbines and wind farms perform poorly. The assumptions made in those models are too drastic and become more and more irrelevant with the sizes and the distances increasing.

Moreover, the wind farms are now being built offshore, where the wind conditions have much more dependence stability effects than onshore. As the water roughness is very small, the turbulence is also preserved over larger distances offshore than onshore.

The wind turbine and wind farm increase of size also has another effect, the amount of investments in relation to the wake losses have dramatically increased.

Finally, wind farms are now installed at closer distances to each others, to a point where problems arise on estimating the impact that one wind farm has on another. The combined wake of a wind farm is here referred as the wind farm shadow. There are, for example, many wind farm projects in the German North Sea that are expected to interact in a very complex manner. The current wake models are not designed for that task and are expected to perform poorly. Moreover, there is no current data available for their calibration.

1.2 Wind Farm Wake Models

A comprehensive literature survey on wind turbine and wind farm wake models can be found in Crespo et al. [30] and Vermeer et al. [97]. Moreover, the latest developments in wind farm wake models to this date are described concisely in Troldborg's PhD thesis [96] and in the literature review of Sanderse [76]. Nonetheless, for the sake of clarity, the main trends in wind farm wake modelling are briefly introduced in the following sections.

Modelling wind turbine wake is a particularly challenging task because it is directly associated to atmospheric turbulence modelling and to airfoil flow modelling, which are two of the unresolved problems of the physics of fluid dynamics. A particularly delicate issue that arises from this combination is that several orders of magnitude of turbulence length-scales play an important role and interact in a complex manner upstream and downstream of the wind turbine. There is, for instance, the atmospheric turbulence scale, characterizing the motion of large atmospheric eddies, which increases linearly

with height in the surface layer and can be up to several hundred meters (Peña et al. [66]). Then, there is the wake interface turbulence scale, characterizing the mixing of the wake boundaries with the atmospheric flow, which eventually evolves to be roughly of the same order of magnitude than the wind turbine rotor diameter. And finally, there is the turbulence length-scale of the blade induced vortex structures, which are related to the dimension of the blade chord.

Because of these different scales, which are more or less important at different locations in the wake, a natural simplification is to speak about close wake and far wake regions. The close wake region is in the direct vicinity of the wind turbine, where the role of the blades induced turbulence structures are dominant. The far wake region is located at a larger distance downstream, where the shear induced turbulence becomes dominant and is progressively absorbed by the atmospheric turbulence. While models have existed for these three types of scales for about a century, little is known about the interaction between them.

Most of the wake models are based on the principle of conservation of mass and momentum. The turbines are often modelled as a sink of momentum corresponding to the thrust force of the turbine. The simplest models neglect terms in the Navier-Stokes Equations and assume the wake to be homogeneous and axisymmetric for increasing the solving speed.

Some of the fastest methods are designed to model the wake expansion directly instead of the turbulence (Lissaman [53], Jensen [46], Frandsen [36] Rathmann [69]). They basically enforce the momentum conservation on a wake region, which is increased according to a semi-empirical wake expansion function.

Other wake models resolve the turbulence using simplified turbulence closure techniques such as eddy-viscosity mixing-length models (Ainslie [4], Lange et al. [48]). As it is presented in Chapter 5, eddy-viscosity models have difficulties to model large-scale turbulence in presence of smaller scale velocity changes. For this reason turbulence is sometimes split in two parts, the large-scale part, modelled as passive tracers to represent the meandering effect and the small-scale part, modelled with an eddy-viscosity model (Larsen et al. [49]).

More wake advanced models retain all the elements of the Navier-Stokes Equations and model the wake and atmospheric turbulence in different ways (e.g. Computational Fluid Dynamics (CFD) with Large Eddy Simulation (LES), Reynolds-averaged Navier-Stokes (RANS) and Reynolds-stresses Model (RSM)) with different flow solvers and different force estimation algorithm. They are mostly research models (Ammara et al. [5], Mikkelsen [63],

Crespo et al. [31], Cabezon et al. [18]), yet some faster CFD models are also commercialized (Schepers [79], Castro et al. [19]).

The computational cost increases with the complexity of the model and with the amount of physics it contains. The simplest models can resolve many cases in a few seconds on a personal computer, while the most complex models can only resolve a single case during several weeks using supercomputers.

1.3 How to Improve the Models?

The simpler models used by the industry lack some physics in comparison to the more advanced CFD models. However, completely abandoning them in favour of more computationally expensive models might not be the best short-term solution. There are many cases where faster models can achieve tasks that would simply be too time consuming with slower models (e.g. layout optimization, power forecasting). Nevertheless, there is still much to learn from the physics of the CFD models in order to improve the faster engineering models.

Another way of improving the models is to use the information provided by the wind farm measurements. The offshore wind farms are in particular interesting in the sense that they do not present any terrain effects and they have various turbulence stability cases to study. The usable information available is nonetheless, in a way, rather limited. The wind farm measurements are typically composed of some meteorological (met.) mast measurements (e.g. wind speed, wind direction, pressure, temperature, humidity) and of wind turbine measurements (e.g. nacelle wind speed, nacelle yaw, power production, rotation speed, pitch angle, blade and tower bending moments). While this certainly represents a very large quantity of information, it does not give information about what happen to the wind between the wind turbines, neither what happens above the wind farm. Moreover, as measurements and wind turbines have a non negligible probability to fail, the cases where all the wind turbines and measurements devices work simultaneously are very scarce (e.g. in a wind farm with 100 turbines where each have an availability of 97%, the probability that all operate normally at the same time is $0.97^{100} < 5\%$).

In these conditions, extracting valuable information from wind farm measurements becomes so complex that it is a science in itself. Until a point where it is actually needed to model the measurements in order to understand them. There is, therefore, a need for more information than that the measurements can provide and the most affordable solution is to try to extend the measurements and to extrapolate them using the most advanced

models available. However, as the amount of data to process is rather large, there is a need for a wake model, which is fast enough to process the measurements in an acceptable time scale and at the same time retains most of the physics necessary.

All this indicates that a CFD study of wake can provide a useful tool to improve and calibrate faster engineering models. It might also help to bridge the gap between the models and the measurements.

The Risø National Laboratory for Sustainable Energy - Technical University of Denmark (Risø-DTU) has done extensive studies on wind turbine and wind farm wake in the last decades and has developed many different types of wind farm models [46, 39, 69, 49]. In this context, one of Risø-DTU's objectives is to provide the wind industry with tools to estimate wind farms energy production such as WAsP [2]. In order to improve the existing wake models and to develop more advanced ones, some measurements campaigns have been carried out on wind farms in collaboration with wind farm operators [59]. Interpreting those measurements is nonetheless a difficult task. In this context, the goal of the current project is to develop a tool capable of carrying full-scale wind farm wake computations and to enhance the available measurements for providing detailed wind map to help the design of better and faster engineering wake models.

1.4 CFD Wind Turbine Wake Models

There are three main CFD wind turbine wake models. The most expensive and detailed are the full-rotor computations, in which the whole geometry of the rotor is detailed (Sørensen and Johansen [90], Zahle [100]). While they provide very detailed information on the flow passing through the rotor, it becomes extremely expensive to model the far wake region while retaining the same level of details. Consequently, this method still requires too much computational power for multiple wakes.

An intermediate method is to model each wind turbine blade as a line or surface of force acting on the wind. The method is called actuator line method (Sørensen and Shen [88], Mikkelsen [63]) and the actuator surface method (Shen et al. [83], Dobrev et al. [33], Sibuet Watters and Masson [85]). While it is still computationally expensive, multiple wake models have been successfully studied by Trolborg [96] using the actuator line method. These methods provide a cost effective way to study the dynamics of the vortex structures evolving in the wake region. The forces can be estimated using the airfoil definition and geometry of the blades and the local velocities at the rotor disc.

Finally the simplest CFD method to model the wind turbine wake is the actuator disc (AD) method. The idea is to model the influence of the wind turbine rotor on the flow as a disc of forces. The blade forces are therefore assumed to be smeared over the area of the disc. The forces can be determined in the same way as the actuator line or surface method or in simpler fashions, e.g. using the thrust coefficient (C_T) curve. As this method does not require the same level of details as the actuator line method, it is relatively faster. The downside is that the vortex structures are not as detailed as in the actuator line. One of the most attractive aspects of the actuator disc is the fact that it can give a steady state solution with the atmospheric boundary layer modelled, while the other method cannot because of the rotating elements. A large number of different models have been developed based on this concept [5, 63, 31, 18, 68, 19, 79]. They mostly differ on the choice of the CFD flow solver, how the forces are computed (e.g. using a thrust coefficient curve, Blade Element method, Vortex method) and how the atmospheric turbulence is modelled.

1.5 Turbulence Models

There are different types of turbulence models used in CFD for modelling wind turbine wake. The most advanced is the LES method. It basically splits the turbulence into two parts, a resolved part modelling the large-scale turbulence, which is carried out through an unsteady simulation and an unresolved part modelling the small-scale turbulence, which is modelled using more basic turbulence models such as an eddy-viscosity model (EVM). LES models are particularly adapted to wake modelling as the wake can be seen to have two distinct ways to dissipate. One part interacts mainly with the large eddies of the atmosphere, which create the wake meandering phenomenon. While the other part, the small-scale of turbulence, is mainly self-generated through the local velocity shear.
As a large part of the LES turbulence is resolved, it needs to be generated in some fashion. There are two main methods, which can be found in the literature. One way is to use an analytical model to generate coherent turbulence (Trolborg [96], Ivanell [45] and Gilling et al. [40] used the turbulence model of Mann [57]). The problem is that the large scale turbulence introduced is naturally dissipated because it is not in balance with the wind speed shear introduced, as a consequence it is difficult to model atmospheric turbulence over large distance, such as a wind farm. Another way is to generate turbulence using a precursor mesh (Bechmann [11]). A precursor box with a wall boundary condition (BC) at the bottom, with the terrain roughness, is used to run a LES using periodic condition. After a relatively large number of iterations, the rough wall creates eddy structures that are numerically pre-

served and are similar to atmospheric eddies. This method is very expensive and building up the precursor box can take several weeks on a cluster.

The other types of turbulence models are mostly based on the RANS Equations. They can nonetheless be steady state or unsteady. There are many turbulence models based on RANS, the most used are based on the eddy-viscosity concept, where the Reynolds-stresses are assumed to be directly proportional to the local velocity shear and where only the eddy-viscosity is modelled (k-ε [50] and k-ω [98]).
More advanced models are based on modelling the Reynolds-stresses independently. Gomez-Elvira et al. [41] and Cabezon et al. [18] used a non linear constitutive relation, based on an expansion of the Boussinesq approximation (Lumley [54], Taulbee [92]). While they are more physical than the eddy-viscosity models, they are more complicated to use and to validate, as they have many more closure parameters. They are also significantly slower. One common issue with the RANS models is that all the scales of turbulence are mixed together. It is then difficult to model the complex interaction between the three types of turbulence introduced in Section 1.2.

Risø-DTU and DTU-MEK have developed in the last 15 years several wind turbine wake models based on the flow solver EllipSys [89] [62]. Recently, a considerable effort has been put on modelling the flow going through multiple wind turbines using LES with the actuator line method (Troldborg [96]) and the actuator disc method (Ivanell [45]). While the studies were successful and brought in light many interesting details of the multiple wake interaction, they remain too computationally expensive for extrapolating wind farm measurements or for carrying out the interaction of a wind farm over another. In order to do that a simpler and faster turbulence model is needed. For this reason, this study focuses on using the fastest turbulence model used with EllipSys, the k-ε model, together with the fastest wind turbine wake model, the actuator disc model.

1.6 Work Summary and Thesis Structure

During one year before and during the first year of the PhD, the work was mainly focused on data analysis of offshore wind farms. The outcome of this work was the development of an analysis tool that is able to extract information from different databases, correct the eventual sensor errors, filter the data to obtain relevant atmospheric and wind turbine conditions, presenting the status of the wind farm and met.mast in a Graphical User Interface (GUI). This tool has been used to produce measurement results for several publications [6, 9, 8, 7, 59, 39, 37, 38]. Finally, the accumulated experience on correcting the data using a set of preprocessing methods was also the
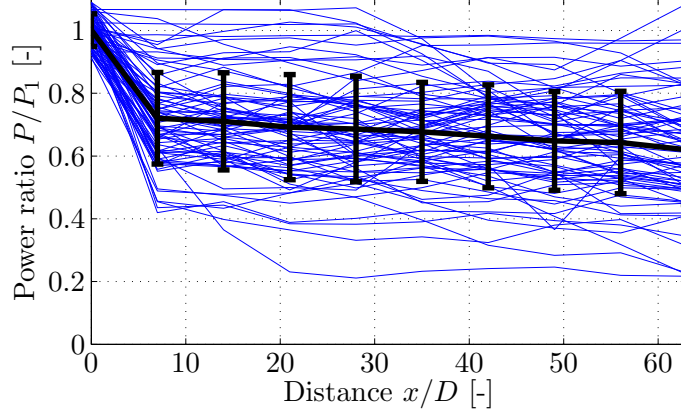
Figure 1.1: Power ratio along a line of 10 wind turbines. The blue lines represent all the 10-minute cases meeting the filtering criteria (Wind direction aligned with the row of turbines $\pm 5^o$, $P1 = \frac{1}{2}P_{\text{rated}} \pm 5\%$). The black line is the average value of all the cases, with the standard deviation presented as errorbars.

subject of an article (Réthoré et al. [71], which is presented in Appendix C. While the data available for analysis was consequent and represented in total several years of wind farms operational time, statistical representative information was difficult to obtain. A representative illustration of the measurements output is presented in Fig. 1.1. The large number of different types of inflow conditions (including stability effects) together with the combined uncertainty and failure rate of the different sensors and wind turbines reduce dramatically the number of cases available per inflow conditions. The difficulty to interpret the measurements has a significant influence on the quality of the wake model calibration. This observation motivated the development of a general method for carrying out full scale wind farm wake computation to be able to understand and expand the measurements information.

The second part of the PhD was oriented towards wind turbine wake modelling and was based on the flow solver EllipSys3D, which is described in details in Michelsen [62], Sørensen [89] and Bechmann [11]. For the reader convenience, EllipSys and the different models it is based on are briefly introduced in Appendix A.1.

During the first year of the project, two Danish offshore wind farms (Horns Rev II and Nysted II) were in the final planning phases at a close distance to existing wind farms. As a consequence, there was a sudden growth of interest regarding wind farms shadow effect from the different groups involved in the wind farm planning. Risø-DTU presented different

models to address this issue (Frandsen et al. [38]). As it was the early stage of this PhD, the methods described in this thesis were not yet available for analysis. Nonetheless, it was decided to complement the lack of a wind turbine wake model by the available measurements of the offshore wind farms to study if it was possible to observe a trend of the wind farm wake recovery over a large distance downwind the turbine. The outcome of this work was the subject of a journal paper (Réthoré et al. [70]) and is presented in Appendix D .

Different actuator disc and actuator line models have been developed for EllipSys. They are all based on a three steps method: 1) the rotor disc velocities are interpolated, 2) the forces are estimated and 3) the corresponding body forces are applied at the blades or rotor disc location. The third step represented an issue, because it turned out that by applying a discrete body force into a finite-volume CFD method based on collocated-variables discretization, such as EllipSys, a pressure-velocity decoupling is generated around the location of the forces. The decoupling is characterized in the simulation by intense numerical fluctuations from one cell to another and is a phenomenon previously discussed by Mikkelsen [63] and Leclerc and Masson [51]. This is particularly inconvenient because a precise estimation of the local velocities at the disc is necessary in order to determine the corresponding wind turbine forces. A mitigation to this issue is to replace the discrete body force by redistributing it over a larger amount of cells using for example a Gaussian distribution (Mikkelsen [63], Troldborg [96], Ivanell [45]). While this method effectively reduces the numerical fluctuations, it needs a relatively large amount of cells to redistribute the forces, which increases the computational cost.
The interest is here to develop a tool relatively fast so that it can carry out computations over very large wind farms. In order to reduce the amount of cells necessary for modelling each wind turbine, a method (Réthoré and Sørensen [73, 74]) is detailed in Chapter 2. This method modifies the pressure correction algorithm to take into account the discretization effects. This method makes it possible to apply discrete body forces over only 3 cells.

The following step, when developing an actuator disc model, is to define a way to redistribute the forces inside the computational domain. As this is a common issue when dealing with body forces in CFD, it was decided to develop a generic flexible method that can be adapted to all kind of actuator methods and more generally to all kind of body forces applications. The method presented in Chapter 3 is based on finding the intersectional polygons between two types of discretization. In the case of the actuator disc, the discretization of the disc is a polar grid. The intersectional polygons of each polar element of the disc with the computational domain cells redistribute proportionally the disc forces in the computational domain. The

method is successfully compared to Conway's analytical solution for heavily loaded actuator discs [24, 25] and a CFD full-rotor computation.

In addition, this method was used to design an immerse boundary technique for generating an unsteady turbulent inflow (Gilling et al. [40]).

When the actuator disc is modelled together with atmospheric turbulence using the standard k-ε model, the solution greatly underpredicts the wake effect when compared to measurements (El Kasmi and Masson [35], Cabezon et al. [18], Réthoré et al. [72], Rados et al. [68]). A parametric study, carried out in Chapter 4, links this error with the size of the eddy-viscosity. LES models have in general eddy-viscosities several orders of magnitude smaller than the atmospheric k-ε model. Based on the threshold value found, under which the eddy-viscosity does not yield an underprediction of the wake effect, it is postulated that LES models can avoid the problem observed in the k-ε simulations.

Chapter 5 is then dedicated to explain the origin of this problem by comparing the results of a LES to the standard k-ε model. The eddy-viscosity concept is found to be the main contribution to the k-ε errors.

Then, in Chapter 6, based on the observations performed in Chapter 5, several scenarios are proposed to modify the k-ε model to address this issue. The methods are compared to the LES model and to different single wind turbine wake measurements. However, the outcome of this comparison it that the existing corrections to the k-ε model are not adequate for modelling single wind turbine wake in atmospheric turbulent flows and by extension full wind farms. There is therefore still a critical need for a steady-state turbulence model that is able to handle different scales of turbulence at the same time.

2

Forces Treatment

Contents

2.1 Introduction

CFD generally refers to methods that solve the Navier-Stokes Equations by spatial and temporal discretization. The Navier-Stokes Equations are essentially composed of velocity terms, pressure gradient terms and body forces. When spatially discretized over a mesh, using a finite volume method, if the pressure and velocity terms are estimated at the same location, a pressure-velocity decoupling might occur that can lead to numerical oscillations of the pressure (or pressure wiggles). One way of dealing with this issue is to keep the velocities at the cell faces and the pressure terms at the cell centers, so that the derived pressure gradient terms, are located at the same place as the velocity terms. This is called the staggered grid method. The other

standard way is to keep the pressure and velocity terms at the cell centers (known as the collocated variable method) and to use a special treatment of the pressure, to avoid the pressure-velocity decoupling. This method, which was first introduced by Rhie-Chow [75], was never intended for the treatment of the pressure-velocity decoupling introduced by imposing a sudden jump of pressure, or discrete body forces.

EllipSys, the in-house curvilinear CFD code designed at Risø-DTU [89] and MEK-DTU [62] is based on a collocated variable arrangement that uses the Rhie-Chow pressure correction algorithm. Discrete body forces are used in the present context to model the influence of wind turbines on the flow. In order to overcome the pressure wiggles introduced by discrete body forces, one approach is to smooth out the body forces by using a Gaussian distribution instead of a Dirac delta distribution (Mikkelsen [63]). This method requires a pressure jump made over several cells, which can become computationally expensive on large problems like, simulating a wind farm. In order to save computational cost, a modification of the Rhie-Chow algorithm is proposed to treat the special case of discrete pressure jumps. This method is in practice close to what is proposed by Masson et al. [58] and Mencinger et al. [60].

In the following sections, the problem of the pressure wiggles is presented for a 1D example of a regular Cartesian mesh with a special case of uniform velocity over the domain. The proposed algorithm is then described in the context of the curvilinear CFD code EllipSys3D. For the sake of clarity, the same notation found in the original description of EllipSys are here used (Sørensen [89]).

2.2 Pressure Jump Correction

Implementing discrete body forces into a non-staggered CFD code can generate undesirable numerical wiggles. One way to cope with this situation is to avoid having discrete body forces by smearing the force over its neighbouring cells. This method can become computationally expensive, as there is a need for having a large number of cells to model a discrete jump of pressure.

This chapter presents an alternative way to avoid these numerical wiggles by transforming the discrete forces located in the cell center, used in the Navier-Stokes Equation, into pressure jump terms located at the cell faces, used in the pressure correction algorithm. After describing the origin of these numerical fluctuations using a simple 1D case, with uniform velocity, the principle of the Rhie-Chow algorithm is briefly introduced. The basic ideas behind the pressure jump correction and its application to the CFD code EllipSys are then presented.
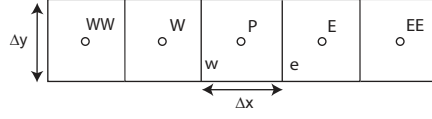
Figure 2.1: 1D mesh.

2.2.1 Origin of Pressure Wiggles in the Non-Staggered Approach

The Navier-Stokes Equations are composed of the Momentum Equations and the Continuity Equation. The 1D Momentum Equation in x-direction can be written as

$$\frac{\partial \rho U}{\partial t} + \frac{\partial \rho U U}{\partial x} = -\frac{\partial P}{\partial x} + \frac{\partial}{\partial x}\left(\mu \frac{\partial U}{\partial x}\right) + F, \qquad (2.1)$$

where U is the flow velocity, P is the pressure, μ is the viscosity, ρ is the density, t is the time, x is the distance and F is a volume force [N/m^3].

In order to have an equation for the pressure, the Continuity Equation is used

$$\frac{\partial \rho U}{\partial x} = 0. \qquad (2.2)$$

In the finite volume formulation, derivatives can be discretized by integrating them over a control volume. Using a Central Difference Scheme (CDS) over the 1D mesh presented in Fig. 2.1, the following rules can be applied.

$$\int_P \frac{\partial \Omega}{\partial x} \, \mathrm{d}x \, \mathrm{d}y = (\Omega_e - \Omega_w)\,\Delta y = (\Omega_E - \Omega_W)\frac{\Delta y}{2}, \qquad (2.3)$$

$$\begin{aligned} \int_P \frac{\partial \Omega \Omega^*}{\partial x} \, \mathrm{d}x \, \mathrm{d}y &= (\Omega_e \Omega_e^* - \Omega_w \Omega_w^*)\,\Delta y \\ &= [\Omega_E(\Omega_E^* + \Omega_P^*) - \Omega_W(\Omega_W^* + \Omega_P^*) \\ &\quad + \Omega_P(\Omega_E^* - \Omega_W^*)]\,\frac{\Delta y}{4}, \qquad (2.4) \end{aligned}$$

$$\begin{aligned} \int_P \frac{\partial}{\partial x}\left(\frac{\partial \Omega}{\partial x}\right) \, \mathrm{d}x \, \mathrm{d}y &= \left[\left(\frac{\partial \Omega}{\partial x}\right)_e - \left(\frac{\partial \Omega}{\partial x}\right)_w\right]\Delta y \\ &= (\Omega_W + \Omega_E - \Omega_P)\frac{\Delta y}{\Delta x}. \qquad (2.5) \end{aligned}$$

where Ω is a dummy variable, x and y are distances, W, P, E indicate the position of the cells, w, e, the position of the faces (see Fig. 2.1) and the *

indicates that the term is known from a previous time step.

Applying these rules on the Continuity Equation Eq. (2.2) gives

$$\Delta y \left(\rho U_e - \rho U_w \right) = 0, \tag{2.6}$$

which, therefore, leads to a second relationship,

$$U_W = U_E. \tag{2.7}$$

Assuming a steady flow and, therefore, dropping the unsteady term in Eq. (2.1) gives

$$\rho \left[(UU^*)_e - (UU^*)_w \right] \frac{\Delta y}{4} = (P_W - P_E) \frac{\Delta y}{2} + \mu \left(U_W + U_E - 2U_P \right) \frac{\Delta y}{\Delta x} + F_P \Delta x \Delta y. \tag{2.8}$$

Eq. (2.8) can be rewritten into a general formulation by linearization and the assumption that one of the Us is known in the convective term (UU term)

$$A_P U_P = \sum_P A_P^{nb} U_{nb} + (P_W - P_E) \frac{\Delta y}{2} + F_P \Delta x \Delta y, \tag{2.9}$$

with $nb \in (W, E)$ and

$$\begin{aligned}
A_P^W &= \mu \frac{\Delta y}{\Delta x} + \rho \frac{\Delta y}{4} (U_W^* + U_P^*), \\
A_P^E &= \mu \frac{\Delta y}{\Delta x} - \rho \frac{\Delta y}{4} (U_E^* + U_P^*), \\
A_P &= 2\mu \frac{\Delta y}{\Delta x} + \rho \frac{\Delta y}{4} (U_E^* - U_W^*).
\end{aligned} \tag{2.10}$$

Note that Continuity states that $\rho \Delta y U_W = \rho \Delta y U_E$, therefore $A_P = A_P^W + A_P^E$.

The cell center velocity obtained from the Momentum Equation Eq. (2.9) can be interpolated, using the midpoint rule, at the cell face in order to apply the Continuity

$$U_e = \frac{1}{2} \left(U_P + U_E \right). \tag{2.11}$$

A simple case can be applied, where the velocity is assumed to be uniform in the domain (i.e. $U_{WW} = U_W = U_P = U_E = U_{EE}$). Combined with the assumption of a regular Cartesian mesh, all the velocity terms and coefficients A_*^* are eventually cancelled with each other. Inserting Eq. (2.9) into Eq. (2.7) gives

$$\begin{aligned}
(P_{WW} - P_P) \frac{\Delta y}{2} + F_W \Delta x \Delta y &= (P_P - P_{EE}) \frac{\Delta y}{2} + F_E \Delta x \Delta y, \\
P_{WW} - 2P_P + P_{EE} &= (F_E - F_W) \Delta x.
\end{aligned} \tag{2.12}$$

If there are not body forces in the domain, the relationship between the pressure at each cell becomes

$$P_P = \frac{1}{2} \left(P_{WW} + P_{EE} \right).$$ (2.13)

As the pressure of a cell is not dependent of its direct neighbouring cells pressure, this relationship can be satisfied by a pressure wiggle solution (also called the check-board solution)

2.2.2 The Rhie-Chow Algorithm

The Rhie-Chow algorithm addresses this issue by separating the pressure terms from the rest of the momentum terms, when the face velocities are derived. Instead of interpolating the pressure gradient at the cell faces using the pressure gradients at the cells center, they are directly derived from the pressure at the closest cells center.

$$U_e = \frac{1}{2} \left(\widetilde{U_P} + \widetilde{U_E} \right) + \frac{\Delta y}{A_e} \left(P_P - P_E \right),$$ (2.14)

where

$$\widetilde{U_P} = \frac{1}{A_P} \left(\sum_P A_P^{nb} U_{nb} + F_P \Delta x \Delta y \right), \quad \text{and} \quad A_e = \frac{1}{2} \left(A_P + A_E \right).$$ (2.15)

where the $\sim$ sign indicates that it is the velocity terms without the pressure.

By inserting Eq. (2.14) into the Continuity Equation (2.2) a different relation is found

$$\frac{1}{2} \left(\widetilde{U_E} - \widetilde{U_W} \right) + \frac{\Delta y}{A_e} \left(P_P - P_E \right) - \frac{\Delta y}{A_w} \left(P_W - P_P \right) = 0.$$ (2.16)

Applying the same simple case of uniform velocity in the entire domain, with a regular Cartesian mesh, all the velocity terms cancel each other, which brings a relationship between the pressure and the body forces

$$\frac{1}{2} \left(F_E - F_W \right) \Delta x \Delta y + \Delta y \left(2P_P - P_W - P_E \right) = 0.$$ (2.17)

If there are no body forces in the domain, then the pressure in the cell P_P is related with its direct neighbouring cells pressure,

$$P_P = \frac{1}{2} \left(P_W + P_E \right).$$ (2.18)

In this case, the oscillation's pressure field is not a solution.
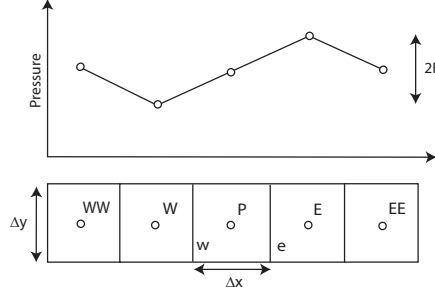
Figure 2.2: Pressure jump with wiggles.

2.2.3 Applying a Discrete Force

If there is a discrete force F_P applied in the cell P, the Momentum discretization Eq. (2.9) can create wiggles. If the velocity is the same over the domain, all the velocity terms are then cancelled with each other, which gives a relationship between the body force and the pressure:

$$P_E - P_W = 2F_P \Delta x. \tag{2.19}$$

Similarly, applying Eq. (2.9) on the cell W and E shows that there is a pressure wiggle solution

$$P_P - P_{WW} = 2F_W \Delta x = 0 \quad \text{and} \quad P_{EE} - P_P = 2F_E \Delta x = 0. \tag{2.20}$$

So even using the Rhie-Chow correction, applying a sudden pressure jump into this scheme causes the appearance of numerical pressure wiggles (see Fig. 2.2).

2.2.4 Proposed Modification

In order to correctly handle discrete forces in the Momentum Equations, the forces are defined at the face of the cells in the same way the pressure gradient terms are. The body force in the cell P is split into two pressure jumps: one on the west face P_w^j and one on the east face P_e^j respectively. Eq. (2.9) can then be rewritten as

$$A_P U_P = \sum_P A_P^{nb} U_{nb} + (P_W - P_E) \frac{\Delta y}{2} + \left(P_w^j + P_e^j\right) \frac{\Delta y}{2}. \tag{2.21}$$

The pressure jumps are then treated in the same way as the pressure gradients for the derivation of the face velocity

$$U_e = \frac{1}{2} \left(\overline{U_P} + \overline{U_E}\right) + \frac{\Delta y}{A_e} (P_P - P_E) + \frac{P_e^j}{A_e} \Delta y, \tag{2.22}$$
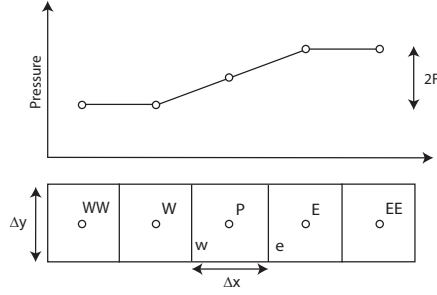
Figure 2.3: Pressure jump without wiggles.

where

$$\overline{U_P} = \sum_P A_P^{nb} U_{nb}, \quad \text{and} \quad A_e = \frac{1}{2}\left(A_P + A_E\right). \tag{2.23}$$

The Continuity Equation (2.6) then gives

$$\frac{1}{2}\left(\overline{U_E} - \overline{U_W}\right) + \frac{\Delta y}{A_e}\left(P_P - P_E\right) - \frac{\Delta y}{A_w}\left(P_W - P_P\right) + \frac{\Delta y}{A_e}P_e^j - \frac{\Delta y}{A_w}P_w^j = 0. \tag{2.24}$$

By applying the same simple case (uniform velocity and regular Cartesian mesh), a relationship between the pressure and the body forces if found. The Continuity, in Eq. (2.24), then gives

$$P_W + P_E - 2P_P = P_e^j - P_w^j. \tag{2.25}$$

Furthermore, by canceling the velocity terms, Eq. (2.21) gives

$$P_E - P_W = P_w^j + P_e^j. \tag{2.26}$$

Finally, combining Eq. (2.25) and Eq. (2.26) gives

$$P_P - P_W = P_w^j \quad \text{and} \quad P_E - P_P = P_e^j, \tag{2.27}$$

which is the correct result without pressure wiggles (see Fig. 2.3).

2.2.5 Implementation in EllipSys

The SIMPLE algorithm [65] of EllipSys uses the predicted velocity, obtained from the Momentum Equations, in order to find the pressure correction, through the Continuity Equation. This pressure correction is used to correct the predicted velocity so that it complies with the Continuity Equation (at this stage, it is then not complying with the Momentum Equation). The iteration goes on until the velocity converges to a solution that satisfies both

the Momentum Equations and the Continuity Equation.

The Continuity Equation can be expressed using the divergence operator

$$\overrightarrow{\nabla} \cdot \overrightarrow{\rho U} = 0. \tag{2.28}$$

Using the notation of Sørensen [89]-Eq.28 for a curvilinear grid, this equation can be rewritten as

$$\frac{1}{J} \left(\rho U \alpha_{\xi x} + \rho V \alpha_{\xi y} + \rho W \alpha_{\xi z} \right)_{\xi}$$
$$+ \frac{1}{J} \left(\rho U \alpha_{\eta x} + \rho V \alpha_{\eta y} + \rho W \alpha_{\eta z} \right)_{\eta}$$
$$+ \frac{1}{J} \left(\rho U \alpha_{\zeta x} + \rho V \alpha_{\zeta y} + \rho W \alpha_{\zeta z} \right)_{\zeta} = 0, \tag{2.29}$$

where ξ, eta and $zeta$ are the curvilinear coordinates, J is the Jacobian of the curvilinear to Cartesian transformation matrix and the α's are differential areas of the cell faces projected in the Cartesian coordinates. Equation (2.29) can be written in a more compact way ([89]-Eq.71);

$$\frac{1}{J} \left[(C_e - C_w) + (C_n - C_s) + (C_t - C_b) \right] = 0, \tag{2.30}$$

where $C_e = \rho_e U_e (\alpha_{\xi x})_e + \rho_e V_e (\alpha_{\xi y})_e + \rho_e W_e (\alpha_{\xi z})_e$.

The predicted velocity, derived from the Momentum equations, is composed of implicit terms $(A_{nb} U_{nb})$ and an explicit terms (S_{U-mom}) ([89]-Eq.65)

$$U_P = \frac{S_{U-mom} - \sum A_{nb} U_{nb}}{A_{P,U}}, \tag{2.31}$$

where the explicit terms S_{U-mom} contain the cross diffusion terms, the pressure terms and the body forces.

In order to apply the Continuity, it is necessary to find the velocity at the cell faces. The usual collocated approach is to interpolate the velocity U_P at the cell faces. This leads to the pressure wiggles, as explained previously. The idea of the Rhie-Chow algorithm is to separate the pressure gradient terms from the rest and to directly estimate them at the cell face,

$$\left(\frac{\partial P}{\partial x} \right)_e = \frac{1}{J} \left(\left(\frac{\partial P \alpha_{\xi x}}{\partial \xi} \right)_e + \left(\frac{\partial P \alpha_{\eta x}}{\partial \eta} \right)_e + \left(\frac{\partial P \alpha_{\zeta x}}{\partial \zeta} \right)_e \right). \tag{2.32}$$

The normal gradients are directly computed using a second-order accurate CDS ([89]-Eq.42)

$$\left(\frac{\partial P \alpha_{\xi x}}{\partial \xi} \right)_e = (P_E - P_P)(\alpha_{\xi x})_e. \tag{2.33}$$

The cross-term gradients are computed as the interpolation between two central difference approximations ([89]-Eq.43),

$$\left(\frac{\partial P\alpha_{\eta x}}{\partial \eta}\right)_e = \frac{1}{4}[(P_N - P_S) + (P_{NE} - P_{SE})](\alpha_{\eta x})_e \qquad (2.34)$$

$$\left(\frac{\partial P\alpha_{\zeta x}}{\partial \zeta}\right)_e = \frac{1}{4}[(P_T - P_B) + (P_{TE} - P_{BE})](\alpha_{\zeta x})_e. \qquad (2.35)$$

Therefore, instead of interpolating directly Eq. (2.31), the pressure gradient is estimated at the cell faces ([89]-Eq.69),

$$\begin{aligned}
U_e &= \overline{\left(\frac{S_{\overline{U}-mom} - \sum A_{nb}U_{nb}}{A_{P,U}}\right)}_e + \overline{\left(\frac{1}{A_P}\right)}_e\bigg[(\alpha_{\xi x})_e(P_E - P_P) \\
&\quad + \frac{1}{4}(\alpha_{\eta x})_e[(P_N - P_S) + (P_{NE} - P_{SE})] \\
&\quad + \frac{1}{4}(\alpha_{\zeta x})_e[(P_T - P_B) + (P_{TE} - P_{BE})]\bigg], \qquad (2.36)
\end{aligned}$$

where the first term in the Right Hand Side (RHS) is the linear interpolation at the cell face of all the momentum terms except the pressure gradient terms.

In the modification of the Rhie-Chow algorithm, the body forces are also extracted from the momentum terms. They are then transformed into pressure jumps located at each cell face in a similar fashion as proposed by Mencinger and Zun [60]:

$$\begin{aligned}
U_e &= \overline{\left(\frac{S_{\widetilde{U}-mom} - \sum A_{nb}U_{nb}}{A_{P,U}}\right)}_e + \overline{\left(\frac{1}{A_P}\right)}_e\bigg[(\alpha_{\xi x})_e(P_E - P_P) \\
&\quad + \frac{1}{4}(\alpha_{\eta x})_e[(P_N - P_S) + (P_{NE} - P_{SE})] \\
&\quad + \frac{1}{4}(\alpha_{\zeta x})_e[(P_T - P_B) + (P_{TE} - P_{BE})] + P_{e,x}^j\bigg], \qquad (2.37)
\end{aligned}$$

where $P_{e,x}^j$ is the pressure jump at the east cell face in the x-direction and $S_{\widetilde{U}-mom}$ is now the momentum source without the pressure terms and body forces.

In order to be consistent with the original body force applied in the cell, the pressure jump needs to satisfy the following property.

$$\iiint_V \overrightarrow{F} \; \mathrm{d}V = \iint_S \overrightarrow{n} \, P^j \; \mathrm{d}S, \qquad (2.38)$$

where V is the volume of the cell, S is the area of the cell's face and $\overrightarrow{n}$ is a normal vector to the cell's face. This relationship can be projected on the

Cartesian coordinate system and discretized over the current cell. For the x-direction, this corresponds to

$$F_{P,x} V_P = \sum_{nb} n_{nb,x} S_{nb} P_{nb,x}^j, \tag{2.39}$$

where nb are the neighbouring faces, S is the face surface area and V the cell volume, $n_{nb,x}$ is the normal vector of the face nb in the x-direction.
One solution to Eq. (2.39) is to weight each face accordingly to its normal vector and face surface area:

$$P_{nb,x}^j = \frac{F_{P,x} V_P n_{nb,x} S_{nb}}{\sum_{nb}(n_{nb,x} S_{nb})^2}. \tag{2.40}$$

The pressure jump contributions from the two cells adjacent faces are added up. The final pressure jump can then be used directly in Eq. (2.37)

$$P_{e,x}^j = \frac{F_{P,x} V_P n_{e,x} S_e}{\sum_{nb,P}(n_{nb,x} S_{nb})^2} + \frac{F_{E,x} V_E n_{e,x} S_e}{\sum_{nb,E}(n_{nb,x} S_{nb})^2}. \tag{2.41}$$

Finally, the forces used in the Momentum equations are recomputed at the cell center using the face pressure jumps and divided by two, so that each neighbouring cell carry out the pressure jump equally.

$$F'_{P,x} V_P = \frac{1}{2} \sum_{nb} n_{nb,x} S_{nb} P_{nb,x}^j \tag{2.42}$$

Therefore, the new $F'_{P,x}$ is not exactly the same as the original $F_{P,x}$. In practice, the force has been smeared over the nearest neighbouring cells, so that the pressure jump, corresponding to the body force, occurs at the cell faces.
The new face velocity can be used in the face mass flux coefficients from Eq. (2.30), which is then used to compute the pressure and to correct the velocity, in order to satisfy Continuity.

2.3 Force Correction Validation

Three cases, where the analytical solution is known, are used to validate the force correction algorithm. The infinite plane of force, where the flow cannot expand on the side, yields a jump of pressure at the position of the cells. The infinite ribbon, or actuator strip in 2D, is a force acting in opposition to the flow direction along a straight infinite ribbon. Finally, an analytical solution for a lightly loaded actuator disc model.

2.3.1 Infinite Plane

The test case is a channel flow similar to the example presented in the previous sections. The BCs are taken to be symmetric on the side, so that no expansion is possible. An homogeneous force, opposed to the flow direction, is applied along a line (in 2D) or a plane (in 3D) (Fig. 2.3.1). This setup ensures that the flow direction remains 1D and constant because of Continuity. Only the pressure is expected to vary along the domain, increasing discretely from one side to the other of the line/plane, as it was described in the previous sections.

The results from EllipSys, Fig. 2.3.1, are in agreement with the theory presented in the previous sections. Using the uncorrected algorithm, the pressure presents some wiggles, visibly damped after 5–6 cells both upstream and downstream of the jump. The velocity also presents wiggles on the same cells where the pressure fluctuates.

Using the pressure jump correction, the pressure follows a clean jump carried over three cells, in good agreement with the analytical solution. There are no visible wiggles on the pressure, nor on the velocity results.
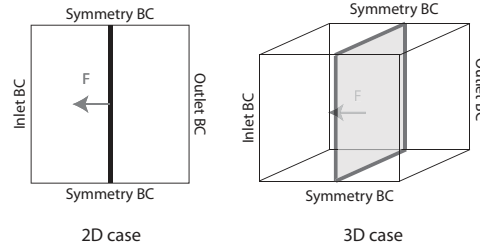
Figure 2.4: Infinite line/plane setup.

2.3.2 Infinite Ribbon

The second case considered is a 2D actuator strip under a rectangular inflow profile. In order to model it in 3D, the top and bottom faces of the domain are taken as symmetric BCs, while the north and south faces are taken as farfield BCs. The actuator strip is then represented as an infinitely long ribbon of homogeneous force going from the top to the bottom of the domain (see Fig. 2.3.2).

The analytical solution for lightly loaded actuator strip, was derived by
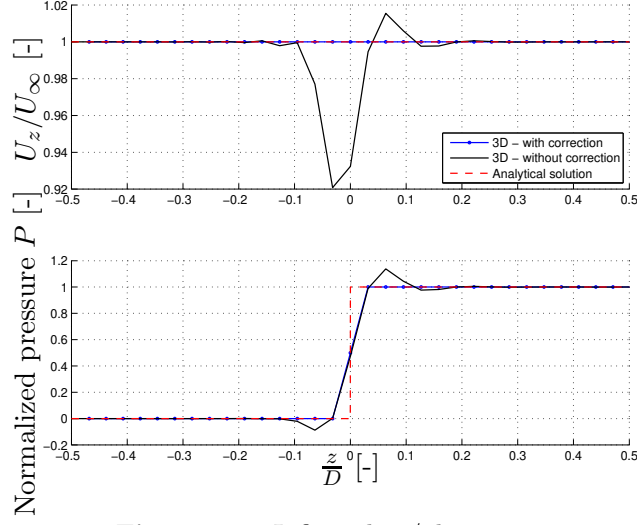
Figure 2.5: Infinite line/plane case.

Madsen [55],

$$p(x, y, \Delta p, D) = \frac{\Delta p}{2\pi} \left[\tan^{-1} \left(\frac{D/2 - y}{x} \right) + \tan^{-1} \left(\frac{D/2 + y}{x} \right) \right], \quad (2.43)$$

$$U_x(x, y, \Delta p, D) = U_\infty - \frac{p(x, y, \Delta p, D)}{\rho U_\infty} - \underbrace{\frac{\Delta p}{\rho U_\infty}}_{\text{only in the wake}}, \quad (2.44)$$

where D is here the actuator strip width, p is the pressure, Δp is the pressure jump, U_∞ is the inflow velocity and ρ is the density. In the derivation of Eq. (2.44), the Navier-Stokes Equations have been linearized. This assumption is only valid for a very lightly loaded actuator strip ($C_T \ll 1$).

Fig. 2.7 presents the normalized velocity and pressure in the x-direction along the centerline of the domain and in the y-direction at a position equivalent to $x = 1D$, where D is the width of the ribbon. The numerical results, using the correction, are in close agreement to the analytical solution. The difference for the pressure distribution in the y-direction is relatively small compared to the scale of the pressure jump. Similarly to the previous case, the numerical result without the correction presents significant velocity and pressure wiggles in the x-direction, both upstream and downstream of the position of the actuator strip. However, there are no visible wiggles in the y-direction.

2.3.3 Lightly Loaded Actuator Disc

The case of a lightly loaded actuator disc in 3D is studied. In order to model the flow appropriately, the BCs on the side faces (south, north, top, bottom)
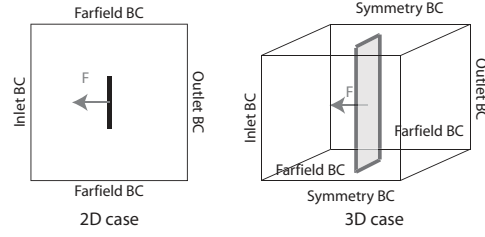
Figure 2.6: 2D actuator strip setup.

are taken as farfield (Fig. 2.3.3).

The analytical solution for an axisymmetric lightly loaded actuator disc in cylindrical coordinates (z, r), derived by Koning [47], can be numerically integrated using the following equations,

$$p(r, z, \Delta p, D) = \frac{\Delta p}{4\pi} \int_0^{D/2} \int_0^{2\pi} \frac{r'z \, \mathrm{d}r' \, \mathrm{d}\theta'}{\left(r'^2 + r^2 + z^2 - 2r'r\cos\theta'\right)^{3/2}}, \quad (2.45)$$

$$U_z(r, z, \Delta p, D) = U_\infty - \frac{p(r, z, \Delta p, D)}{\rho U_\infty} - \underbrace{\frac{\Delta p}{\rho U_\infty}}_{\text{only in the wake}}, \quad (2.46)$$

where D is the actuator disc radius, p is the pressure, U_∞ is the inflow axial velocity, ρ is the density and Δp is defined as

$$\Delta p = \frac{1}{2}\rho C_T U_\infty^2, \quad (2.47)$$

where C_T is the thrust coefficient.

The assumptions made to derive Eq. (2.45) and Eq. (2.46) are only valid for a very lightly loaded actuator disc ($C_T \ll 1$). The numerical results, using the correction, are also in good agreement with the analytical solution. The behaviour of the numerical results, without the corrected algorithm, is very similar to the previous actuator strip case. Velocity and pressure wiggles are clearly visible both upstream and downstream of the position of the body forces in the axial direction, yet not in the radial direction.
Note that the wiggles do not seem to affect the overall solution. They only produce an error at the local position of the actuator disc. It is nonetheless important to obtain a correct velocity and pressure at the actuator disc position, as this information can be used, for example, to determine the energy extracted by the wind turbine modeled using the actuator disc.
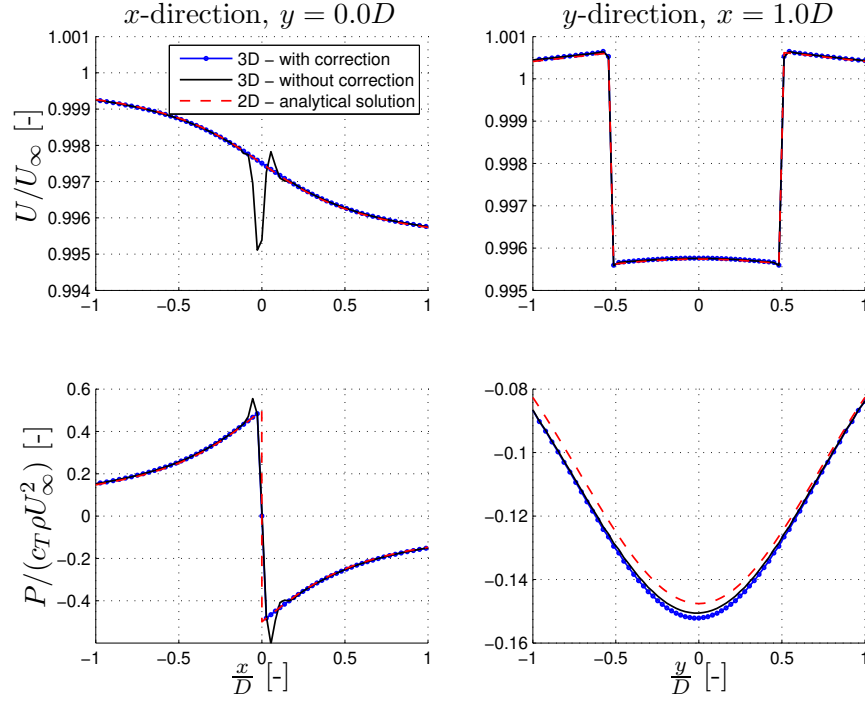
Figure 2.7: Infinitely long actuator ribbon (3D) compared to a 2D analytical solution for an actuator strip.

2.4   Summary

The force correction algorithm presented effectively removes the pressure wiggles that appear in the original model of Rhie-Chow when using discrete body forces. As it was visible in the example of the actuator strip, the wiggles just appear locally around the position of the forces and do not seem to have a very large influence after several cells. This effect is nonetheless highly non desirable when modelling wind turbines, as the forces applied against the flow using actuator discs are derived using the local velocity at the disc. If the velocities are incorrect at the disc because of the pressure-
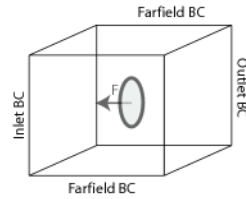
Figure 2.8: 3D actuator disc.
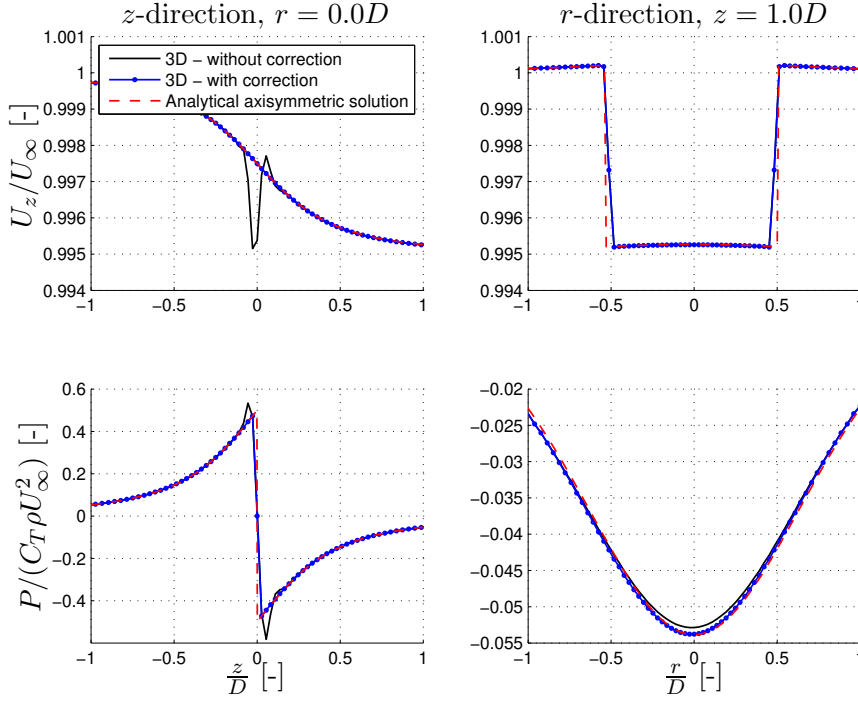
Figure 2.9: Actuator disc (3D) compared to an analytical axisymmetric solution.

velocity decoupling effect, then the forces are incorrectly estimated, which eventually affects the whole simulation.

While similar results were obtained previously using a Gaussian smoothing of the forces over several cells, the new method is able to apply forces successfully over only 3 cells without any numerical instability. Using this technique it is possible to increase the grid coarsening even at the position where the forces are applied, reducing significantly the total amount of cells needed for a computation. This improvement has a considerable effect for the computational cost of modelling wind turbines.

3

Actuator Shape Model

Contents

3.1 Introduction

In order to model wind turbines, there is a need for a model that is able to read the velocities at the surface of the wind turbine rotor and to apply the corresponding loading. The goal is to have a generic and flexible method that can adapt to different shape of rotors (e.g. coned, tilted, bended, winglets) and also do different modelling strategies (e.g. actuator disc, actuator lines, actuator surfaces). For this purpose, an Actuator Shape (AS) model is proposed. Given a geometry, the method is able to estimate the associated velocities at different locations on the shape, calculate a corresponding force and distribute it in the computational domain.

Because of the general formulation of the model, it can also have other applications. The actuator shape can be used to model any kind of immobile or mobile objects with a known drag force (e.g. tower, nacelle, buildings, forest, kites).

An indirect application of this formulation is to model dynamically atmospheric turbulence through an immerse boundary technique (Troldborg [96]). The fluctuating components of the velocity are enforced through the use of equivalent body forces. This application, based on the current model, was investigated by Gilling et al. [40].

Furthermore, as one goal of the model is to interpolate the velocity vector at different positions on a shape, the model can be used as an extraction tool for real time plotting and debugging.

The model is based on two levels of discretization. The shape by itself is defined by a grid with 3D coordinates. The second discretization is the intersection between the shape grid and the computational domain mesh.

A recursive algorithm detects the cells, which have intersections between the two meshes and it define the intersection polygons. The intersectional polygons are used during the simulation to transfer the forces of the shape inside the computational domain.

This double discretization of the shape has the advantage to have the shape grid and the computational mesh independently defined and still to preserve the correct distribution of the forces even when the meshes are coarse.

The emphasis of the following sections is placed on the description and the validation of the application of the actuator shape model as an actuator disc (AD). The actuator disc model is compared to two different wind turbine models. The first one is the heavily loaded analytical actuator disc model developed by Conway [24, 25]. The second one is a full CFD rotor computation of a Nortank turbine carried out by Zahle and Sørensen [101]. In each case, the same loading used in the models is distributed using the actuator shape model.

The results show a very good agreement between the proposed actuator shape model and the other two models.

3.2 Methods

The current section describes the necessary steps to initialize the model. First, the shape is discretized into shape cells and positioned in the domain. Then, each shape cell is linked to its respective domain cells. Finally the intersectional polygons are found between each couple of shape cell and domain cell.

From this definition, the model estimates the velocities at the position of the

shape points. These velocities are used to derive the equivalent forces. Finally the forces are redistributed in the domain cells using the intersectional polygons.

3.2.1 Shape Position and Discretization

The shape is positioned through three vectors. The first indicates the position of the shape center in relationship with the computational domain center. The second indicates the vertical direction of the shape in the computational domain. The third indicates the direction normal to the shape, in the computational domain. All three are variable and can be changed during the simulation to model the shape displacements.

The shape is discretized as a 3D surface where each element is a 3-point or a 4-point cell. One restriction imposed by the discretization is that each point of the cells is within the same plane. This restriction is given in order to easily find the intersectional polygons.
Each shape point coordinate is defined with respects to the shape center and located in the domain using the three position vectors.

3.2.2 Finding the Shape Points in the Domain Cells

During the initialisation phase, all the shape points are located inside the domain cells. The relationship tables between the shape points and the domain cells are then created. As the algorithm is multiblock and deals with actuator shapes that are split between several blocks, the initial step is to loop through all the domain blocks to see if the actuator shapes are inside. The search routine is based on a recursive dichotomy search of the DB in 8 independent parts. The algorithm then returns the association between one shape point with one domain cell. From this point, a recursive spreading search function is used to test all the association between the neighbouring shape points and the neighbouring domain cells.
This method has the advantage to reduce the number of search iteration. As the neighbouring cells are located physically close to one another, the recursive spreading technique reduces significantly the number of iterations needed to associate each shape cell with the corresponding domain cells.

3.2.3 Finding the Intersectional Polygons

A loop is done on each domain cell to find the intersectional polygon with each shape cell it have been associated with at the previous step. In order to construct the intersectional polygon, the algorithm searches for three types of points. The intersectional plane between each domain cell and each associated shape cell is found by looking for the intersectional points between each domain cell segment and the shape cell plane. The following
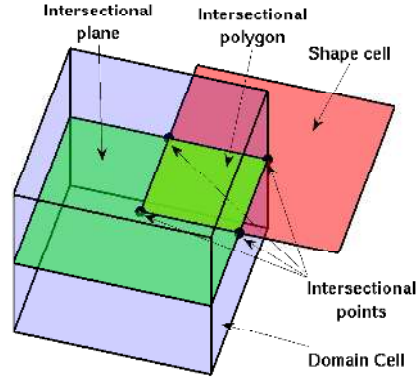
Figure 3.1: Illustration of the different elements considered in the intersectional polygon search algorithm.

step is to exclude all the intersectional points that are not located inside the shape cell and to add the rest to the intersectional polygon list of points. Then, the shape points that are located inside the domain cell are added to the intersectional polygon list. Finally, the intersectional points between the domain cell faces and the shape cell segments are also added to the intersectional polygon list.

Fig. 3.1 illustrates the different elements considered in this algorithm.

3.2.4 Interpolating the Shape Velocities

Each shape point has been associated with its corresponding domain cell in Section 3.2.2. Using the velocity in the center of the neighbouring domain cell, it is then straightforward to find the velocities in each shape point using a tri-linear interpolation technique.

The time consuming part of this algorithm is to identify the neighbouring domain cell centers and their respective interpolation coefficients, which are related to the distance between the shape cell and the neighbouring domain cell centers. If the point does not move from one iteration to another, the interpolation coefficients are stored for improving the speed. The method then uses only one loop for the number of shape points.

3.2.5 Estimating the Shape Forces

One of the advantages of this method is that any kind of force estimation model can be used. In the case of the actuator disc, the forces can be modelled using a simple drag coefficient in a similar way as it is done in the basic actuator disc theory. Two approaches can be followed. Each shape point

forces can be scaled according to the drag coefficient and the local velocity squared. Alternatively, the total thrust of the turbine can be estimated using the average velocity over the disc and redistributed proportionally according to the area of each shape cell, in order to reproduce the assumptions of the basic actuator disc theory.

More complex methods involving the use of the airfoil geometry and aerodynamic properties (Blade Element method, vortex method) have also been applied successfully in the literature (Ammara et al. [5], Mikkelsen [63]). In this work, however, in order to focus the study towards the fluid effects, the force model is kept as simple as possible.

In this chapter, the forces are directly extracted from the other wind turbine models. In the case of Conway's axisymmetric actuator disc model, the axial loading of the turbine is spread equally over the disc. In the case of the full-rotor computation, the time-history of the blade forces is averaged and spread equally over the disc.

In the following chapters, the forces are estimated by using the full-rotor computation forces as a local force coefficient scaled with the local normal velocities at the disc. While the load distribution is not expected to be realistic in all kinds of inflow, it gives a simple and flexible way to test different assumptions, which are used in the engineering models (e.g. the importance of the load inhomogeneity, of the wake rotation, of the fluctuating forces).

3.2.6   Redistributing the Shape Forces in the Domain Cells

Once the forces are estimated in each shape cell, their values are redistributed inside their associated domain cell. The procedure followed is to use the area of the intersectional polygons as a weight to proportionally redistribute the forces. This ensures that even if the discretization of the shape cells or the domain cells are coarse, the forces are split proportionally. Fig. 3.2a and 3.2b illustrate this method by presenting respectively the axisymmetric force distribution in the shape discretization on the left and the intersectional polygon areas between the shape cells and the domain cells, on the right.
Similarly, if the shape has not moved since the initialization, the intersectional polygons are kept in memory. The method is then processed using only one loop on the number of shape cells.

(a) Shape cells. The colour indicates the force by area of each shape cell.

(b) Intersectional polygons between the shape cells and the domain domain cells. The colour indicates the magnitude of the polygons area
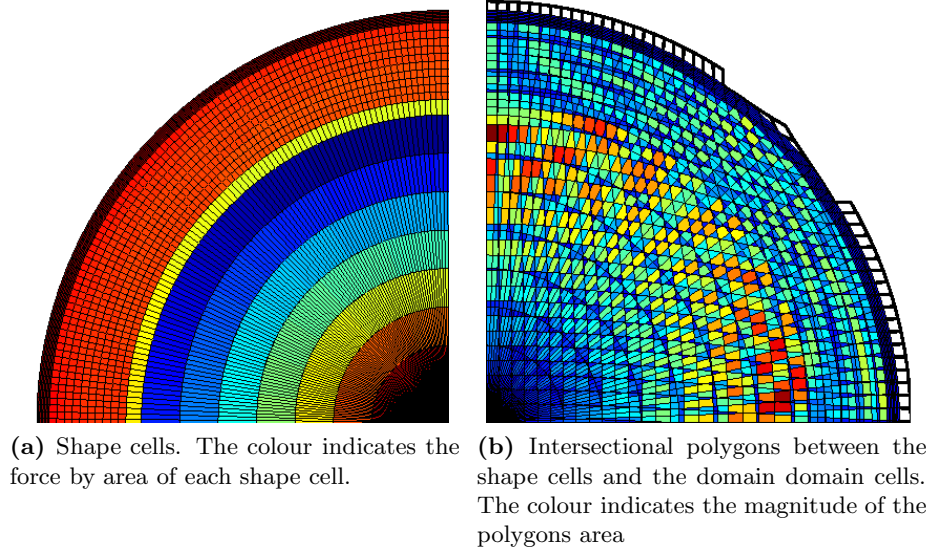
Figure 3.2: Force discretization algorithm.

3.3 Comparison to other models

3.3.1 Comparison to an analytical Solution for a Heavily Loaded Actuator Disc

The last case studied is a heavily loaded turbine, where the slipstream expansion is taken into account. In a series of articles [24, 25, 26, 78, 23], Conway has developed an exact actuator disc model for a heavily loaded propeller or a wind turbine. The model is based on the idea of axially discretizing the slipstream azimuthal vorticity of a wind turbine into vortex disks. As there are ways to express the flow behaviour induced by vortex disks, if the vortex distribution of the slipstream is known, it is possible to derive an exact formulation of the induced flow features.

This method is relatively complex to implement as it requires solving Bessel-Laplace integrals using recursive rules in order to get an expression in terms of complete elliptic integrals and other associated functions. This section presents a concise explanation on how to setup this solution and gives some analytical expressions needed to solve the special case of a parabolic wake profile.

The Special Case of a Parabolic Wake Profile

Conway has derived in [25] a solution for the special case of a parabolic wake profile including the slipstream expansion, where the vorticity distribution

is taken as

$$\omega_\phi = ar, \tag{3.1}$$

where ω is the vorticity, ϕ is the tangential direction, a is a free parameter and r is the radial coordinate. In this special case, the velocity profile in the ultimate wake is known to be

$$U_z(r,\infty) = U_\infty + a(R_\infty^2 - r^2)/2, \tag{3.2}$$

where R_∞ is the ultimate width of the slipstream. In this case, the stream function Ψ and the axial and radial velocities V_z and V_r can be found by solving,

$$\Psi(r,z) = \frac{U_\infty r^2}{2} + \frac{ar}{2}\int_0^\infty R_w^2(z')I_{(-1,2,1)}(R_w(z'),r,z-z')\,\mathrm{d}z', \tag{3.3}$$

$$U_z(r,z) = U_\infty + \frac{a}{2}\int_0^\infty R_w^2(z')I_{(0,2,0)}(R_w(z'),r,z-z')\,\mathrm{d}z', \tag{3.4}$$

$$U_r(r,z) = \frac{a}{2}\int_0^\infty \pm R_w^2(z')I_{(0,2,1)}(R_w(z'),r,z-z')\,\mathrm{d}z', \tag{3.5}$$

where $R_w(z)$ is the slipstream boundary radial position at an axial distance z the disc (also defined as the wake width function), U_∞ is the freestream inflow velocity and $I_{(\lambda,\mu,\nu)}$ is the Bessel-Laplace integrals (BLI) introduced by Conway [24] and defined as Eq. (3.6). The analytical expression of $I_{(-1,2,1)}$, $I_{(0,2,0)}$ and $I_{(0,2,1)}$, as well as the method used to derive them are described in the appendix.

$$I_{(\lambda,\mu,\nu)}(R,r,z) = \int_0^\infty e^{-s|z|}s^\lambda J_\mu(sR)J_\nu(sr)\,\mathrm{d}s, \tag{3.6}$$

where λ, μ and ν are integers and J_α are Bessel functions of the first kind. In order to find the wake width function $R_w(z)$, Conway proposes in the appendix of [25] a recursive method based on the idea that the stream function Eq. (3.3), is constant along the slipstream boundary, so that $\Psi\big(R_w(z),z\big) = \Psi(D/2,0)$.

Comparison to the Actuator Shape Model

The loads on the disc are estimated by Conway's model from the stream function Eq. (3.3), using Eq. (3.7) [25]. To implement them into EllipSys, they are distributed over a polar mesh and then inserted inside the computational mesh as described in Section 3.2,

$$L(r) = a\rho\Big[\Psi(R_T,0) - \Psi(r,0)\Big], \tag{3.7}$$

where L is the axial loading, a is the free parameter and ρ is the density.

(a) Axial velocity
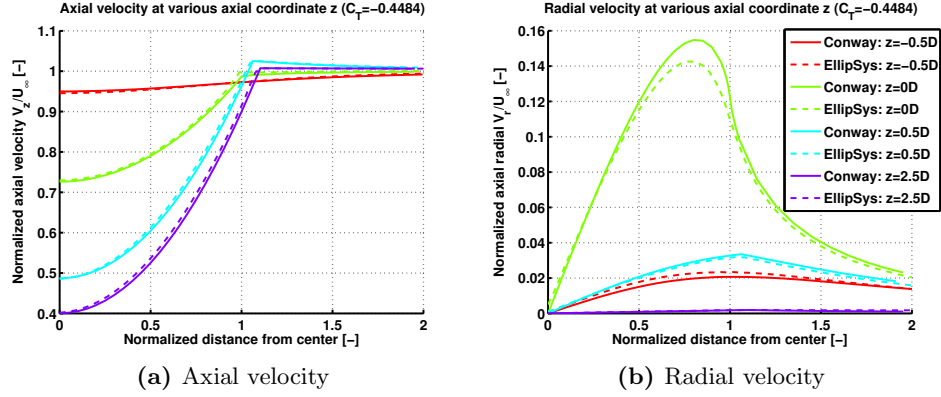
(b) Radial velocity

Figure 3.3: Actuator disc (parabolic wake case) compared to the analytical axisymmetric solution of Conway.

Fig. 3.3 presents the comparison of the CFD actuator disc model to Conway's heavily loaded actuator disc model. Conway's model uses a vorticity factor $a = -4U_\infty/D^2$, corresponding to $C_T = -0.4484$ applied in the CFD-AD. The model in EllipSys was used without any turbulence model in order to obtain a result close to the inviscid formulation of Conway.
The results show that the two models are in very close agreement, except for the radial velocity directly at the disc.

As it was commented by Schaffarczyk and Conway [78], who did a similar comparison, this difference probably comes from the fact that the CFD actuator disc model has a finite thickness, corresponding to the cell dimensions, while the model of Conway is infinitely thin. Moreover, the radial velocity evolves very rapidly at the disc position, which makes it difficult to precisely interpolate the velocities at the correct disc position.

3.3.2 Comparison to a Full Rotor Computation

In order to fully validate the actuator disc model, it is compared to a full rotor computation. The complete geometry of the rotor and nacelle of a Nortank 500 kW wind turbine is simulated up to a steady state solution by Zahle and Sørensen [101] using EllipSys and the k-ω SST turbulence model [61]. An illustration of the mesh used in the full rotor computation is presented in Fig. 3.4. In this computation, the emphasis is placed on the accurate definition of the flow that passes through the rotor. For saving computational cost, the mesh is then stretched in the wake region downstream of 3 rotor diameters. As it is based on an eddy-viscosity model, the full rotor computation does not perform well under atmospheric turbulence (see Section 5.5.4). For this reason, the inflow turbulence at the wind

turbine rotor is intentionally kept relatively low compared to atmospheric turbulence.
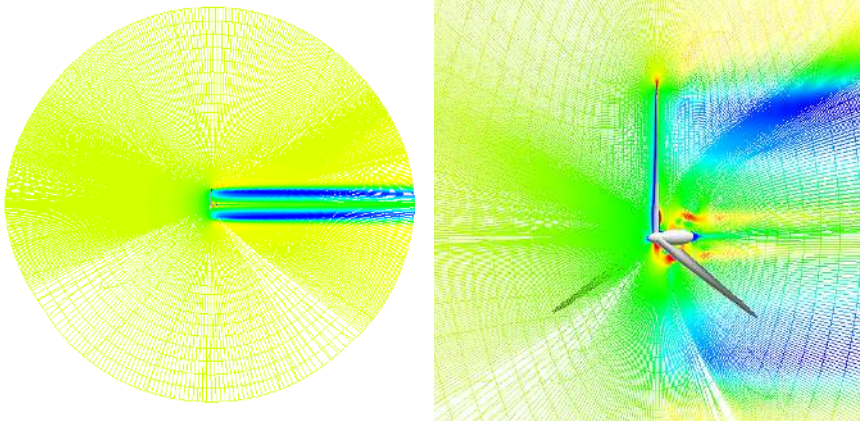
Figure 3.4: Illustration of the mesh surrounding the full-rotor computation. The colours illustrate the axial velocity magnitude.

The actuator disc model does not give a detailed description of the flow in the direct vicinity of the rotor blades. Instead, its application is to be used to model the far wake of a wind turbine. The region of comparison between the two kind of wind turbine flow model is chosen to be $x \in [-3D, -1D]$ and $x \in [1D, 3D]$. The same inflow parameters for both the mean velocity and the turbulence are used in the actuator disc model and the full rotor computation.

On Fig. 3.5, the axial U_x and tangential U_θ velocity components as well as the pressure are compared along the radial direction r, at different positions upstream and downstream of the rotor. The results are satisfactory in terms of mean velocity and pressure distribution.

However, the comparison in terms of turbulence parameters shows a large difference between the two models (not illustrated here). Indeed, the turbulence generated by the actuator disc lacks the detailed structures generated by the blade and nacelle geometry that still dominate in this region. The only turbulence generated by the actuator disc is produced through the mean velocity shear at the boundary of the wake. As the inflow turbulence is low, the production of turbulence is several orders of magnitude smaller than the turbulence generated by the blades and nacelle in the full rotor computation. Compared to atmospheric turbulence, the turbulence generated by the rotor is nonetheless an order of magnitude smaller and should
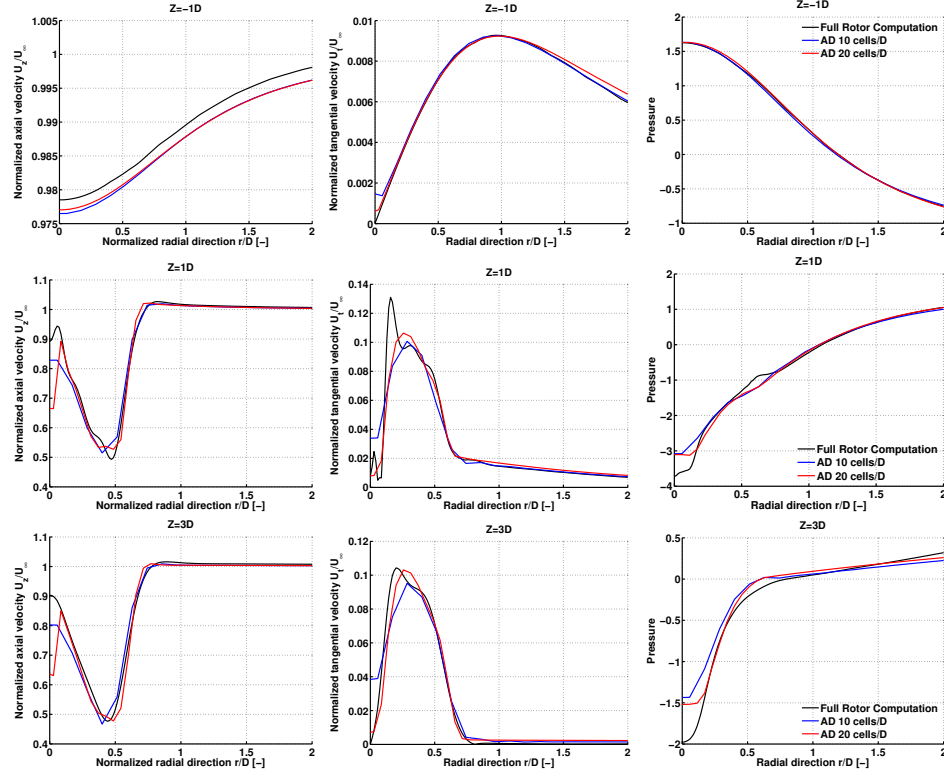
Figure 3.5: Comparison between the full rotor computation and the actuator disc model (with 10 and $20c/D$) of the normalized axial velocity in a cross section at hub height and at different positions upstream and downstream of the wind turbine.

not play a significant role in the far wake.

The difference between the two actuator disc computations (10 cells per rotor diameter (c/D) and 20 c/D) is is visible, yet remains relatively small. This indicates that using only $10c/D$ is enough for obtaining a good resolution of the close wake flow features. In the far wake region, the gradients become smaller and the cell size becomes less critical.

Using only $10c/D$ open the possibility to carry out large wind farm computations. For example an hypothetical cluster of 10×10 wind turbines (WT), with a wind turbine spacing of $8D$ in each direction needs roughly $10\,\text{WT} \times 10D \times 10c/D = 1000$ cells in the two horizontal directions. With 128 cells in the vertical direction, this roughly needs 128M cells in the center of the wind farm, in order to obtain a good resolutions. These types of steady-state simulations can be solved in less than 10 hours on a large computer cluster.

3.4   Summary

The actuator shape model is a flexible method for estimating and implementing forces inside the computational domain. The method was designed focussing on increasing the computational speed by reducing the number of iterations in order to find the shape discretization in the computational domain.

The actuator shape model implemented in EllipSys agrees very well with the analytical solution for heavily loaded actuator disc model of Conway. This demonstrates that the distribution and treatment of the forces is well implemented in the CFD flow solver. This result also confirms that the actuator disc model of Conway, originally designed for propellers, can be succeffully applied for the wind turbine cases.

The comparison between the actuator shape model of EllipSys and the full-rotor computation of EllipSys shows that the modelling of the wake of a wind turbine using forces is a good approximation at distances larger than a rotor diameter from the wind turbine. Nonentheless, the forces fail to model the small-scale turbulence generated at the blade location. This added turbulence can however be added as a source of turbulence at the disc location independently. The actuator disc model resolves reasonably well the close wake region, even with as little as 10 cells per rotor diameter, which opens the prospects of very large wind farm computations.

_4_

Comparison of k-ε and Measurements

Contents

4.1 Introduction

The force distribution and force treatment presented in the two previous chapters are implemented with the k-ε turbulence model to simulate a wind turbine in the atmospheric boundary layer.

The method followed to estimate the wind turbine forces is based on a local thrust coefficient multiplied by square of the local disc velocities. The atmospheric boundary layer is modeled using a simple wall function that enforces a neutral temperature stratification inflow case. Under these conditions, the main mean velocity component is fully logarithmic over all the domain, which corresponds to an eddy-viscosity linearly dependent with height.

The method is compared to single wind turbine wake measurements from Nibe [94] and Sexbierum [22]. These two data sets have been compared extensively in the literature to wake models. Each represent a wind turbine with met.mast measurements at different locations upstream and downstream.

The comparison shows a large discrepancy between the measurements and the standard k-ε model. In k-ε , the mean velocity does not reach the same wake deficit in the close wake region and recovers much faster than in the measurements. Furthermore, the turbulence kinetic energy and the eddy-viscosity build up in an unrealistic fashion upstream of the wind turbine. Similar comparisons carried out by El Kasmi and Masson [35], Cabezon et al. [18] and Rados et al. [68] have drawn similar conclusions.

Different artificial inflow conditions, where the eddy-viscosity is controlled independently from the other parameters, are tested and compared to the basic actuator disc. There is a direct dependency on the velocities at the disc and the background eddy-viscosity. A threshold value is found for an eddy-viscosity of $\mu_{tsh} = 0.1$, by doing a parametric study over the disc velocities. This value gives encouraging prospects regarding the validity of using LES methods to physically model wind turbine wakes using actuator disc models.

4.2 Methods

4.2.1 Force Estimation

The method used to model the wind turbine is the actuator disc model, as it was presented in Chapter 3. The forces are estimated using the local velocities at the disc. The forces are estimated using is a drag force model, where the drag coefficients, are predefined

$$\mathbf{F} = -\frac{1}{2}\rho A \mathbf{C_D}(\mathbf{U} \cdot \mathbf{n})^2, \tag{4.1}$$

where $\mathbf{n}$ is the normal vector to the disc and $\mathbf{C_D}$ is a vectorial force coefficient that is function of the position relative to the center of the disc.

In this chapter, the drag coefficients used are found using a full rotor computation on the Nordtank 500 kW turbine, as described in Section 3.3.2. The advantage of using this method is that the force distribution along the disc are relatively physical. There is for example a reduction of the velocities at the blade roots and tips. Furthermore, the tangential forces, which model wake rotation, are also present.
While more complicated Blade Element (BE) methods are relatively easy to

implement, they need airfoil data, which are not always available. Moreover, the details of the force distribution are not expected to play an important role on the wake development further than $1 - -2$ rotor diameters.

4.2.2 Turbulence Modelling

In order to model the atmospheric boundary layer turbulence, the law-of-the-wall BC is used at the ground. This standard method, based on the balance between the wall roughness turbulence production and the dissipation, is well known and is fully described in Sørensen [89]. This method produces a neutrally-stratified logarithmic mean velocity Eq. (A.18), p.140.

4.2.3 Numerical Considerations

The inlet and top BCs of the domain, are set to the atmospheric values defined as Eq. (A.18), (A.19) and (A.20). The outlet BC and the side farfield BC are both based on the assumption of fully developed flow (non-gradient flow). The model constants are the standard values used in EllipSys (listed in table A.1, p. 140). However, the C_μ value is used as a parameter in order to obtain the same inflow turbulence as in the measurements. The $C_{\epsilon 1}$ is adapted to the change of C_μ with Eq. (A.23).

The domain is discretized in order to obtain 10 cells per rotor diameter and is stretched at the boundaries to have the smallest cells where the gradients are large (i.e. very small cells at the wall BC and very large cells at the top, side and outlet BCs).
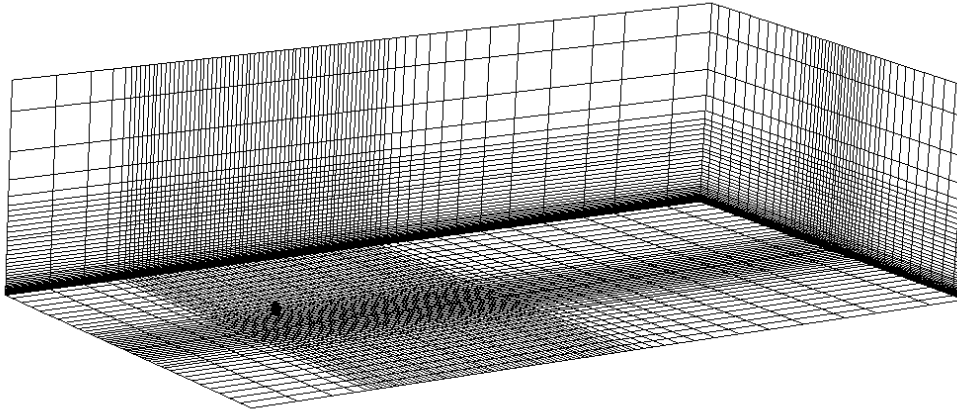

Figure 4.1: Illustration of the k-ε mesh. Only 1 out of 3 cells are represented. The actuator disc is also visible.

4.3 Measurements

The two data set available for this project are the Nibe B turbine [94] and the Sexbierum wind farm [22].

The Nibe wind turbine is located in Denmark. Four meteorological masts were placed at different position behind the wind turbine ($x = 2.5D$, $x = 4D$, $x = 6D$ and $x = 7.5D$). In the measurements considered one wind turbine located between the met.mast $x = 4D$ and met.mast $x = 6D$ was stopped in order to study a single wake case. However, the drag force of this stand-still turbine should to be considered in the interpretation of the measurements. For this reason, the met.mast ($x = 6D$), located directly downstream of the stopped turbine, is taken out of the analysis.
A similar comparison is carried out using the Sexbierum wind farm data set. Three met.masts were placed downstream of a wind turbine ($2.5D$, $5.5D$, $8D$).

The computational setups used to compare the wind turbine wake model and measurements are given in Table 4.1.

Table 4.1: Setup description.

Location	D	z_H	C_T	z_0	$U_{\infty,H}$	c/D
	[m]	[m]	[-]	[m]	[m/s]	[-]
Nibe	40.0	45.0	0.85	0.100	8.0	10
Sexbierum	35.0	40.0	0.75	0.049	8.0	10

Note that the measurement campaigns have been carried out between 15–20 years ago and are based on wind turbine sizes which are not relevant with the large offshore wind turbine installed nowadays. It would be interesting to have more inflow cases and measurement locations downstream of the wind turbines.

4.4 Main results

Fig. 4.3a and Fig. 4.2b present the comparison of the standard k-ε model to the measurements from Nibe and Sexbierum. As it can be seen, the general trend of the result is that the standard k-ε model largely overpredicts the wake recovery compared to the measurements. The closest met.mast downstream of the wind turbine indicates a much larger wind speed deficit in both data sets.
Similar results were obtained by El Kasmi and Masson [35], Cabezon et al.[18]

and Rados et al [68].

(a) Normalized axial velocity profile by inflow hub height velocity $\frac{U}{U_\infty}$

(b) Normalized axial velocity centerline by inflow hub height velocity $\frac{U}{U_\infty}$
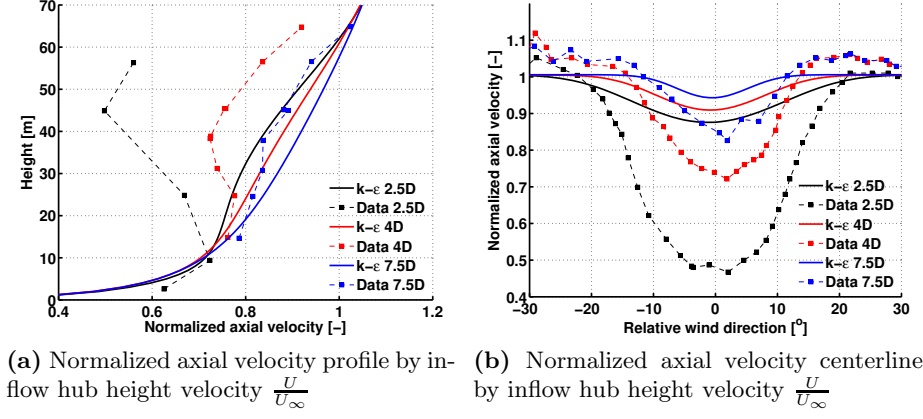
Figure 4.2: Axial velocity in the wake of the Nibe B wind turbine.

(a) Normalized axial velocity by inflow hub height velocity $\frac{U}{U_\infty}$

(b) Normalized turbulent kinetic energy by local axial velocity $\frac{k}{U^2}$
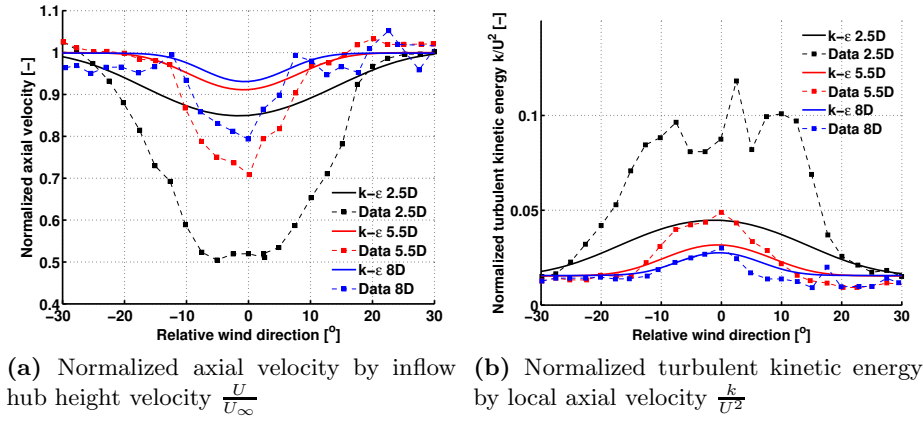
Figure 4.3: Axial velocity and turbulent kinetic energy measured in the wake of a wind turbine at Sexbierum wind farm.

Fig. 4.4 indicates that k has a sudden increase at about half a rotor diameter upstream of the wind turbine. A similar trend can be observed for the eddy-viscosity.

Another interesting observation is to notice that the velocities at the disc are significantly larger than those estimated from the basic actuator disc theory (Hansen [42]),

$$U_D = (1-a)U_\infty, \quad \text{with} \quad a = \frac{1}{2}\left(1 - \sqrt{1-C_T}\right), \qquad (4.2)$$
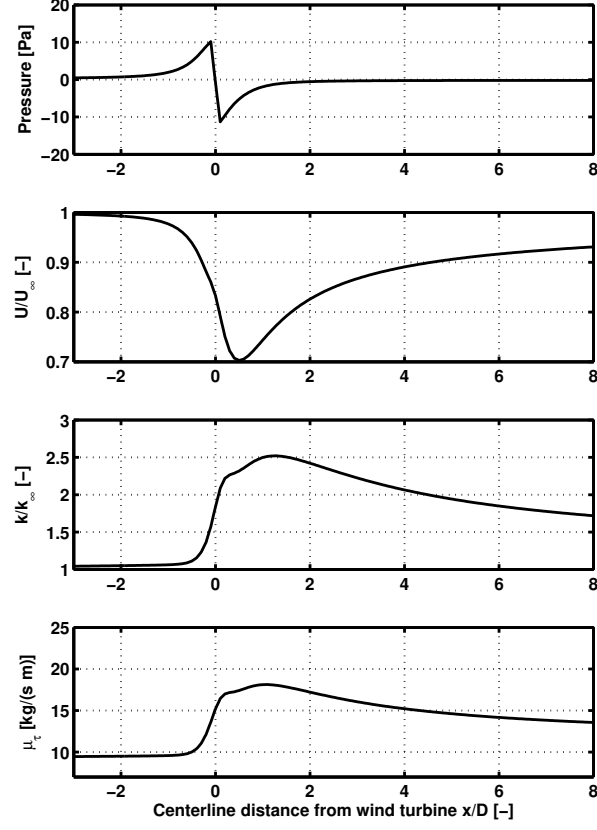
Figure 4.4: Pressure, axial velocity, turbulent kinetic energy and eddy-viscosity along the centerline passing through a wind turbine at the Sexbierum wind farm.

4.5 Discussion

The effect of turbulence over the mean velocity is implemented in the Navier-Stokes Equations as a sink of momentum associated to the Reynolds-stresses. Consequently, an underestimation of the mean velocity wake deficit, as it is seen in comparison to the measurements, implies an overestimation of the Reynolds-stresses. In the k-ε model and more generally in most of the eddy-viscosity models, the Reynolds-stresses are functions of the eddy-viscosity and the strain-rate tensor $\overline{S}_{ij}$ Eq. (A.11), p.139. This indicates that the eddy-viscosity is overpredicted in the standard k-ε model for the case considered.

In order to check if the eddy-viscosity is overpredicted, a similar computation is carried out, yet this time imposing a constant eddy-viscosity over the domain, defined as $\nu_t = \kappa u^* z$, independent from k and ε.
In this computation, the velocities at the disc decrease compared to the standard k-ε computation and the wake is slightly more pronounced. However, the velocities remain significantly higher than those from the basic actuator disc theory or the measurements.

This observation indicates not only that the eddy-viscosity should not increase as much as it does in the standard k-ε model, but also that it should actually be smaller than the atmospheric values in the region surrounding the rotor. In order to estimate the order of magnitude of the maximum eddy-viscosity that would give physical rotor velocities, a parametric study is carried out over the eddy-viscosity.
To simplify the problem, the inflow velocity is taken as uniform, the actuator disc is uniformly loaded, the turbulence model is switched off and the molecular viscosity is increased to simulate the effect of the eddy-viscosity over the mean momentum. Increasing the molecular viscosity gives the same effect to having a constant eddy-viscosity all over the domain. This artificial eddy-viscosity is referred in the following sections as an "equivalent eddy-viscosity".

Six different equivalent eddy-viscosities are illustrated on Fig. 4.5. The atmospheric eddy-viscosity at hub height is of the same order of magnitude as Fig. 4.5 e). In that case, the mean axial velocity has qualitatively the same behaviour.
On Fig. 4.6, the deviation of the axial induction factor at the disc from with the theoretical one Eq. (4.2), is plotted for the different equivalent viscosities. There is a visible threshold value after $\mu_{tsh} = 0.1$, where the axial induction factor becomes more and more different from the theory.

The eddy-viscosity based on the Boussinesq approximation is estimated to be linearly dependent with height. Eq. (A.18) can be rewritten as a function of the roughness and the velocity,

$$\nu_t = \frac{\kappa^2 U z}{\ln\left(z/z_0\right)}. \tag{4.3}$$

Based on Eq. (4.3), Fig. 4.5, illustrates how far the standard k-ε eddy-viscosity is from the threshold value for different hub height and different surface roughnesses. Note that the hub heights of a modern offshore turbine is located higher than $z_H = 70$ m and the water roughness is at least $z_0 = 10^{-6}$ m. In those conditions, the eddy-viscosity is roughly two orders of magnitude larger than the threshold value.
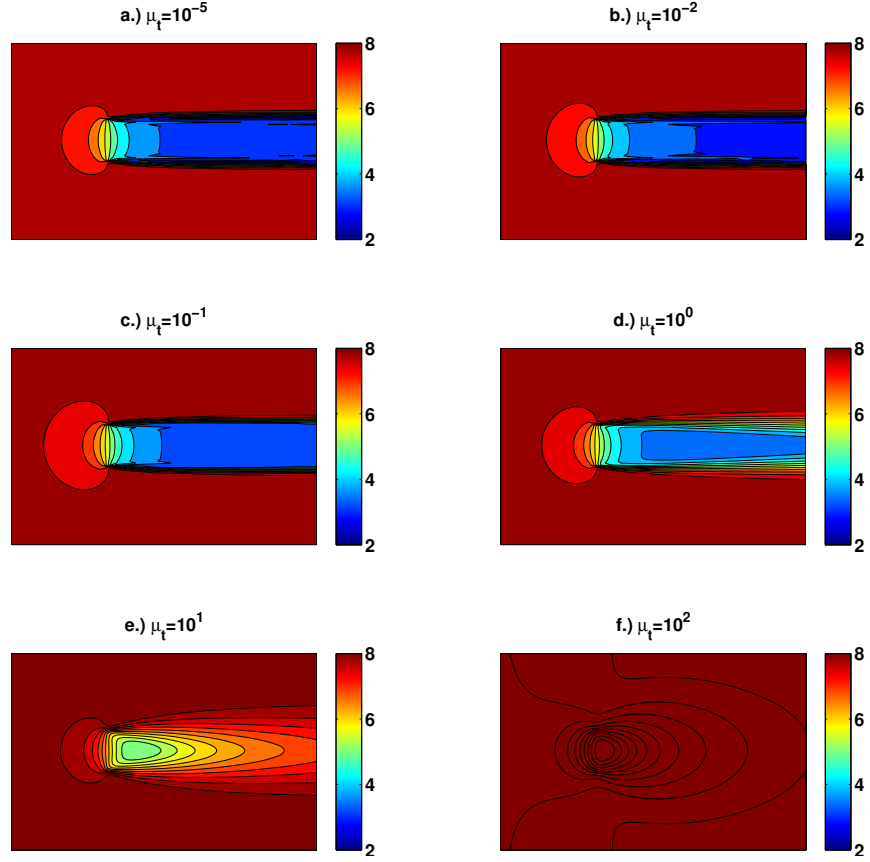
Figure 4.5: Illustration of 6 identical uniformly loaded actuator discs ($U_\infty = 8.0$m/s, $C_T = 0.85$) under different equivalent viscosities. The turbulence effect is modelled by increasing the molecular viscosity. The colors represent the axial velocity [m/s].

All these observations indicates that the k-ε model inappropriately treats the large-scale turbulence for wind turbine flow applications. The threshold value found for the eddy-viscosity can be used as a design parameter to perform a LES analysis. In LES, the eddy-viscosity is only used to model the action of the small-scale turbulence and ν_t is typically a fraction of the grid cell size. If the cell size is taken small enough to obtain an eddy-viscosity lower than the threshold value found previously, the LES results should be unaffected by the same problem observed for the standard k-ε model.
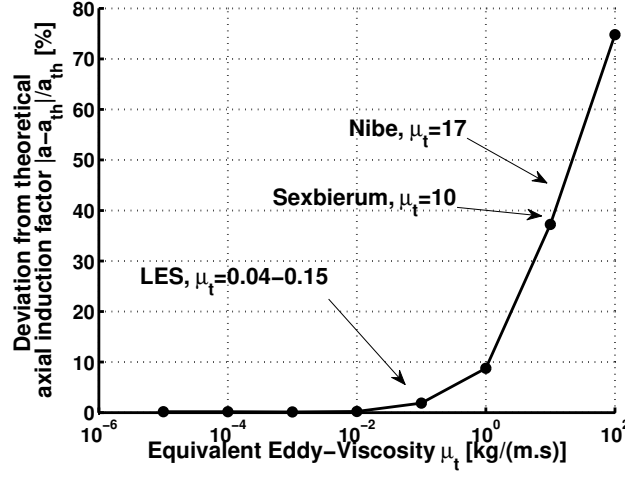
Figure 4.6: Parametric study of the axial induction factor a for different equivalent inflow eddy-viscosities. The y-axis represents the deviation of a compared to the theory a_{th} Eq. (4.2).

4.6 Summary

A standard k-ε model have been applied to simulate a wind turbine wake flow. The results show that the mean velocities are significantly overestimated compared to wind turbine wake measurements. A parametric study of the eddy-viscosity shows that there is a threshold value. Higher than this eddy-viscosity threshold value, the turbulence model overestimates the velocities at the disc. This value is nonetheless large enough to enable LES of wind turbine wake. This kind of turbulence model can give valuable insight on the turbulence behaviour in the vicinity of wind turbines and can potentially help the development of a set of correction that enable the modelling of wind turbines flow using k-ε.
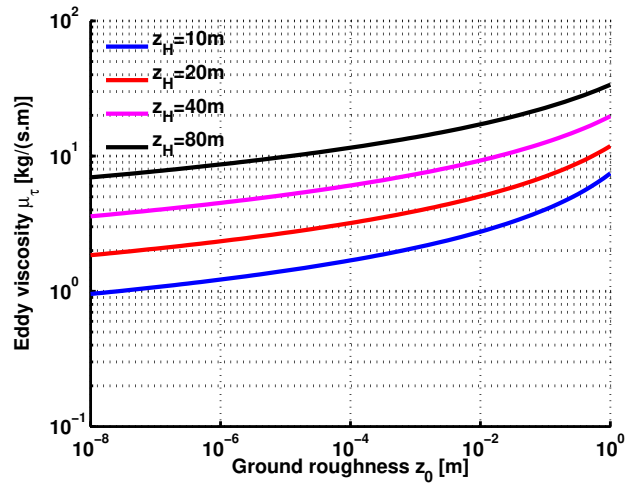
Figure 4.7: Different eddy-viscosities as function of roughness length (z_0) and hub height (z_H) for a velocity of 8m/s, based on Eq. (4.3).

5

Comparison of k-ε and LES

Contents

5.1 Introduction

In the previous chapter, the k-ε model was found to perform poorly for wind turbines in atmospheric flow cases, in comparison to measurements. However, a parametric study performed on the eddy-viscosity showed that the error made in k-ε is negligible for eddy-viscosities under a threshold value $\mu_{tsh} = 0.1$.

A LES splits the turbulence into two parts, the large-scale turbulence and the small-scale turbulence and treats them differently. The large-scale turbulence is fully resolved as a time-series, while the small-scale turbulence is modelled using a so-called subgrid-scale (SGS) turbulence model. Bechmann [11] has developed a LES model, based on a k-ε SGS turbulence model for EllipSys that was designed to perform complex terrain simulations. As the SGS-k-ε model only models the small-scale turbulence, the eddy-viscosity remains bounded to relatively small values. The free-stream atmospheric value for the eddy-viscosity is proportional to the mesh's cell size Eq. (A.30). With a fine discretization, LES can operate under the eddy-viscosity threshold value μ_{tsh}. For this reason, the LES model should not have the same short-comings as the k-ε concerning atmospheric flows. Comparing the result of the LES to k-ε could, therefore, give an in-depth understanding of the modelling issues of wind turbine wake with k-ε.

The k-ε model has been introduced in the previous chapter and the governing equations are given in the Appendix A.4. The LES model used is fully described in Bechmann [11]. Section 5.2 focuses on how to compare steady-state k-ε results to unsteady LES time-series. Section 5.3 presents the numerical aspects of the two kind of simulations. Section 5.4 compares some of the main results of the LES and k-ε.

While the two turbulence models have comparable inflow conditions, they behave very differently in the region surrounding and downstream of the wind turbine. In order to fully understand where these differences come from, the Discussion section 5.5 studies the main assumptions made by the k-ε and confront them with the LES results. The eddy-viscosity concept and the pressure-velocity correlation in the k and ε-equations are found to perform poorly in the region surrounding wind turbines. These assumptions are believed to be the main source of error in the k-ε simulation of wind turbine in atmospheric flows.

5.2 Methods

5.2.1 LES

Bechmann [11, 12] has developed an hybrid LES-RANS turbulence model for EllipSys. While other models have to generate the inflow turbulence through a statistical model (Troldborg [96] uses the Mann model [57]), Bechmann's model is able to simulate directly the atmospheric boundary layer turbulence generated from the surface roughness length. The idea is that the small-scale turbulence, which is usually modelled using a Smagorinsky model [?], are modelled using a more sophisticated SGS model which automatically switch between the Smagorinsky model and the k-ε model in the wall region. As the k-ε is better at modelling the wall region, the LES model a obtain more realistic atmospheric behaviours. The inflow turbulence is generated using a precursor mesh with periodic BCs at the inlet and outlet and is run for a large number of iterations until the turbulence is statistically representative with atmospheric values.

However, the disadvantage of this method, is that generating the inflow turbulence is computationally expensive. Running the precursor mesh can take several weeks on large computer clusters (see Bechmann [11]). Fortunately, a precursor mesh, used in a previous project, was available and was appropriate for modelling a single wind turbine wake.

5.2.2 Steady and Unsteady forces

With LES, it is possible to compare the influence of a steady and an unsteady force distribution. An unsteady force distribution depends on the local instantaneous velocities at the disc and can be modelled using the same method presented in Section 4.2.1 $\mathbf{F}(\mathbf{U_D})$.

A steady force distribution does not depend of the local instantaneous velocities and is constant over the time. It is the equivalent force that would be applied in a steady-state k-ε computation.

There are two methods to estimate the steady force distribution from LES. The unsteady force distribution can be averaged over time $\overline{\mathbf{F}(\mathbf{U_D})}$. Otherwise, the time-averaged mean velocity field generated using an unsteady force distribution can be used to estimate the equivalent steady force distribution $\mathbf{F}(\overline{\mathbf{U_D}})$ in a similar fashion to a steady-state k-ε.

5.2.3 Resolved LES eddy-viscosities

Two definitions are used to estimate the resolved LES eddy-viscosity. The first one, ν_t^{LES1}, is based on the k-ε definition,

$$\nu_t^{LES1} = C_\mu^{LES} \frac{k^2}{\varepsilon}. \tag{5.1}$$

where C_μ^{LES} is the eddy-viscosity constant used for the LES (see Table A.2), k is the resolved LES TKE Eq. (A.31) and ε is the resolved LES dissipation Eq. (A.32).

The second one, ν_t^{LES2}, is based on the eddy-viscosity concept Eq. (A.11), using the time-averaged resolved Reynolds-stresses tensor $\overline{u_i'u_j'}$ directly estimated from the computation and the mean strain rate tensor $\overline{S}_{ij}$ Eq. (A.3), This method is inspired from the eddy-viscosity concept:

$$\nu_t^{LES2} = \frac{1}{2}\frac{||R||}{||S||}, \tag{5.2}$$

where $||R||$ and $||S||$ are defined as:

$$||R|| = \sqrt{\left(\frac{2}{3}k\delta_{ij} - \overline{u_i'u_j'}\right)\left(\frac{2}{3}k\delta_{ij} - \overline{u_i'u_j'}\right)}, \tag{5.3}$$

$$||S|| = \sqrt{\overline{S}_{ij}\overline{S}_{ij}}. \tag{5.4}$$

Based on these two definitions, it is possible to define the eddy-viscosity factor C_μ^*,

$$C_\mu^* = \frac{||R||}{2||S||}\frac{\varepsilon}{k^2}. \tag{5.5}$$

5.2.4 Resolved LES Reynolds-stresses

The Reynolds-stresses can be either estimated directly by time-averaging of the square of the velocity fluctuations, Eq. (5.7)

$$\overline{u_i'u_j'} = \overline{U_iU_j} - \overline{U}_i\overline{U}_j, \tag{5.6}$$

or through the eddy-viscosity concept, using ν_t^{LES1},

$$R_{ij}^{LES} = \frac{2}{3}k\delta_{ij} - 2C_\mu^{LES}\frac{k^2}{\varepsilon}S_{ij}. \tag{5.7}$$

5.3   Setup description and numerical aspects

5.3.1   Setup

The same wind turbine is modelled using LES and k-ε. The wind turbine is similar to the Nibe turbine and is described in Table 5.1.

Two LESs are carried out, one with forces adapted to the local velocities (referred as "LES, Variable Forces" or LES_{VF}) and the second one with the time average force distribution of the first LES (referred as "LES, Constant Forces" or LES_{CF}).

The time series are averaged over 3000 iterations to obtain a steady-state comparable result.

The turbulent inflow is generated using a precursor simulation performed by Bechmann [11] according to the wind speed and roughness described in Table 5.1.

5.3.2   Meshes

The Mesh used for the k-ε computation is the same as presented in section 4.2.3. However, the mesh used for the two LESs is different. The mesh is gradually refined at the ground BC in order to obtain the details of the gradient and is modelled using a standard wall-function. The sides have a periodic BC, while the top has a symmetric BC.

The domain dimensions are 1200 m × 600 m × 200 m. The wind turbine is placed at the position (300,300,45). The stretching in the x-direction begins at 850 m from the inlet, which is 550 m downstream of the wind turbine (see Fig. 5.1). This gives a region of more than 13 rotor diameters for the wake study. In practice, the periodic BC on the side, do that the setup models an infinite column of wind turbines spaced at 600 m ($15D$) from each other. The spacing between them is nonetheless expected to be large enough to avoid having an influence over the region of study ($13D$).

This setup models an atmospheric flow with a boundary layer corresponding to the height of the domain (200 m). The symmetric BC at the top intentionally reduces the turbulence intensity in this region by damping all the fluctuations coming upwards. The relatively small height of the domain also makes it economical and feasible to have small cells and consequently

Table 5.1: Setup description.

D	z_H	C_T	z_0	$U_{\infty,H}$	c/D
[m]	[m]	[-]	[m]	[m/s]	[-]
40.0	45.0	0.85	0.0001	11.0	10
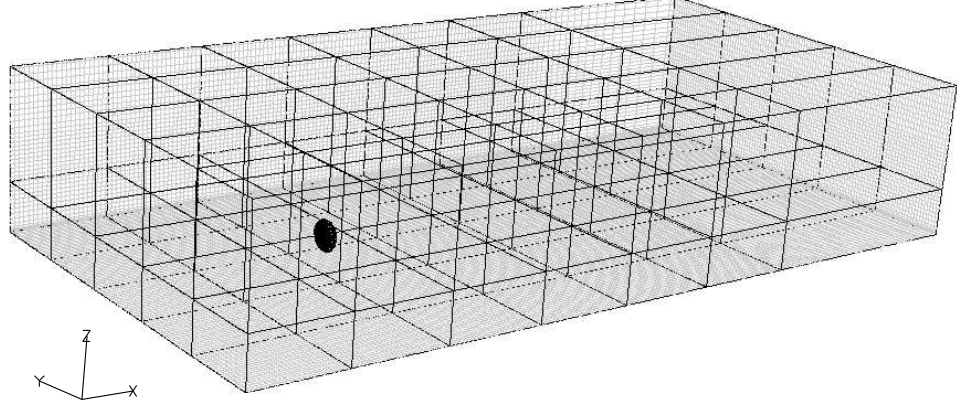
Figure 5.1: Illustration of the LES mesh. Only 1 out of 3 cells are represented. The different blocks used are visible in black lines. The actuator disc is also visible.

a small eddy-viscosity. The maximum cell size is then $\Delta = 4$ m.

The mesh is decomposed in blocks of 64^3 cells. The whole domain has the dimension of $7 \times 5 \times 2$ blocks ($448 \times 320 \times 128 > 18.35$M cells).

The time step is set to $\Delta t = 0.025$ s. The solving time of the LES for 9000 iterations (225 s) is about 4 days on 70 CPUs. However, the k-ε simulation takes only a couple of hours to converge to acceptable residuals on 64 CPUs.

5.3.3   Limitations of the comparison

Unfortunately, the surface roughness and the inflow conditions of the precursor mesh available were not compatible with the wake measurements test cases and, therefore, the LES results could not be directly compared with them.

The inflow time-series that could be extracted from the precursor mesh were limited to 10,000 iterations with a time step of $\Delta t = 0.025$ s, representing roughly 4 minutes. Of these 4 minutes, 2–3 minutes were needed to fully initialize the domain, which left slightly more than 1 minute (3000

iterations) for doing statistics. Because of this situation, the inflow resolved turbulence is found to be significantly smaller compared to a longer time series. Fig. 5.2 illustrates this issue by comparing the average turbulence intensity in the precursor mesh over 1–4 minutes. The 4-minute statistics converge towards the analytical solution. However, the 1-minute statistics have a factor 10% lower than the analytical solution.

A RANS model averages the variables over an infinite long time. It is, therefore, supposed to represent all the fluctuation-scales. However, the LES precursor mesh only produces statistics over fluctuation-scales lower than 1-minute. While the k-ε is able to give a TKE solution close to the logarithmic values, the LES gives a significantly lower inflow condition.

In the case of a wind turbine flow, the time-scales larger than 1-minute should mainly contribute to the meandering of the wake structure, which becomes important in the far wake region. In the close wake region, the "very" large-scale turbulence does not play an important role in the wake development.
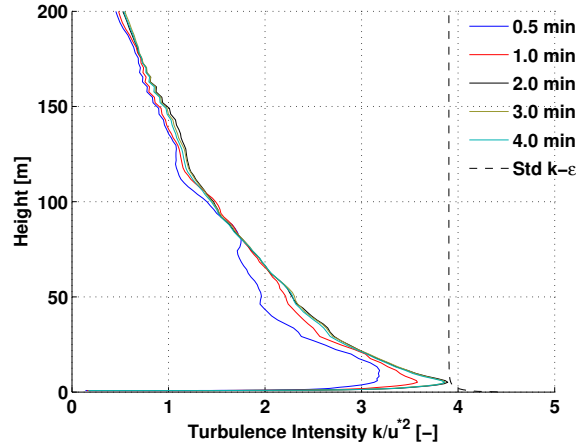
Figure 5.2: LES turbulence intensity for different averaging times in comparison with the standard k-ε turbulence intensity.

The differences in the meshes between the LES and the k-ε also yields constraints regarding the comparison of the two models. The LES mesh has a relatively small height (200 m), with symmetric boundary condition, which reduces the TKE with height. On the contrary, the k-ε mesh has a larger height (500 m), with a inlet BC. This setup generates a constant TKE with height. Combined with the short time statistics of the LES, the TKE at hub height is significantly different in the two simulations.

As the turbulence level of the two models is different, the results cannot be directly compared and only the main trends and features of the two models can be analyzed.

5.4 Main results

5.4.1 Mean velocities

Fig. 5.3 and Fig. 5.4 show the vertical and horizontal profiles of the axial velocity in a centerline passing through the center of the rotor at hub height at different positions upstream and downstream of the wind turbine. Fig. 5.6 shows the axial velocity over an horizontal plane at hub height.
The LES_{VF} mean axial velocity progressively decreases until an inflexion point, located $x = 3.0D$, where the wake begins to recover (Fig. 5.6). The LES_{CF} mean axial velocity has an inflexion point around $x = 1.6D$. However, the 90% recovery point is roughly the same in both simulations. The k-ε model predicts a wind speed recovery inflexion point occurring at $x = 0.22D$ rotor diameters downstream of the wind turbine. Following this point, the recovery is completed at 90% at $x = 6.0D$. Note that these values are dependent on the position of the extracted line and should be taken as a trend comparison only.

The two LESs have a similar trend between each other in contrast to the k-ε computation. One noticeable difference is that, while the two LESs amplitudes are similar, the wake shape becomes smoother earlier in the case of the LES_{CF} (Fig. 5.3 and Fig. 5.4). Another interesting observation is that the wake expands more in the vertical direction for the case of the constant forces and more in the horizontal direction for the case of the variable forces.

The tangential velocities have a different trend in the three computations (Fig. 5.5). The LES_{VF} has tangential velocities that are significantly higher than the two others for as a long as $6D$. The LES_{CF} dissipates the tangential velocities after half a rotor diameter. The difference of tangential velocities between the two LESs can explain the difference of wake width horizontally and vertically. As the LES_{CF} have a reduced wake rotation, the recovery is more dominant at the top of the wake, where the large eddies have more energies. The LES_{VF} has significantly more wake rotation and the recovery of the wake is redistributed mode evenly between the horizontal direction and the vertical direction.

Figure 5.3: Axial velocity vertical profile at different positions upstream and downstream of the wind turbine. The blue lines represent the results of the LES_{VF}. The black lines represent the results of the LES_{CF}. The red lines represent the k-ε simulation The green lines represent the free stream inflow u-velocity of the k-ε simulation.

Figure 5.4: Axial velocity horizontal profile at different positions upstream and downstream of the wind turbine. The blue lines represent the results of the LES_{VF}. The black lines represent the result of the LES_{CF}. The red lines represent the k-ε simulation.

Figure 5.5: Tangential velocity horizontal profile at different positions upstream and downstream of the wind turbine. The blue lines represent the results of the LES with variable forces. The black lines represent the results of the LES with constant forces. The red lines represent the result of the k-ε.
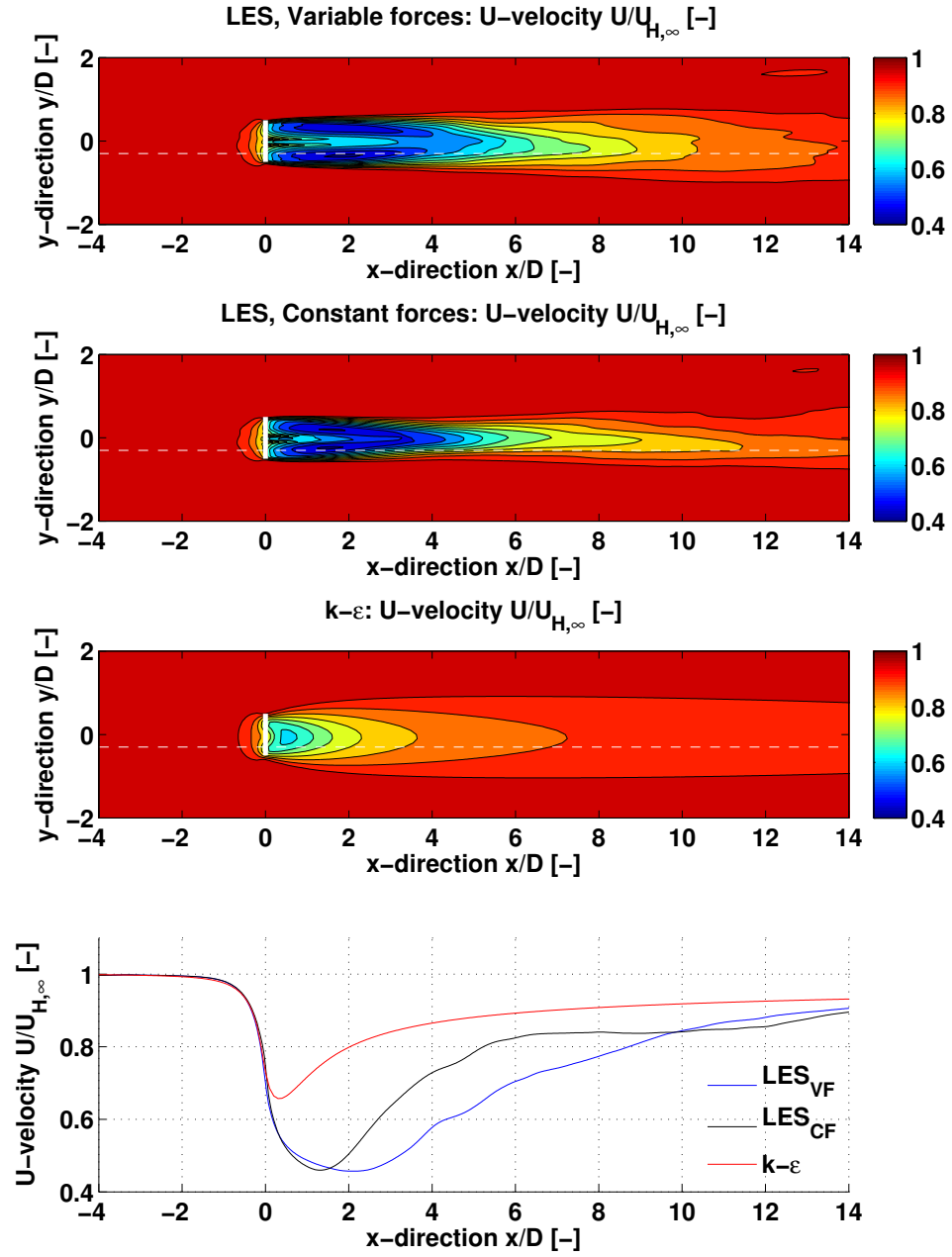
Figure 5.6: Axial velocity at hub height, normalized with the inflow value. The full white line indicates the position of the wind turbine. The dot white line indicates the position of the bottom plot (at $y = -0.25D$).

5.4.2 Turbulence Kinetic Energy

Fig. 5.7, Fig. 5.8 and Fig. 5.9 present the same types of plots for the TKE k. The k-ε indicates that the k increases upstream of the disc (Fig. 5.9). In comparison, LES_{VF}'s and LES_{CF}'s k show no indication of an increase upstream of the rotor. There is, however, a slight decrease of TKE in the close vicinity of the wind turbine in the LES_{VF}, which is not present in the LES_{CF} (Fig. 5.9).

In the two LESs, k starts to increase at the interface of the wake downstream of the rotor (Fig. 5.7 and Fig. 5.8). Further on, at about $x = 10D$, the level of k is more homogeneous in the wake region. Similarly to the axial velocity, there is a clear difference regarding the wake width of the two LESs. The LES_{VF} expands more horizontally, while the LES_{CF} expands more vertically.

While the inflow turbulence is not the same in the LESs and the k-ε simulation, the level of turbulence in the wake region is equivalent after $x = 5D$.

5.4.3 Dissipation

The dissipation ε is compared between the three simulations and presents very similar trends with respect to the TKE (Fig. 5.10). The dissipation ε starts to increase upstream the disc in the k-ε computation, yet not in the two LESs. Moreover, the LES_{VF} shows a slight decrease immediately downstream of the disc position, which is not present in the LES_{CF}. The two LESs' ε have similar trends. The LES_{VF} has a slight delay compared to the LES_{CF} as it starts to increase half a rotor diameter later. This difference is, however, not visible after $4D$.
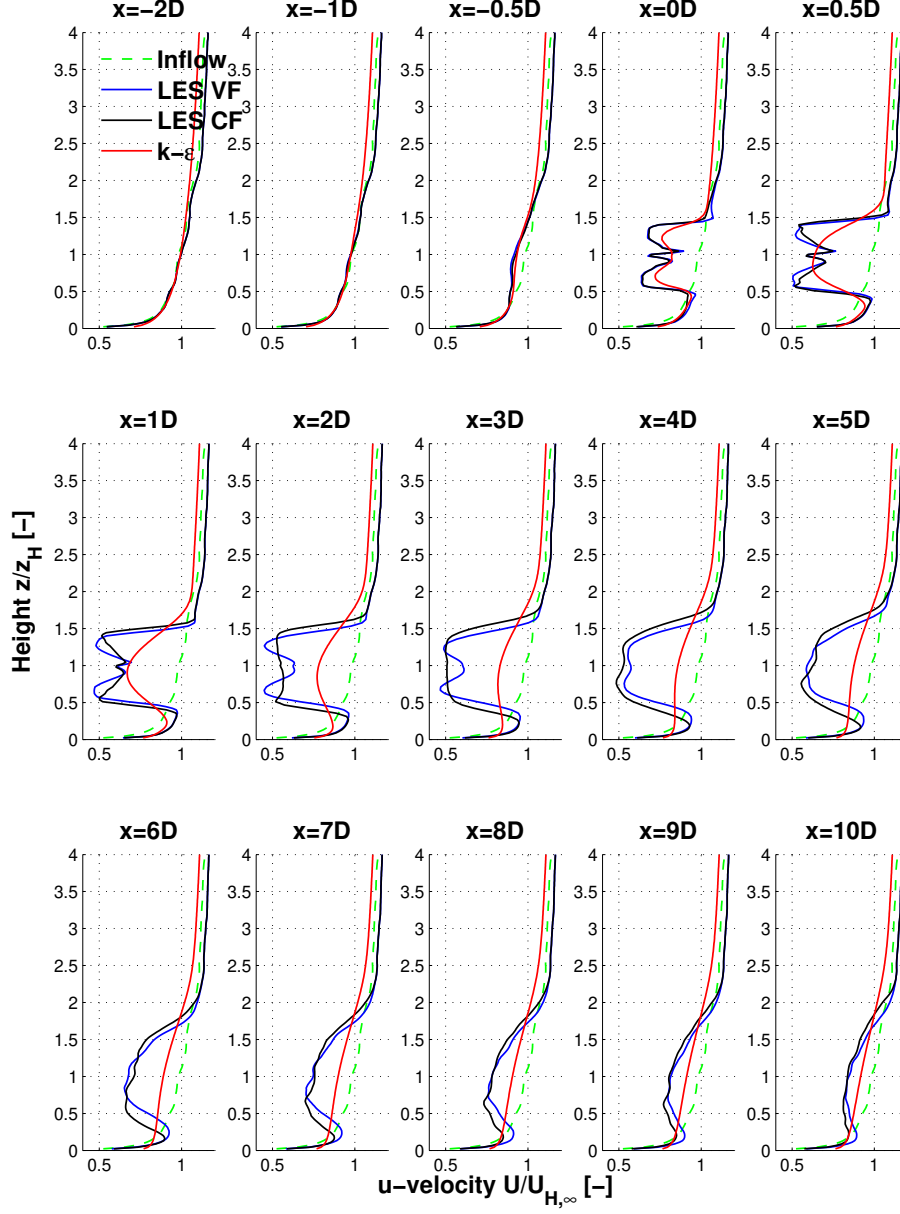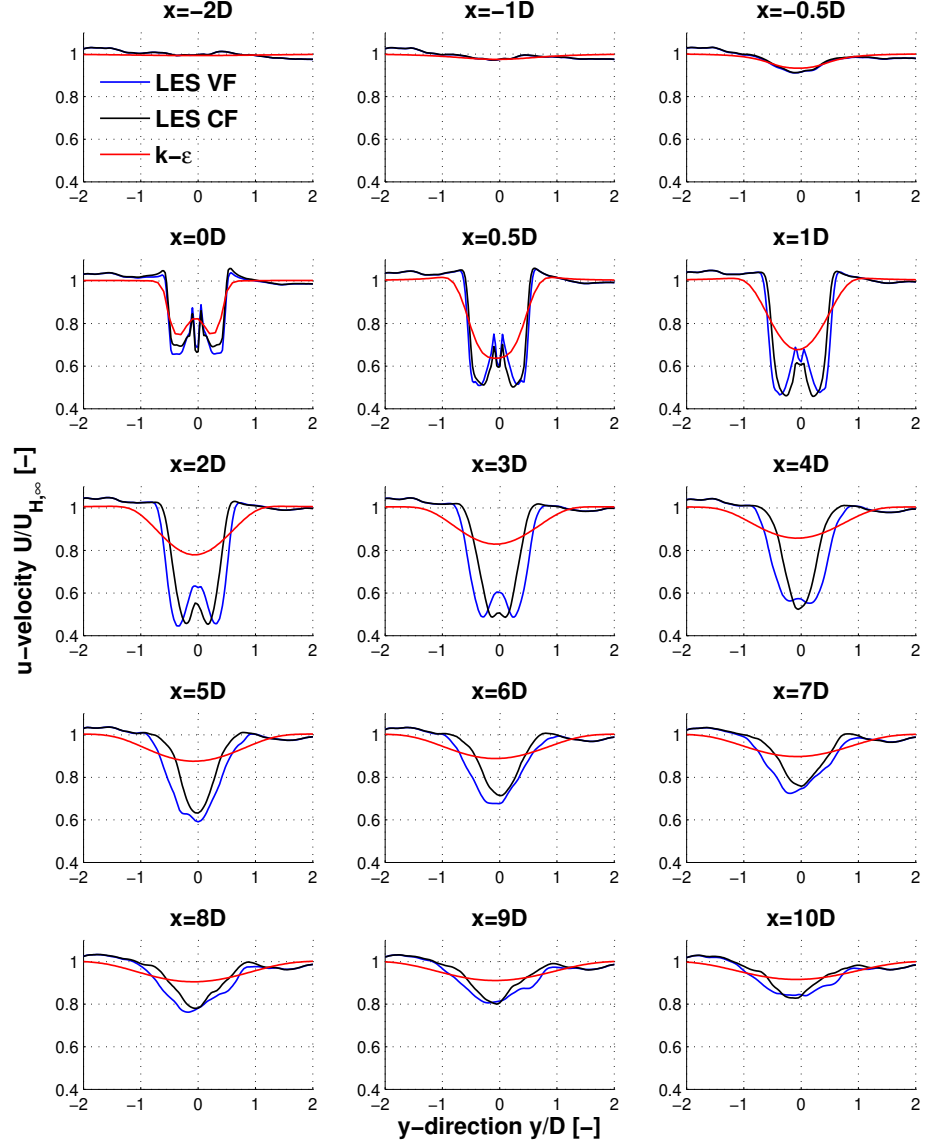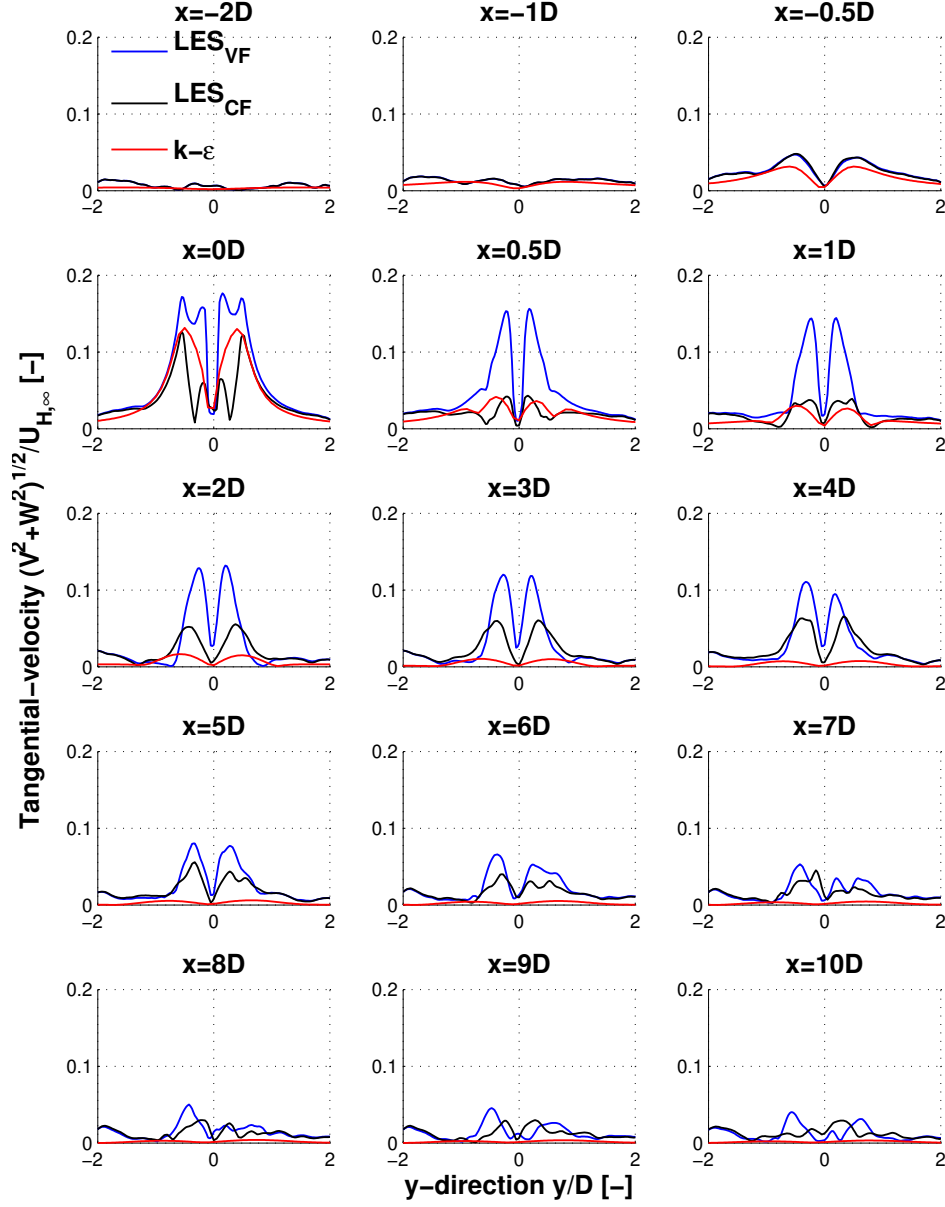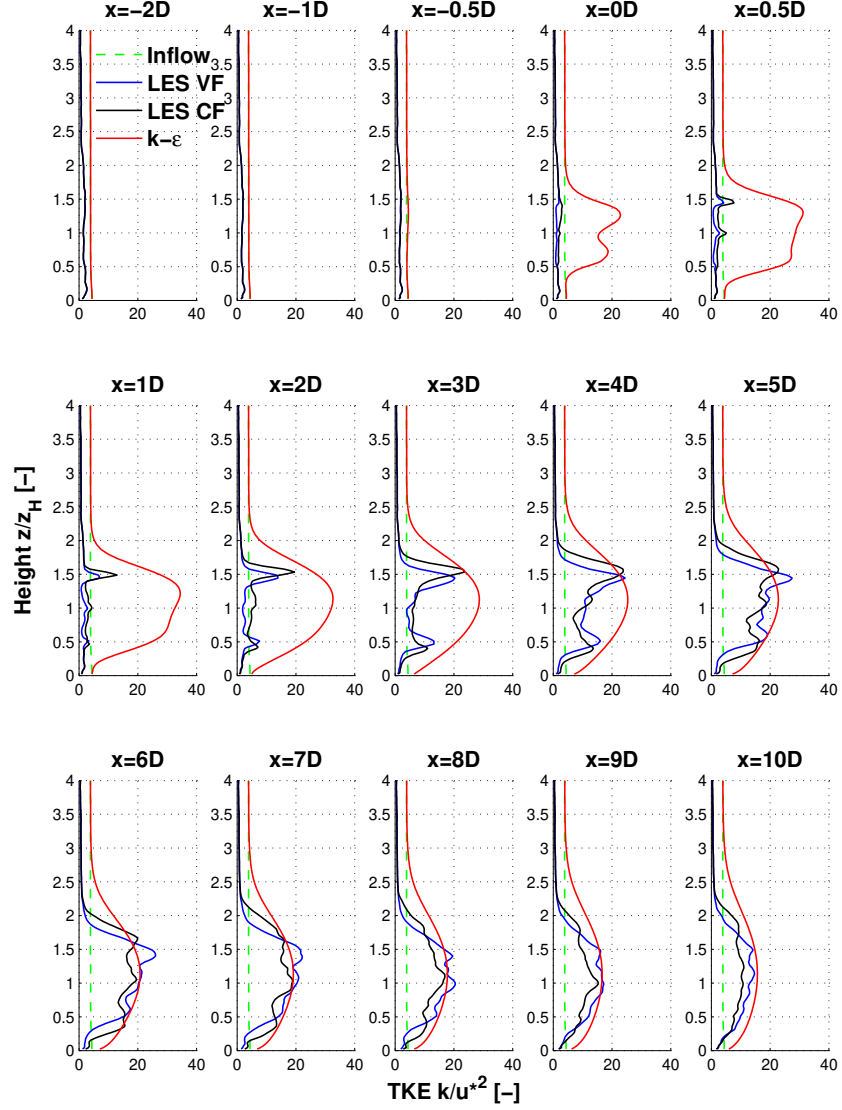
Figure 5.7: TKE vertical profile at different positions upstream and downstream of the wind turbine. The blue lines represent the results of the LES with variable forces. The black lines represent the results of LES with constant forces. The red lines represent the results of the k-ε simulation using the averaged force of the LES. The green lines represent the free stream inflow k of the k-ε simulation.
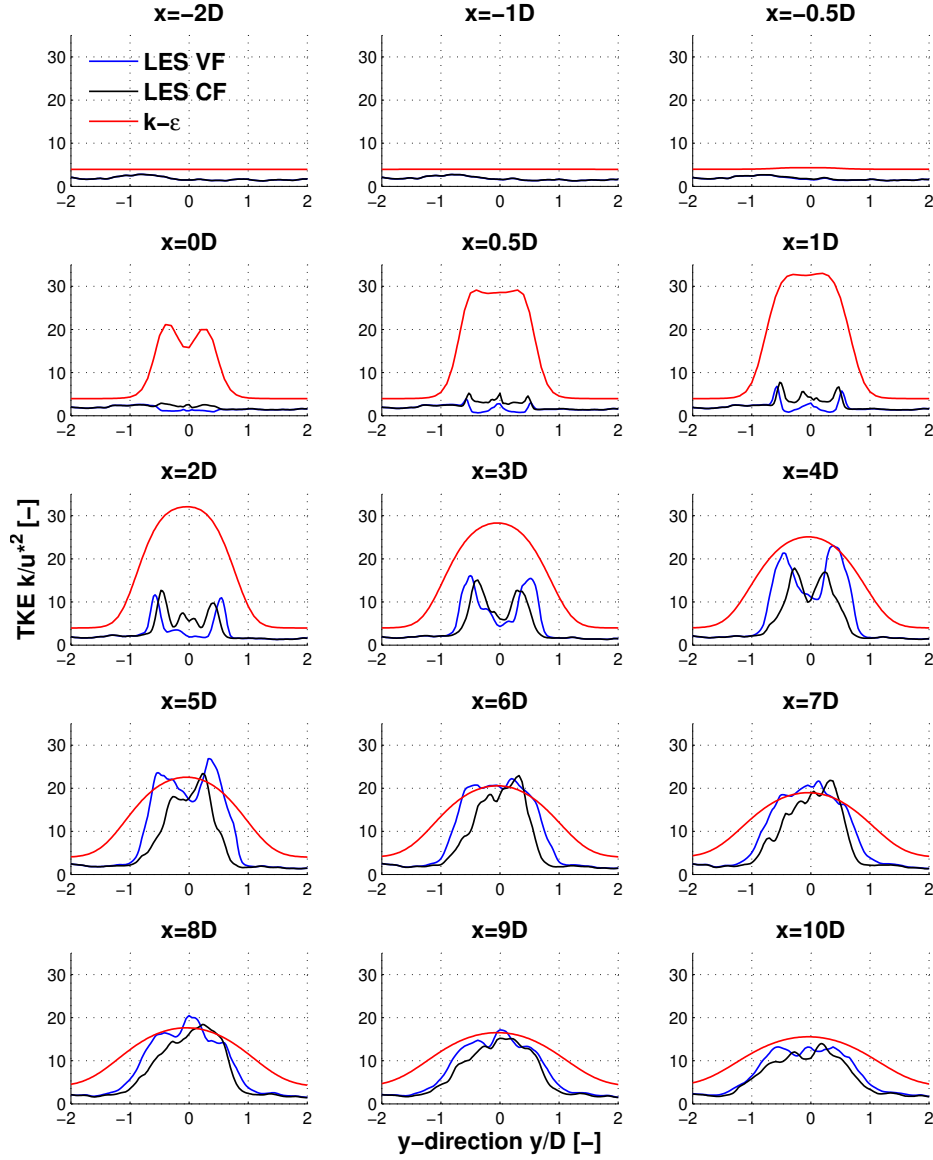
Figure 5.8: TKE horizontal profile at different positions upstream and downstream of the wind turbine. The blue lines represent the results of the LES with variable forces. The black lines represent the results of LES with constant forces. The red lines represent the results of the k-ε simulation using the averaged force of the LES. The green lines represent the free stream inflow k of the k-ε simulation.
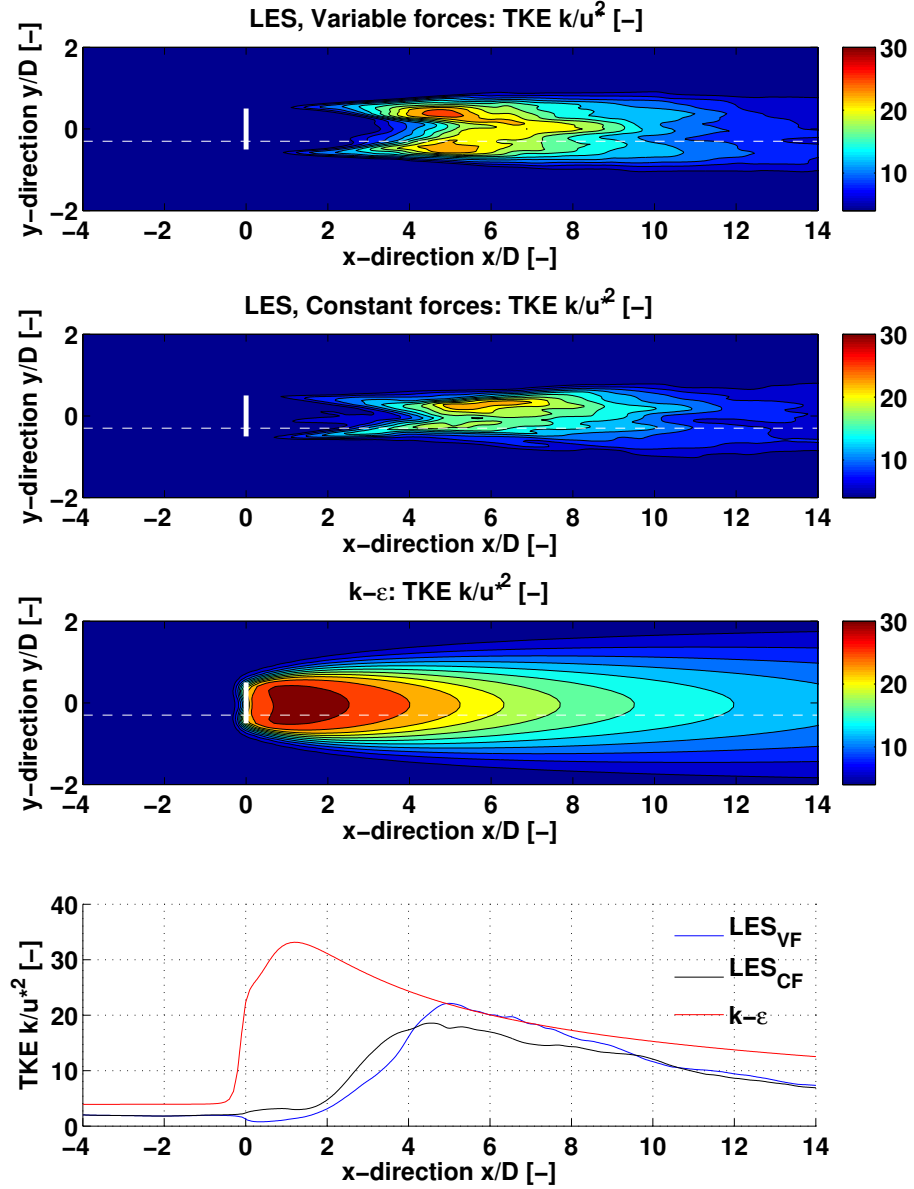
Figure 5.9: Turbulence Kinetic Energy k at hub height, normalized with the square of the friction velocity. The full white line indicates the position of the wind turbine. The dot white line indicates the position of the bottom plot (at $y = -0.25D$).
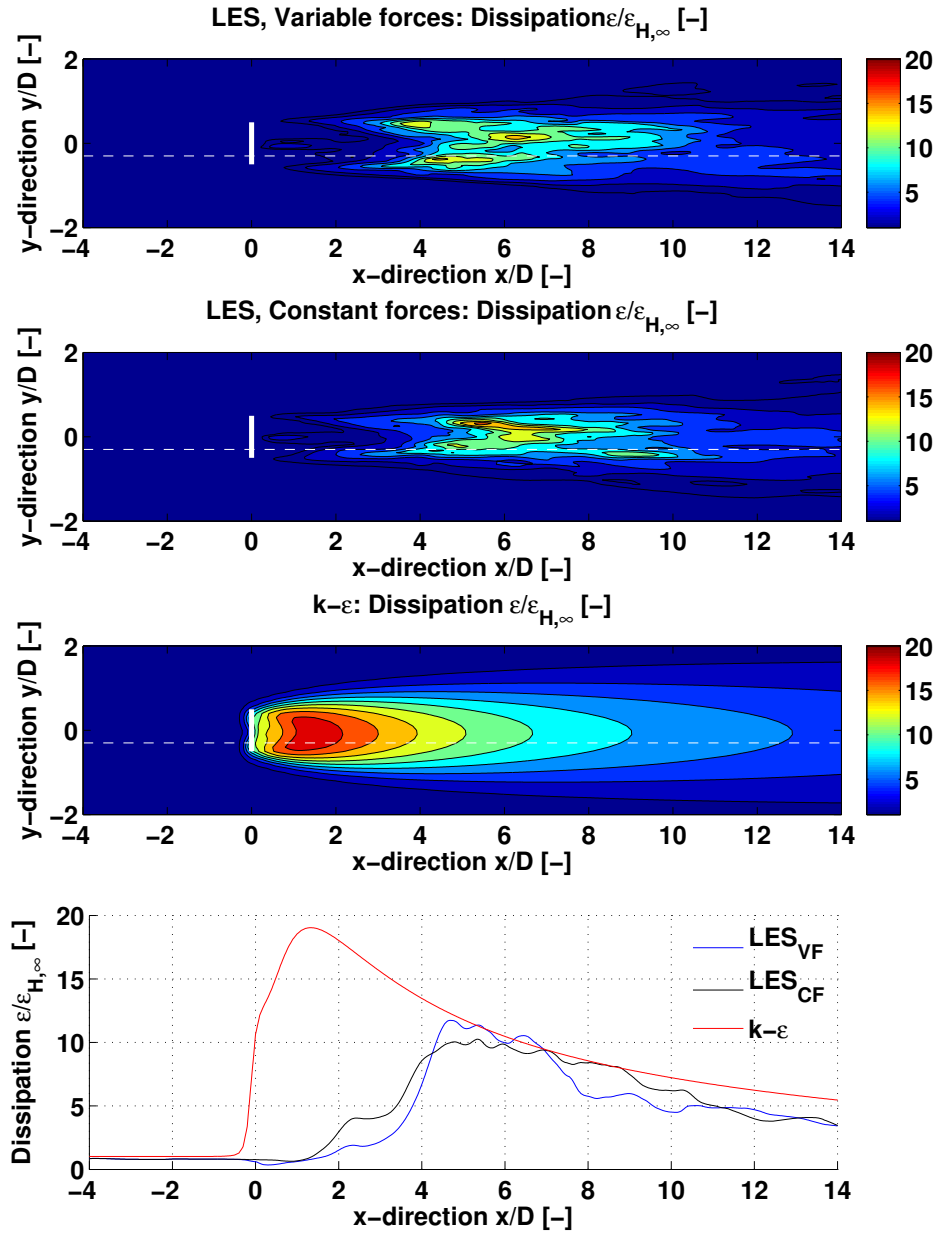
Figure 5.10: Dissipation ε at hub height, normalized with the inflow value. The full white line indicates the position of the wind turbine. The dot white line indicates the position of the bottom plot (at $y = -0.25D$).

5.4.4 Reynolds-stress

The normal axial Reynolds-stresses R_{11}^{LES} Eq. (5.7) and $\overline{u_1' u_1'}$ Eq. (5.6), for the two LESs and $R_{11}^{k\text{-}\varepsilon}$, for the k-ε Eq. (A.11), are plotted in Fig. 5.11. As for the TKE, the Reynolds-stress $R_{11}^{k\text{-}\varepsilon}$ in the k-ε increases upstream of the rotor.

The two different expressions for the resolved LES Reynolds-stresses gives similar trends far upstream of the wind turbine and in the far wake region. However, the region surrounding the wind turbine has a completely different trend.

The R_{11}^{LES} in the two LESs presents an increase upstream of the disc, in a similar trend as $R_{11}^{k\text{-}\varepsilon}$, although at a much lower scale. On the contrary, the time-average $\overline{u_1' u_1'}$ terms do not increase upstream of the disc. As for k and ε, the LES_{VF} $\overline{u_1' u_1'}$ term slightly decreases just downstream of the disc, while the LES_{CF} term starts to increase right downstream of the disc.

5.4.5 Eddy-viscosity

The two types of LES eddy-viscosities and the k-ε eddy-viscosity are plotted on Fig. 5.12. As for k, ε and R_{11}, the k-ε eddy-viscosity starts increasing upstream of the disc and reaches its maximum value at about one rotor diameter downstream of the wind turbine.

The two LESs eddy-viscosities are slightly more difficult to interpret, as there is a large amount of noise. Nonetheless, some distinctive trends can be seen in the region close to the rotor disc.

The ν_t^{LES1} Eq. (5.1) stays constant in the two LESs up to the disc position. Directly downstream of the disc, the LES_{CF} starts increasing, while the LES_{VF} term decreases to a level lower than the inflow value. After about $1.5D$ downstream of the disc, the two ν_t^{LES1}s have a similar trend. They both increase steeply to a level similar to the k-ε value and start decreasing steadily after $3D$.

The ν_t^{LES2} Eq. (5.2), based on the Reynolds-stresses and strain rate ratio, starts to decrease about $1D$ upstream of the disc, to reach a level close to zero. At the disc location, the LES_{CF} starts increasing in a similar way as for the LES_{CF}'s ν_t^{LES1}, while the LES_{VF} term stays relatively small. The two LESs' ν_t^{LES2}s meet again at $1.5D$ downstream of the disc and follow a similar trend afterwards, i.e. a slow increase up to $10D$, followed by a slow decrease.

Note that the LES_{VF}'s term shows a peak at $10D$, which is not visible on other lines extraction. This peak is expected to be caused by the low averaging time discussed previously.
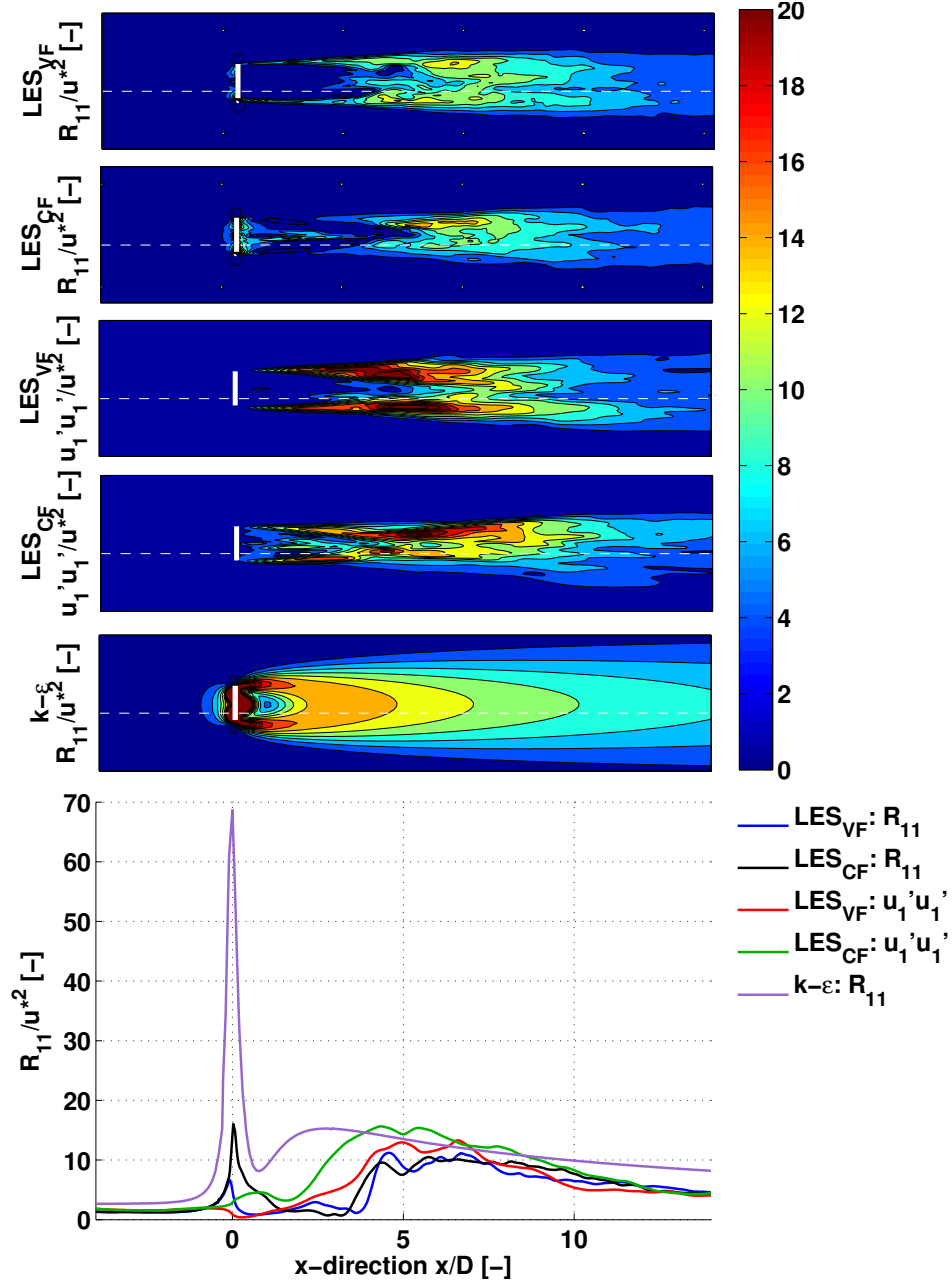
Figure 5.11: Normal axial Reynolds-stresses of LES Eq. (5.6), Eq. (5.7) and k-ε (A.11). The full white line indicates the position of the wind turbine. The dot white line indicates the position of the bottom plot (at $y = -0.25D$).
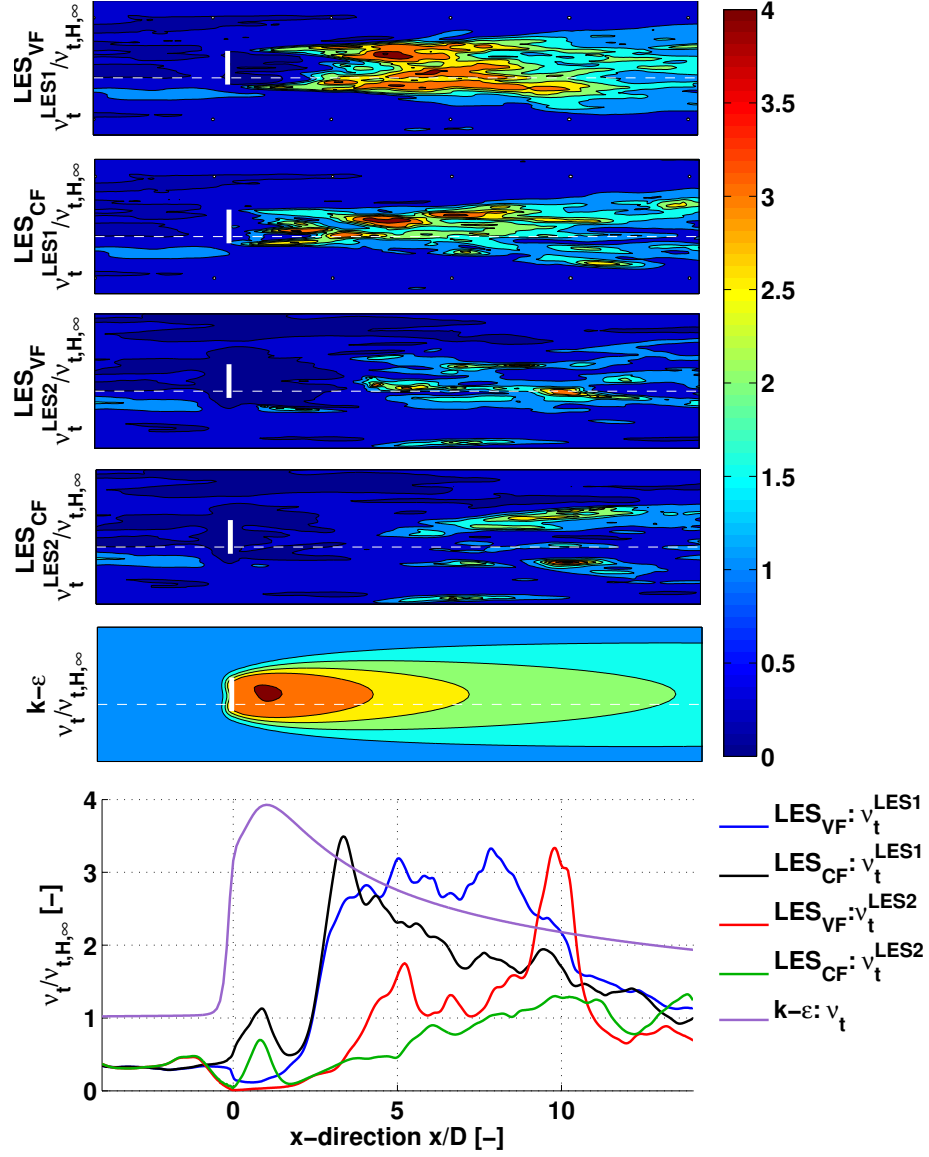
**Figure 5.12:** Eddy-viscosity normalized with the neutral stratified atmospheric value in a plane at hub height. The LES eddy-viscosity is calculated in two ways: ν_t^{LES1} using the k-ε definition Eq. (5.1), and using the ratio between the time averaged Reynolds-stresses and the mean strain rate tensor Eq. (5.2). The full white line indicates the position of the wind turbine. The last graph is a line extraction at $y = -0.25D$. Its path is shown in the contour plots as a white dotted line.
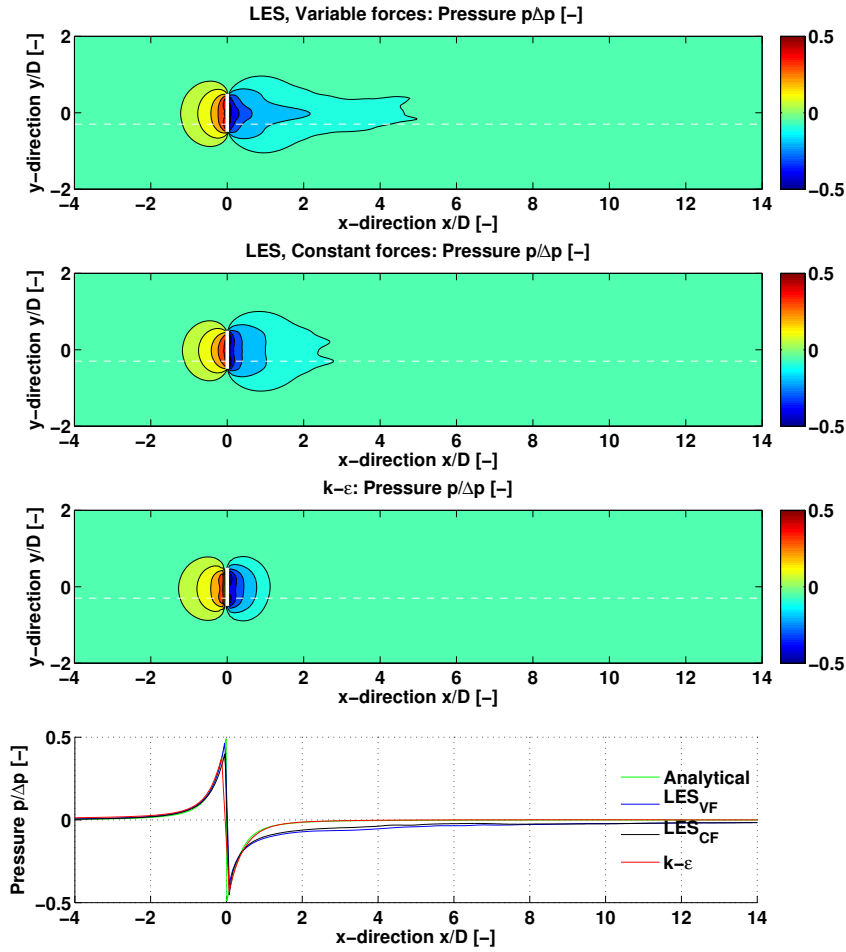
Figure 5.13: Pressure at hub height for the two LESs and the k-ε. The full white line indicates the position of the wind turbine. The dot white line indicates the position of the bottom plot (at $y = -0.25D$). The analytical solution is found from Eq. (2.46).

5.5 Discussion

5.5.1 First observations

The large discrepancy between k-ε and LES at the vicinity of the wind turbine shows that the way the large eddies are modelled in the k-ε model is not appropriate in this region.
The velocity at the disc is significantly higher for k-ε (Fig. 5.6), which confirms the results of the previous chapter. As the LES model operates with an eddy-viscosity much lower than the RANS model, the disc velocities are closer to the theoretical values.

The tangential velocities are dissipated much faster in the k-ε than in the two other LESs (Fig. 5.5). The wake rotation is known to yield a larger pressure in the wake region, compared to the atmospheric pressure (Sharpe [82], Madsen [56]) and could explain why the k-ε pressure is recovering faster in the wake compared to the two LESs (Fig. 5.13).

The normal Reynolds-stress comparison, Fig. 5.11, shows that the $R_{11}^{k\text{-}\varepsilon}$ starts increasing upstream of the actuator disc. While the increase of the R_{11}^{LES} is not of the same scale, it also starts to increase upstream of the disc. These two Reynolds-stresses are based on k, ε and S_{ij} through Eq. (5.7). While the eddy-viscosity, which is linked to the ratio k^2/ε, acts differently in k-ε and LES (Fig. 5.12), the velocity gradient is very similar upstream of the wind turbine (Fig. 5.6). This can explain the similar trend and the difference of amplitude between the normal Reynolds-stress R_{11}^{LES} and $R_{11}^{k\text{-}\varepsilon}$ (Fig. 5.11).
However, it is interesting to note that this peak is not present in the normal resolved LES Reynolds-stress $\overline{u_1' u_1'}$ Eq. (5.6) (Fig. 5.11). While there is a steep increase of the axial velocity gradient, the LES_{VF} normal Reynolds-stress decreases shortly upstream of the wind turbine.

The similar trend between R_{11}^{LES} and $R_{11}^{k\text{-}\varepsilon}$, in contrast with the trend of the LESs $\overline{u_1' u_1'}$ indicates that the eddy-viscosity concept Eq. (5.7)) is invalidated in the region surrounding the actuator disc (Fig. 5.11). Even if the k-ε simulation had the same k and ε as the LES, the Reynolds-stresses based on Eq. (5.7) could not be the same as the time averaged resolved LES Reynolds-stresses $\overline{u_i' u_j'}$.

The comparison between the two LESs also gives an interesting insight. While they both have the same time averaged force, the mean velocity and turbulence parameters present some visible differences. In the close wake region, k starts increasing in the LES_{CF}, while it decreases in the LES_{VF} (Fig. 5.9). As a consequence, the LES_{CF}'s axial velocity vertical and hori-

zontal profile are smoothed more rapidly (Fig. 5.3 and Fig. 5.4). Moreover, the LES_{VF} tangential velocities are significantly larger than the LES_{CF} in the first $7D$ downstream of the disc. This indicates that the wake rotation decays into turbulence faster in the case of LES_{CF} and could partially explain the increase of k. However, there is no clear indication of why k decreases in the LES_{VF}.

In the following sections, the different assumptions made to derive the two turbulence models are studied in order to get an in-depth understanding of why the two models differ so widely.

5.5.2   Assumption map

EllipSys, the flow solver used in the present work, is based on a series of assumptions that simplify the physics of the problem in order to make it solvable and to decrease the computational cost. The initial postulates are the Navier-Stokes Equations (A.2), which are based on the concept of mass and momentum conservation. From this point, the different assumptions and their applicability to the wind turbine flows, are analyzed.
An illustration of the different layers of assumptions of the most wildly used turbulence models is presented in Fig. 5.14. The arrows indicate the path followed by the different turbulence models to obtain their final equations. The following analysis is focussed on the k-ε model and consequently follows its assumption path. The LES model is taking care of the turbulence in two different ways accordingly to its length-scale ℓ. The large-scale turbulence is modelled directly in a similar fashion as a Direct Navier-Stokes (DNS) simulation. The small-scale turbulence is taken care of, here, by the SGS model, which is based on the same assumption as a RANS model (except that the averaging is spatial instead of temporal). This is important to notice, because this means that the LES model also depends on the RANS assumptions for modelling the small-scale turbulence. If

5.5.3   RANS assumptions

Averaging assumptions

In the RANS Equations, the forces are averaged with time. However, the derivation of the time-averaged forces is not straightforward. The forces representing the action of the wind turbine on the flow are calculated in the k-ε as in the LES model, based on the local velocities. The difference is that the LES model recomputes the velocities at each time step, while the k-ε model obtains one equivalent steady state force.
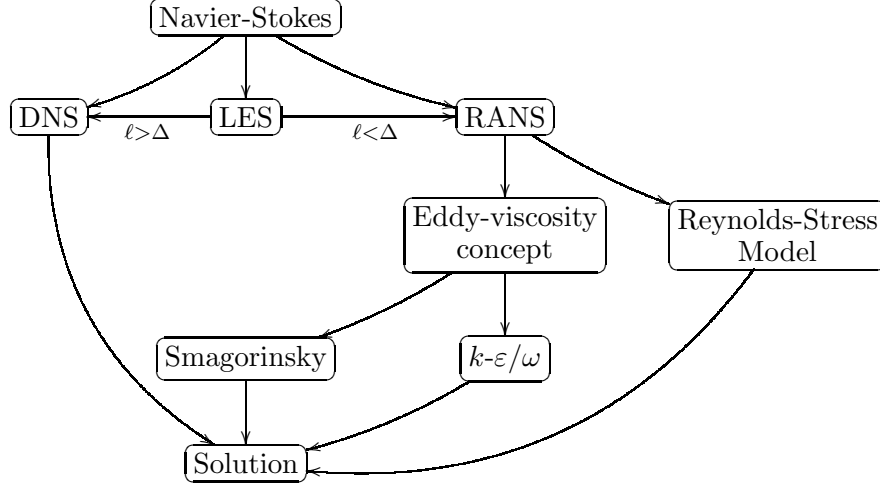
Figure 5.14: Turbulence assumption map

The forces are nonlinear functions of the local instant velocity $\mathbf{F}(\mathbf{U_D})$. Consequently, the time-averaged force is not a function of the time-averaged velocity $\overline{\mathbf{F}(\mathbf{U_D})} \neq \mathbf{F}(\overline{\mathbf{U_D}})$.

An illustration of this issue can be achieved by comparing the LES_{VF} time-averaged force $\overline{\mathbf{F}(\mathbf{U_D})}$, with the equivalent force reconstructed from the time-averaged velocities $\mathbf{F}(\overline{\mathbf{U_D}})$. The difference between the two forces $\overline{\mathbf{F}(\mathbf{U_D})}$ and $\mathbf{F}(\overline{\mathbf{U_D}})$ is found to be very small, with a relative difference of the total thrust force under $|\overline{\mathbf{T}(\mathbf{U_D})} - \mathbf{T}(\overline{\mathbf{U_D}})|/\overline{\mathbf{T}(\mathbf{U_D})} < 0.1\%$.

The force averaging assumption done in the k-ε model does not produce a large error. However, as it was observed in the previous sections, there are visible differences between the time-averaged solutions of LES_{VF} and LES_{CF} (Fig. 5.6). These differences cannot be explained by the force averaging assumption, could, therefore, be linked to the turbulence modelling assumptions.

Realizability assumptions

The concept of realizability of a Reynolds-averaged turbulence model is directly derived from the relation between the cross-correlations and auto-correlation of the velocity fluctuations (see Schumann [81]). The realizability can be checked using two relations. The Schwartz inequality imposes a positive normal stress Eq. (5.8) and the inequality relationship between the

off-diagonal terms and the diagonal terms Eq. (5.9):

$$R_{ij} > 0, \quad \text{when} \quad i = j, \tag{5.8}$$

$$|R_{\alpha\beta}|^2 \leq R_{\alpha\alpha} R_{\beta\beta}. \tag{5.9}$$

While the realizability concept does not hold any practical modelling information, it can be used to check the validity of the method used to compute the Reynold-stresses.

On Fig. 5.15, the regions where the realizability of type 1 and 2 do not hold are flagged in white. The k-ε fails to predict Reynolds-stresses that agrees with the realizability criterion in the region surrounding the wind turbine, as well as the interface of its wake.
The resolved LES Reynolds-stresses $\overline{u'_i u'_j}$ Eq. (5.6) pass the realizability test successfully. However, the resolved LES Reynolds-stresses R_{ij}^{LES} Eq. (5.7), based on the eddy-viscosity concept, fail the test in the wake region. This also indicates that the eddy-viscosity concept is not appropriate to model the Reynolds-stresses in the wind turbine wake region. The model showed here is with the LES_{CF} because it is the closest in theory to a k-ε simulation, however the LES_{VF} version gives similar results.
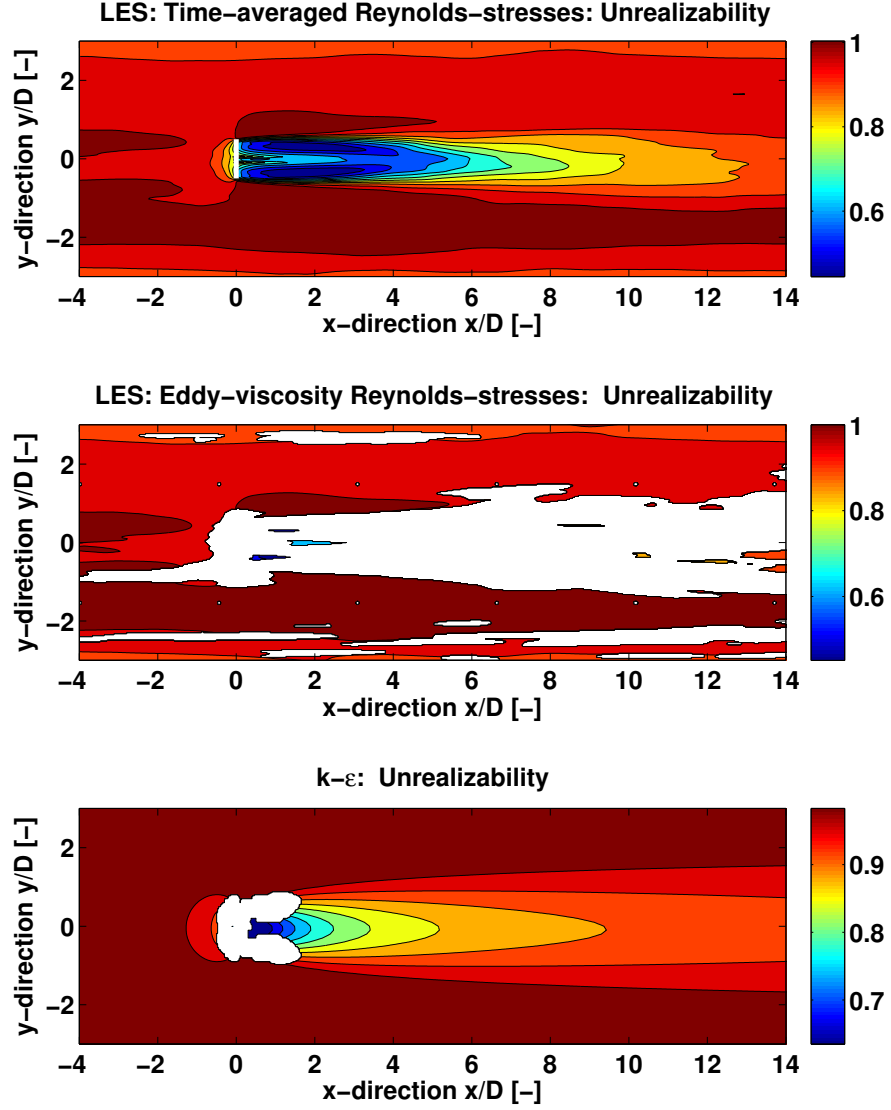
Figure 5.15: Realizability criterion at hub height for LES_{CF} and k-ε. The axial velocity is represented with the colours. The white color illustrates the regions where the Schwartz inequalities are significantly invalidated. The top plot is based the time-averaged resolved LES Reynolds-stresses $u'_i u'_j$ Eq. (5.6). The middle plot is based on the Eddy-viscosity concept LES Reynolds-stresses R_{ij}^{LES} Eq. (5.7). The bottom plot is based on the Eddy-viscosity concept k-ε Reynolds-stresses $R_{ij}^{k\text{-}\varepsilon}$ Eq. (A.11).

5.5.4   Boussinesq assumptions

The Boussinesq approximation is derived from an analogy between the molecular transport and the turbulence transport budget and was originally proposed by Boussinesq [16]. An introduction to the eddy-viscosity concept and some of its assumptions is presented in most of the turbulence textbooks (e.g. Wilcox [98], Pope [67], Tennekes and Lumley [95], Bernard and Wallace [15]). Many publications discuss more in detail the implications of the Boussinesq assumptions [54, 43, 93, 13, 14, 34, 80]. In particular, Schmitt [80] analysed the correlation between the Reynods-stress tensor and the strain rate tensor, using DNS and LES basic test cases and found that in practice the Boussinesq hypothesis is almost never verified.

The following analysis is based on an approach originally proposed by Bernard et al. [13, 14] and was also summarized in details in chapter 6 of the turbulence textbook from Bernard and Wallace [15].

Turbulent momentum transport

The particle n passing through a fixed point $\boldsymbol{x}$ is studied. Through its random path, the particle brings the flow features from different upstream locations. The velocity component in the i-direction, at $\boldsymbol{x}$, at the time $t = t^n$ is defined as

$$U_i(\boldsymbol{x}, t^n) = \overline{U_i}(\boldsymbol{x}) + u_i'(\boldsymbol{x}, t^n), \qquad (5.10)$$

where the overbar is the ensemble average value of the velocity field at the position $\boldsymbol{x}$. The path of this particle is defined by the vectorial time function $\boldsymbol{x}^n(t)$, so that $\boldsymbol{x}^n(t^n) = \boldsymbol{x}$.

Figure 5.16: Illustration of different paths followed by particles passing through the position $\boldsymbol{x}$.

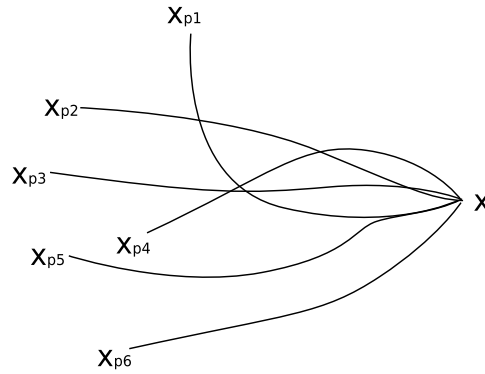For the purpose of studying the turbulent momentum transport, the flow differences between the particles at the position $\boldsymbol{x}$ and at an upstream position are analyzed. This upstream position is defined by the time $t = t_p^n < t^n$, where the particle is located at the position $\boldsymbol{x_p}^n = \boldsymbol{x}^n(t_p^n)$. Note that the time t_p^n and the position $\boldsymbol{x_p}^n$ are directly linked to the particle considered and, therefore, change when another particle is considered. The velocity of the particle n at the time t_p^n is defined as

$$U_i(\boldsymbol{x_p}^n, t_p^n) = \overline{U}_i(\boldsymbol{x_p}^n) + u_i'(\boldsymbol{x_p}^n, t_p^n). \tag{5.11}$$

Note that the term $\overline{U}_i(\boldsymbol{x_p}^n)$ corresponds to the ensemble average velocity value of the position $\boldsymbol{x_p}^n$, which, therefore, still depends on the particle considered (see Fig. 5.16).
For the sake of clarity, the terms ^{n} are dropped from now on.

From this definition, three assumptions are made:

1. For each particle, there exists a time $\tau = t - t_p$, during which the particle conserves its momentum.

$$U(\boldsymbol{x_p}, t_p) = U(\boldsymbol{x}, t). \tag{5.12}$$

2. This time τ is large enough so that the fluctuation components at the time t_p are uncorrelated with the other fluctuation components at the time t.

$$\overline{u_i'(\boldsymbol{x_p}, t_p) u_j'(\boldsymbol{x}, t)} = 0. \tag{5.13}$$

3. The velocity between $\boldsymbol{x}$ and $\boldsymbol{x_p}$ can be assumed to be linear.

$$\overline{U}_i(\boldsymbol{x_p}) = \overline{U}_i(\boldsymbol{x}) - L_{p,j} \frac{\partial \overline{U}_i}{\partial x_j}(\boldsymbol{x}), \tag{5.14}$$

with

$$L_{p,j} = \int_{t_p}^{t} U_j(\boldsymbol{x}(s), s) \, \mathrm{d}s = x_j - x_{p,j}. \tag{5.15}$$

In order to define the eddy-viscosity concept, the expression of the fluctuation component is first expressed as

$$u_i'(\boldsymbol{x}, t) = U_i(\boldsymbol{x}, t) - \overline{U}_i(\boldsymbol{x}). \tag{5.16}$$

Then the expression of the original position of the particle is added,

$$u_i'(\boldsymbol{x}, t) = u_i'(\boldsymbol{x_p}, t_p) + \left[\overline{U}_i(\boldsymbol{x_p}) - \overline{U}_i(\boldsymbol{x}) \right] + \left[U_i(\boldsymbol{x}, t) - U_i(\boldsymbol{x_p}, t_p) \right]. \tag{5.17}$$

The first assumption Eq. (5.12) cancels the last RHS term and the third assumption Eq. (5.14) rewrite the second RHS term as a velocity gradient term. Eq. (5.17) can then be rewritten as,

$$u_i'(\boldsymbol{x}, t) = u_i'(\boldsymbol{x_p}, t_p) - L_{p,k} \frac{\partial \overline{U_i}}{\partial x_k}(\boldsymbol{x}). \tag{5.18}$$

The Reynolds stress Eq. (5.19) are then found by multiplication of Eq. (5.18) with another local fluctuation component and a time average

$$\overline{u_i'(\boldsymbol{x}, t) u_j'(\boldsymbol{x}, t)} = \overline{u_j'(\boldsymbol{x}, t) u_i'(\boldsymbol{x_p}, t_p)} - \overline{u_j'(\boldsymbol{x}, t) L_{p,k}} \frac{\partial \overline{U_i}}{\partial x_k}(\boldsymbol{x}). \tag{5.19}$$

From Eq. (5.19), the second assumption Eq. (5.13) cancels the first term of the RHS. The local fluctuation component are assumed to be mainly correlated with the distance corresponding to their respective direction ($\overline{u_j'(t) L_{p,k}} \neq 0$ only if $j = k$),

$$\overline{u_i' u_j'} = -\nu_{t,ij} \frac{\partial \overline{U_i}}{\partial x_j}, \tag{5.20}$$

$$\nu_{t,ij} = \overline{\int_{t_p}^{t} u_j'(\boldsymbol{x}, t) u_i'(\boldsymbol{x}(s), s)\, \mathrm{d}s} = \overline{u_j'(\boldsymbol{x}, t) L_{p,j}}. \tag{5.21}$$

From Eq. (5.20), the usual expression of the Reynolds stress Eq. (5.22) is obtained by enforcing the tensor symmetry ($\overline{u_i' u_j'} = \overline{u_j' u_i'}$), as well as enforcing the trace to be equal to the turbulence kinetic energy ($k = \frac{1}{2} \overline{u_i' u_i'}$). In the process, the eddy-viscosity is assumed to be equal in all direction,

$$\overline{u_i' u_j'} = \frac{2}{3} k \delta_{ij} - \nu_t \left(\frac{\partial \overline{U_i}}{\partial x_j} + \frac{\partial \overline{U_j}}{\partial x_i} \right). \tag{5.22}$$

The Boussinesq assumptions can now be analysed in the context of wind turbine wake in atmospheric flows.

Transport by acceleration

The first assumption Eq. (5.12) is based on the idea that the particles are free of external or internal forces and conserve their velocity over their path. However, the particles rarely conserve their velocity over long distances. The particle constantly undergoes the work of pressure and viscous forces. The term neglected is, therefore, accounting for the particle acceleration and deceleration. Bernard and Handler [14] expressed this acceleration term

with respect with the pressure gradient and a dissipative term.

$$\overline{u'_j(\boldsymbol{x},t)[U_i(\boldsymbol{x},t) - U_i(\boldsymbol{x_p},t)]} \;=\; -\overline{\int_{t_p}^{t} \frac{1}{\rho} u'_j(\boldsymbol{x},t)\frac{\partial p}{\partial x_i}(\boldsymbol{x}(s),s)\,\mathrm{d}s}$$
$$+\overline{\int_{t_p}^{t} \nu u'_j(\boldsymbol{x},t)\nabla^2 U(\boldsymbol{x}(s),s)\,\mathrm{d}s} \quad (5.23)$$

A wind turbine extracts energy from the wind by applying a thrust and a torque on the wind. This thrust and torque create a jump of pressure at the rotor that generate a strong adverse pressure gradient field surrounding the wind turbine. The effect of this pressure gradient field is to gradually reduce the wind velocity over a distance upstream and downstream of the rotor that is larger than a rotor diameter. In the volume where the adverse pressure gradient field acts, the first assumption of the Boussinesq approximation is invalidated. The pressure gradient systematically reduces the momentum of any particle passing through the volume.

The local velocity fluctuations are directly influenced by the velocity brought by the particles. As the particles receive a different work from the pressure gradient according to, which path they follow, the velocities brought by the particles at the position $\boldsymbol{x}$ and, therefore, also the velocity fluctuations are directly affected by the path of the particle. Neglecting the term $\overline{u'_j[U_i - U_i^p]}$ consequently overpredicts the Reynolds-stresses.

In Fig. 5.17, the adverse pressure gradient region is indicated by the gray contour lines. Underneath is illustrated the axial velocity deficit created by the pressure gradient. The error made by the first assumption Eq. (5.12), in the region of influence of the wind turbine, increases according to the position respective to the wind turbine.

In Fig. 5.18, the LES_{VF} eddy-viscosity factor C_μ, as defined in Eq. (5.5), is plotted in the region surrounding the wind turbine. The region where the adverse pressure gradient acts has a significantly lower eddy-viscosity factor. In the first rotor diameter, C_μ follow the inverse trend of the adverse pressure gradient $\frac{\partial P}{\partial x}$. This indicates that in order to have a resolved normal Reynolds-stress based on the eddy-viscosity concept in the region of the adverse pressure gradient independently from the values of k and ε, the resolved normal Reynolds-stress $\overline{u'_1 u'_1}$ is not influenced

Transport by fluid particle displacement

The third assumption Eq. (5.14) is also invalidated by the wind turbine. The turbulence length-scale created by the surface roughness can be ap-
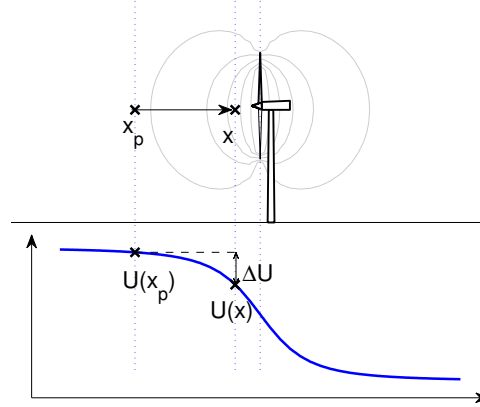
Figure 5.17: First Boussinesq assumption in the wind turbine adverse pressure gradient field. The gray isobars surrounding the wind turbine illustrate the pressure distribution. The blue line illustrates the axial velocity along the centerline passing through the wind turbine at hub height. It is assumed that there is no pressure forces acting on the flow and that the particle conserves its velocity between x_p and x ($\Delta U = 0$).

proximated as linear in the first hundred meters from the ground Eq. (A.21).

In neutrally stratificated flows the turbulent length-scale ℓ is found as Eq. (A.21),

$$\ell = \frac{\kappa z}{C_\mu^{3/4}}. \tag{5.24}$$

In the close wake region, the interface between the wake and the free stream wind flow can be very thin. However, in practice, the mesh imposes a minimum wake interface size through the cell size. In the close wake region, the interface of the wake is typically defined by three cells and has therefore a minimum size $\Delta I = 2\Delta x$. There are c cells per rotor disc in the y-direction, therefore, the initial wake interface size is

$$\Delta I = 2D/c. \tag{5.25}$$

If the wind speed is assumed to be linear in that context and the Reynolds-stresses are based on the local velocity gradients of Eq. (5.22), the initial error made at the thin interface can be up to a factor ,

$$\text{Error} = \frac{\ell}{\Delta I} \approx \frac{\kappa z c}{2 D C_\mu^{3/4}}. \tag{5.26}$$
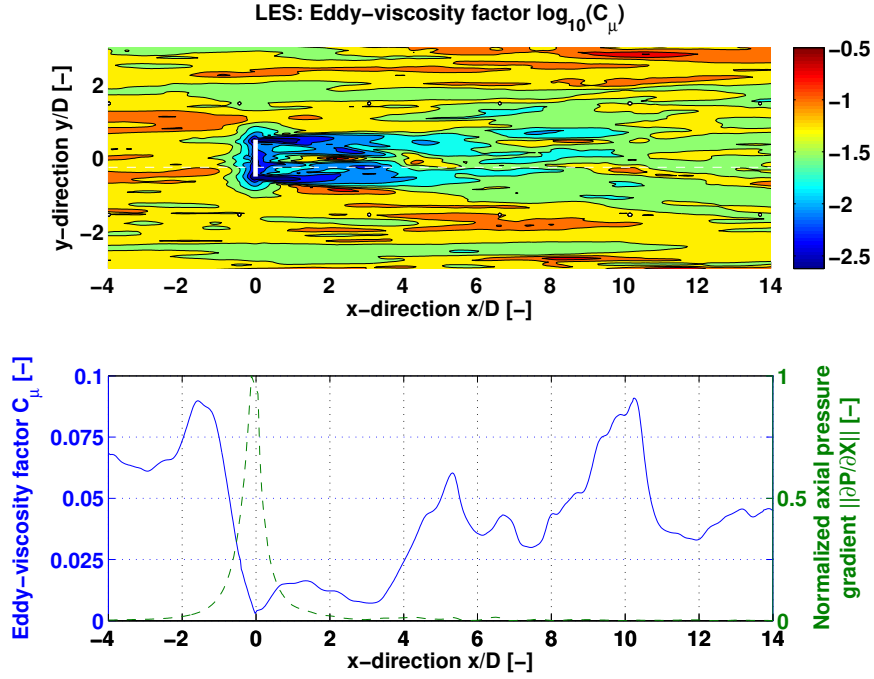
Figure 5.18: Illustration of the LES_{VF} eddy-viscosity factor C_μ^* at hub height. The factor is computed by taking the ratio between the two definitions of the eddy-viscosity Eq. (5.1) and Eq. (5.2), $C_\mu^* = \frac{||R||}{2||S||}\frac{\varepsilon}{k^2}$. The last graph is a line extraction at $y = -0.25D$. It's path is visible on the first contour plots as a white line. The axial pressure gradient is also presented to illustrate that C_μ begins to decrease at the same position where the axial pressure gradient begins to increase.

It is interesting to notice that the error increases linearly with the number of cells used to model the disc. Eq. (5.26) indicates that, in the current k-ε computation, the Reynolds-stresses are initially estimated 45 times larger than they should at the tip of the blades.

On Fig. 5.19, the assumption of linearity is checked on the LES_{VF}, at the wake interface at two positions downstream of the wind turbine. Note that the length-scale ℓ is reduced in the figures in order to illustrate the problem.

The idea of using the local velocity gradient scaled over a length-scale in order to estimate the equivalent difference of velocity brought by the particle is fine when the length-scale is linked to the size of the velocity shear. This would typically be the case of free stream turbulence. However, if the inflow turbulence length-scale is several times larger than the velocity shear size,

the scaled velocity gradient can greatly overshoot the difference of velocities intended to be computed ($L\partial U/\partial x \gg U(\boldsymbol{x_p}) - U(\boldsymbol{x})$).

To sum up, the model breaks down when changes in the mean velocity field occur over distances smaller than the turbulence length-scale. A wind turbine wake in atmospheric boundary layer turbulence is an good example of this issue.

(a) Linearity assumption at $x = 1D$

(b) Linearity assumption at $x = 7D$
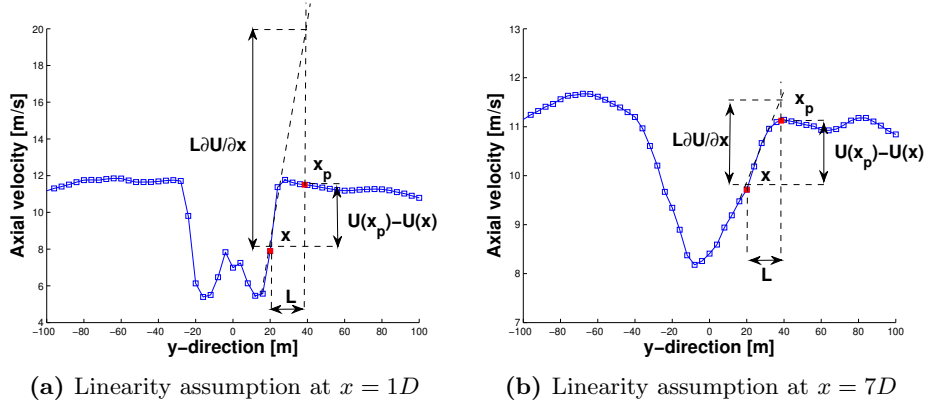
Figure 5.19: The linearity assumption in the y-direction is illustrated at two positions downstream of the wind turbine. The shear Reynolds-stress $\overline{u'v'}$ is related with the difference between the local velocity $U(x)$ and the velocity at a distance $L = \ell$. The Boussinesq approximation assumes the local linearity over the length-scale, so that $U(x+L) - U(x) = L\partial U/\partial x$. Note that, for the sake of the illustration, the length L is smaller that the turbulence length-scale found in the computation.

To check this issue, Wilcox suggests to look at the Knudsen number. The Knudsen number, as defined in Eq. (5.27), checks the assumption of linearity in a direction over a given length based on the ratio of the second-order derivative and the first-order derivative,

$$\mathrm{Kn}_{i,j} = \ell \frac{|\partial^2 U_i/\partial x_j^2|}{|\partial U_i/\partial x_j|}. \tag{5.27}$$

This number compares the second-order term in the Taylor series expansion, to the first-order term. The assumption of linearity assumes that the second-order term is negligible compared to the first-order term. This is consequently only valid when the Knudsen number is small compared to 1 ($\mathrm{Kn}_{i,j} \ll 1$).

For a logarithmic wind speed profile, the length-scale is usually assumed to be linear over height (A.21, p.140). In that case, the Knudsen number is found to be equal to the von Kármán constant ($\mathrm{Kn}_{i,j} = \kappa$), which is smaller than 1, nonetheless of the same order. Therefore neutral cases of boundary layer flows are already located at the border of the assumption of linearity

over the length-scale.

In practice, the Knudsen number is difficult to analyze on the LESs as it gives a very noisy picture. Much more illustrative results are obtained by checking the position where the second-order Taylor terms are larger than the first-order Taylor terms

$$\frac{1}{2}\ell \left| \frac{\partial^2 U_i}{\partial x_j^2} \right| > \left| \frac{U_i}{x_j} \right|. \tag{5.28}$$

Fig. 5.20 shows the nonlinearity check in the flow surrounding a wind turbine, for a standard k-ε and the LES_{VF}. The region where the second-order term is larger than the first-order term is flagged in white over the mean axial velocity contour. The whole wake region invalidates the linearity assumption in both types of computations.
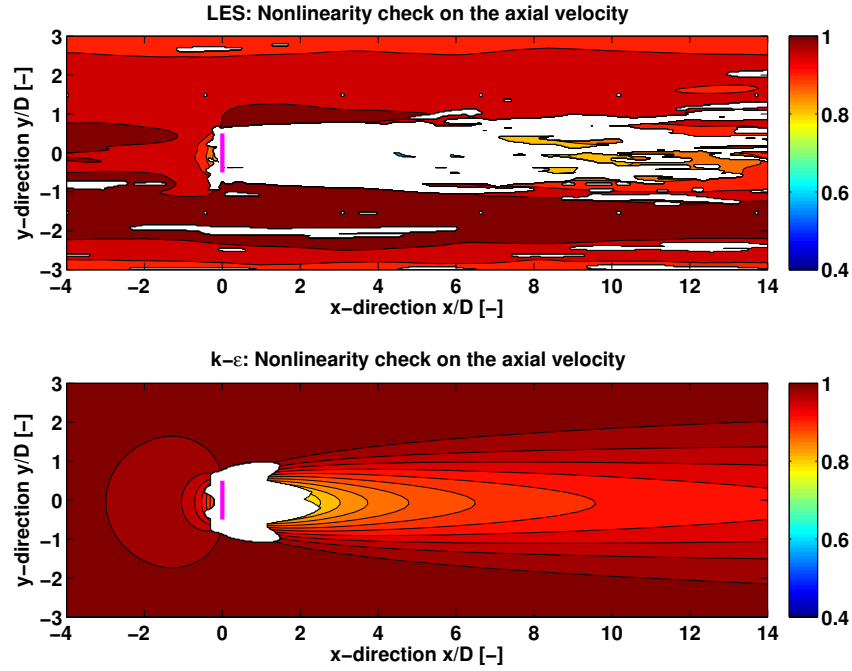

Figure 5.20: Non-linearity check on the LES_{CF} and the k-ε. The region where the second-order Taylor terms are larger than the first order terms are spotted in white. The pink line indicates the position of the turbine.

5.5.5 k-ε assumptions

Theoretical observations

The turbulence that is relevant to the rotor and the blades is not of the same order of magnitude than the fluctuations of wind considered as turbulence by the atmospheric boundary layer. Consequently only a part of the turbulence spectrum is really perceived as turbulence by the wind turbine, the low frequency turbulence is perceived as rapid changes of inflow, to which the wind turbine forces have time to adapt. As the body forces only act at the momentum level, the consequence is that the large-scale part of the turbulence is not modelled correctly in the k-ε model. Somehow, the influence of the rotor thrust should also act on the turbulence, not only through the wind speed shear generated by the forces, yet also directly as a sink of k.

The literature review on wind turbine wake measurement from Vermeer et al. [97] confirms the fact that the close central wake region of a wind turbine sees an significant decrease of the axial normal stress. This was for example observed in the Nibe wake measurement campaigns (Taylor [94] Fig. 5.1-a). Taylor notes that "the suppression of low frequency turbulence is very marked towards the centre of the wake and occurs at frequencies below abou 5×10^2 Hz. Spectral amplitudes are reduced to typically 40–50% of the corresponding upstream values. The data on the wake centreline at 25 m height indicate that the low frequency turbulence has started to recover towards the ambient level by 2.5D".
Moreover, Højstrup and Courtney [44] also noticed that in the close wake region, the turbulence length-scale is reduced in comparison to the inflow turbulence.

Fig. 5.9 shows that in the case of LES_{VF}, there is a decrease of the k and the ε. This is, however, not the case of the LES_{CF}. The LES_{CF} applies constant forces that are not able to extract energy from the turbulence. On the contrary, LES_{VF} has the time to adapt to the local changes of velocities and can, therefore, extract energy from the fluctuations.

Turbulent Equations

In the Momentum Equation, the discrete body forces action is smoothed over a larger volume by the action of the pressure gradient. This action is brought into the k and ε-equations directly through the force-velocity terms $\overline{F_k}$ and $\overline{F_\varepsilon}$ Eq. (5.29) and indirectly through the pressure-strain terms $\overline{\Pi_k}$ and $\overline{\Pi_\varepsilon}$ Eq. (5.30). These terms are derived in the same fashion as the k

and ε-equations,

$$\overline{F_k} = \overline{u'_i F_i} \quad \text{and} \quad \overline{F_\varepsilon} = 2\nu \overline{\frac{\partial F_i}{\partial x_j} \frac{\partial u'_i}{\partial x_j}}, \tag{5.29}$$

$$\overline{\Pi_k} = -\overline{u'_i \frac{\partial P}{\partial x_i}} \quad \text{and} \quad \overline{\Pi_\varepsilon} = -2\nu \overline{\frac{\partial^2 P}{\partial x_i \partial x_j} \frac{\partial u'_i}{\partial x_j}}. \tag{5.30}$$

The k-equation is found by taking the dot product of the Navier-Stokes Eq. (A.2) and the velocity filed U_i and removing the terms only composed of mean variables (Bernard & Wallace [15] Eq. 2.40). The extra term kept is here the dot product of the force with the fluctuating velocity vector average $\overline{F_k}$ Eq. (5.29). The standard form of the k-equation is rearranged as,

$$\frac{\partial k}{\partial t} + \overline{U}_j \frac{\partial k}{\partial x_j} = -\frac{\partial \overline{U}_i}{\partial x_j} R_{ij} - \varepsilon + \overline{F_k} + \overline{\Pi_k} + \nu \nabla^2 k - \frac{1}{2} \frac{\partial \overline{u'_j u'_i u'_i}}{\partial x_j}. \tag{5.31}$$

In the final k-equation in the standard k-ε model, the two terms $\overline{F_k}$ and $\overline{\Pi_k}$ are assumed to be negligible and are dropped of the equation (Wilcox [98], Bernard & Wallace [15]).

Similarly, the ε-equation is derivable from the Navier-Stokes Equations by differentiating by $\partial/\partial x_j$ and then by multiplying by $2\nu \partial u'_i/\partial x_j$ (Bernard & Wallace [15] p.28). The force term is estimated as $\overline{F_\varepsilon}$ Eq. (5.29). The different terms of the Dissipation Equation undergo afterwards some heavy surgical operations to be reduced to the standard k-ε model Eq. (A.17). During this operation the two terms $\overline{F_\varepsilon}$ and $\overline{\Pi_\varepsilon}$ are also assumed to be negligible.

The question is, therefore, are the four terms $\overline{F_k}$, $\overline{F_\varepsilon}$, $\overline{\Pi_k}$ and $\overline{\Pi_\varepsilon}$ really negligible in the vicinity of a wind turbine wake? To address this question the two LESs are compared.
The simulation show that, similarly to the momentum level, where $\partial P/\partial x$ have a smoothing property to the discrete forces, Π_k is smoothing out F_k in the k-equation and Π_ε is smoothing out F_ε in the ε-equation. For this reason the study is focussed on the sum of the terms $\Pi_k + F_k$ and $\Pi_\varepsilon + F_\varepsilon$. In order to have an idea of what is the influence of the terms in the two equations, the terms are normalized with their respective equivalent. $\Pi_k + F_k$ is a sink of turbulence and should, therefore, be compared with ε. $\Pi_\varepsilon + F_\varepsilon$ is a compared to the ratio of ε^2/k, which accounts for the "stretching of dissipation" (Bernard & Wallace [15]).

The Fig. 5.21 and 5.22 present a contour plot of the terms scaled with representative terms. The two terms are consequently $(\overline{F_k} + \overline{\Pi_k})/\varepsilon$, $(\overline{F_\varepsilon} + \overline{\Pi_\varepsilon})k/\varepsilon^2$. If the terms are smaller than 1, they are negligible. In Fig. 5.21, a clear peak is found around the disc position in the LES_{VF}, which is not

present in the LES_{CF}. The k term is roughly two orders of magnitude larger than the local dissipation, which indicates that it is not negligible. This peak explains the decrease of k, which is observed in the LES_{VF} and not in the LES_{CF}.

Fig. 5.22 also presents a clear peak around the disc location in the LES_{VF}, which is not observed in the LES_{CF}. However, the order of magnitude is small compared to the ratio ε^2/k. The reduction of ε in Fig. 5.10 is also less significant than the equivalent reduction of k, which validates the previous observation.
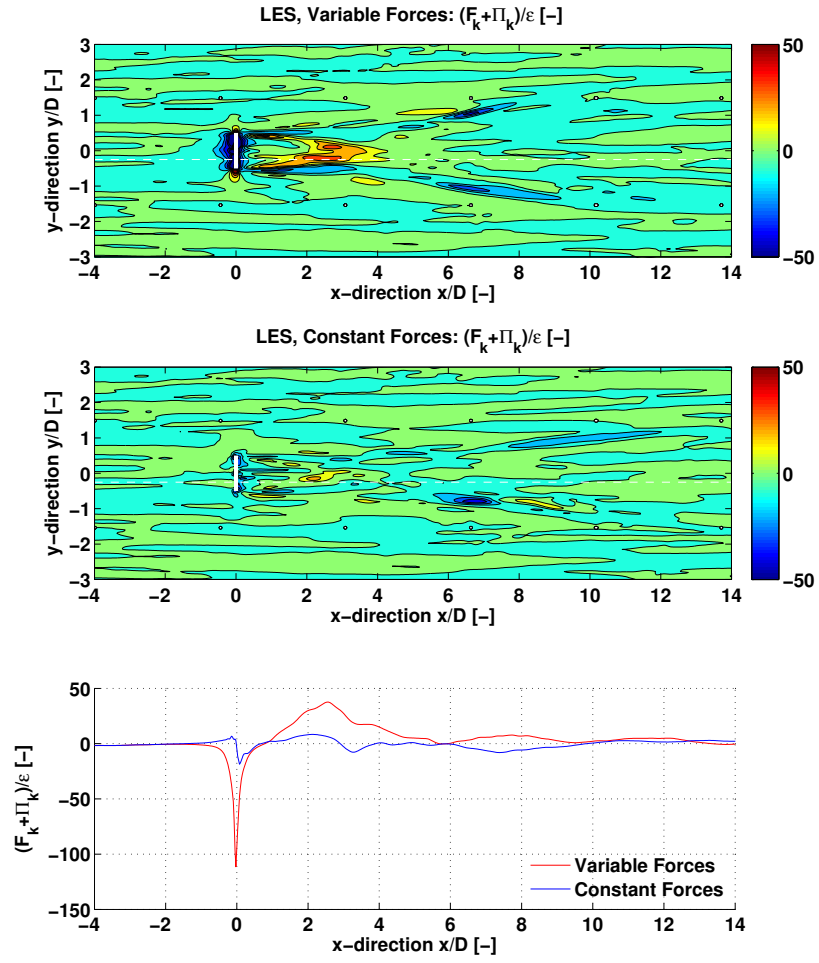
Figure 5.21: Force and pressure terms of the k-equation normalized with the local ε, in the two LESs. The white dot line indicates the path of the bottom plot.
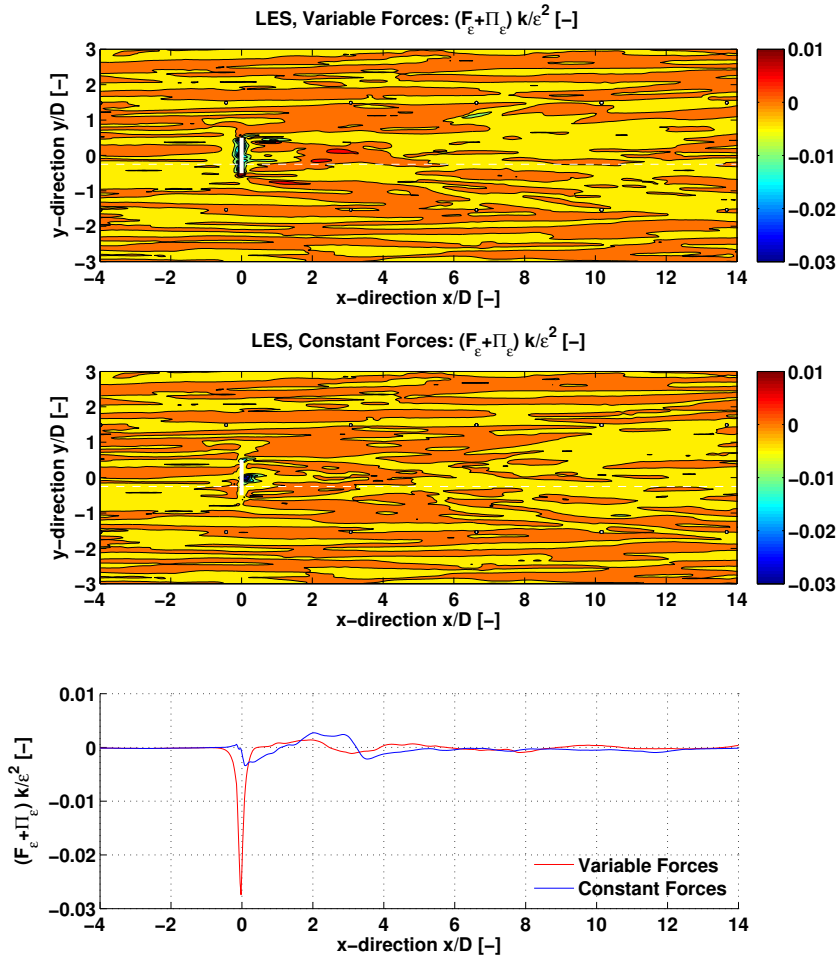
Figure 5.22: Force and pressure terms of the ε-equation normalized with the ratio ε^2/k, in the two LESs. The white dot line indicates the path of the bottom plot.

5.6   Summary

Two LESs, one with unsteady forces and one with equivalent steady forces were compared to a k-ε model. The large discrepancy between the k-ε and LES results indicates that there were issues when modelling wind turbine wake in atmospheric flows.
The two LESs gave the opportunity to analyze the different assumptions made to design the k-ε model.

The RANS assumption of force averaging was found to be valid for the case of the actuator disc. The difference between the time averaged forces and the forces estimated from the time-averaged velocity were found to be close.

The assumption of realizability in the RANS was found to be invalid in the k-ε and in the LESs, when the eddy-viscosity concept was used to derive the Reynolds-stresses. This finding indicates that the eddy-viscosity concept was invalid in the wake region.

The assumption of velocity conservation over the turbulence length-scale done in the Boussinesq approximation was found to be invalid in the region of adverse pressure gradient that surrounds the wind turbine in a spherical volume larger than $1D$.

The assumption of the velocity linearity over the turbulence length-scale yields a very large error in the estimation of the Reynolds-stresses based on the eddy-viscosity concept. This assumption was found to be invalidated in the major part of the wake region up to $10D$.

The k-ε assumption, which neglects the pressure-velocity correlation in the k- and ε-equation were found introduce a significant error. Because of this assumption, the modelled turbine was unable to extract energy from the turbulence, which yields an overestimation of the turbulence in the wake and a too rapid dissipation of the wake rotation. In particular the sink term of turbulence that was neglected in the k-equation was found to be roughly two orders of magnitude larger than the local dissipation. However, the sink term in the ε-equation was found to be negligible compared to the "dissipation stretching" term $C_{\varepsilon 2}\varepsilon^2/k$.

The methodology followed in this chapter can be applied to other types of flows, like complex terrain and canopy flow modelling. These types of flows also present some of the features of the atmospheric wind turbine flows and might also suffer from the same issues.

$$6$$

Modifications of k-ε

Contents

6.1 Introduction

In the previous chapter, the different limitations of the k-ε were analyzed in comparison to LES. From this analysis, several assumptions were found to be invalid in the context of wind turbine in atmospheric flow. This chapter focuses on presenting different methods that intent to correct those invalid assumptions.

The methodology followed is to describe the models and to compare their behaviour to the LES turbulence model, to compare the different models to the single wind turbine wake measurements from Sexbierum and Nibe and finally to discuss the different advantages and shortcomings of the models.

6.2   *k*-ε Modification Models

6.2.1   The El Kasmi-Masson Model

Description

El Kasmi and Masson [35] proposed an extended *k*-ε model based on the same idea of Chen and Kim [20]. The idea is to add a term in the turbulence kinetic energy dissipation ε-equation to enhance the creation of dissipation proportionally to the production of turbulence P_τ,

$$S_\varepsilon = C_{\varepsilon 4} \frac{P_\tau^2}{\rho k}. \tag{6.1}$$

where $C_\varepsilon 4$ is a model parameter.

This model introduces practically two free parameters to calibrate the wake turbulence model to the measurements, namely the dissipation parameter $C_{\varepsilon 4}$ and the region size over, which it is applied. El Kasmi and Masson propose to use the constant $C_{\varepsilon 4} = 0.37$ and a cylindrical region encompassing the rotor ($\pm 0.25D$).

The axial velocity development was compared to different sets of measurements by El Kasmi and Masson [35], Cabezon et al. [18], Réthoré et al. [72] and Rados et al. [68]. El Kasmi and Masson obtained results in good agreements with the Nibe turbine, the Danwin 180 kW and the MOD-0A 100 kW measurements. However Cabezon et al. [18] found that the model behaviour was unsatisfactory in comparison to the Sexbierum measurements.

Theoretical Analysis

The model is intended to be used as a mitigation of the issues disscussed in the two previous chapters. By adding this term around the wind turbine location, the production of turbulence created by the velocity shear is compensated by a proportional increase of dissipation. Chen and Kim [20] argued that this added term represents the "energy transfer rate from large-scale turbulence to small-scale turbulence controlled by the production range scale and the dissipation rate time scale.". This term, therefore, intent to account for the short-circuiting of the turbulence cascade described in Section 5.5.5. The influence of the turbine on the turbulence is here assumed to be proportional to the production of shear stresses.

By introducing a source of dissipation in the ε-equation, the model also reduces the eddy-viscosity in the region of shear stress production. This is consequently also a way to address the invalidity of the assumption of velocity linearity over the length-scale (Section 5.5.4).

Finally, in the region of adverse pressure gradient, the model is triggered

by the axial velocity gradient, which generate an unphysical increase in the normal axial Reynolds-stress, as discussed in Section 5.4.4. It is therefore also addressing the invalidity of the Boussinesq's approximation in the region of adverse pressure gradient.

The El Kasmi-Masson model consequently partically accounts for different types of modelling issues of k-ε occurring at different locations upstream and downstream of the wind turbine.

6.2.2 The Adverse Pressure Gradient Model

In Section 5.5.4, concerning Boussinesq's approximation, two main assumptions were found to be invalidated in atmospheric wind turbine flows. The first assumption, which assumes that the particles can conserve their velocity over a time-scale, is invalidated in the adverse pressure-gradient region surrounding the wind turbine. The net effect is that the axial normal Reynolds-stress R_{11} are overestimated in this region, which is the main contribution for building up the turbulence kinetic energy upstream of the wind turbine and attenuating the effect of the wind turbine on the mean velocity. In order to correct Boussinesq's assumptions in the adverse pressure gradient, the overestimated Reynolds-stresses have to be reduced.

A simple way to mitigate this issue is to reduce the eddy-viscosity in the region where the adverse pressure gradient acts. $\widetilde{\nu}_t$ is redefined as

$$\widetilde{\nu}_t = C_\mu \frac{k^2}{\varepsilon} \mathcal{F}\left(\frac{\partial P}{\partial x_i}\right), \tag{6.2}$$

where $\mathcal{F}$ is a simple function that reduces the eddy-viscosity to a minimum value in the region where the pressure gradient is higher than a threshold value,

$$\widetilde{\nu}_t = \begin{cases} C_\mu \frac{k^2}{\varepsilon} & \text{when} \quad \frac{\partial P}{\partial x_i} < c_{\text{th}} \\ \nu_{t,\text{min}} & \text{when} \quad \frac{\partial P}{\partial x_i} > c_{\text{th}}. \end{cases} \tag{6.3}$$

This method, however, creates a numerical coupling between the turbulence and the pressure gradient. This coupling is characterized by numerical pressure fluctuations in the wake of the wind turbine. In order to avoid this coupling, the region where the eddy-viscosity is decreased is set manually as a spherical region, where the radius Δr is a free parameter. This method is referred in the following section as the Adverse Pressure Gradient (APG) model.

6.2.3 The Realizability Model

The second assumption of Boussinesq's approximation that is invalidated in the wind turbine flows is the assumption of velocity linearity over the length-scale (Section 5.5.4). The regions where this assumption is invalidated are

mainly at the interfaces between the wake and the free stream.

Some of these regions are visible by checking where the Schwartz inequalities are not respected. While the Schwartz inequalities do not provide information regarding the modelling of the Reynolds-stresses, they provide a useful way to limit their relative size by comparing the shear-stresses with the normal-stresses.

The Schwartz inequalities as a turbulence model correction have been used in many studies including Schumann [81] and Shih et al. [84], who introduced the k-ε Realizable model. It was studied in the context of wind turbine by Cabezon et al. [18] and gave results closer to measurements than the standard k-ε model. The method proposed here is to use the Schwartz inequalities to reduce the eddy-viscosity following the same idea as the k-ε Realizable.

$$\widetilde{\nu}_t = \min\left(C_\mu \frac{k^2}{\varepsilon}, \nu_{t,\text{Swz}}\right). \tag{6.4}$$

The eddy-viscosity limiter $\nu_{t,\text{Swz}}$ is calculated by finding the maximum value that matches the Schwartz inequalities based on the eddy-viscosity expression of the Reynolds-stresses.

$$\left(2\nu_{t,\text{Swz}}\overline{S}_{\alpha\beta}\right)^2 = \left(\frac{2}{3}k - 2\nu_{t,\text{Swz}}\overline{S}_{\alpha\alpha}\right)\left(\frac{2}{3}k - 2\nu_{t,\text{Swz}}\overline{S}_{\beta\beta}\right), \tag{6.5}$$

where the convention followed is that there is no summation on the Greek letters.

Eq. (6.5) has two solutions:

$$\nu_{t,\text{Swz1}} = \frac{k}{6} \frac{\sqrt{\overline{S}_{\alpha\alpha}^2 + \overline{S}_{\beta\beta}^2 + 4\overline{S}_{\alpha\beta}^2 - 2\overline{S}_{\alpha\alpha}\,\overline{S}_{\beta\beta}} + \overline{S}_{\alpha\alpha} + \overline{S}_{\beta\beta}}{\overline{S}_{\alpha\alpha}\,\overline{S}_{\beta\beta} - \overline{S}_{\alpha\beta}^2}, \tag{6.6}$$

$$\nu_{t,\text{Swz2}} = \frac{k}{6} \frac{\sqrt{\overline{S}_{\alpha\alpha}^2 + \overline{S}_{\beta\beta}^2 + 4\overline{S}_{\alpha\beta}^2 - 2\overline{S}_{\alpha\alpha}\,\overline{S}_{\beta\beta}} - \overline{S}_{\alpha\alpha} - \overline{S}_{\beta\beta}}{\overline{S}_{\alpha\beta}^2 - \overline{S}_{\alpha\alpha}\,\overline{S}_{\beta\beta}}, \tag{6.7}$$

where the maximum value of the two solutions is taken. In the case where both solutions are negative, there is no solution and the normal definition for the eddy-viscosity is used,

$$\nu_{t,\text{Swz}} = \max(\nu_{t,\text{Swz1}}, \nu_{t,\text{Swz2}}). \tag{6.8}$$

To extend this method, a factor on the Schwartz eddy-viscosity can be applied:

$$\widetilde{\nu}_t = \min\left(C_\mu \frac{k^2}{\varepsilon}, C_{\text{Swz}}\nu_{t,\text{Swz}}\right), \tag{6.9}$$

which gives more control over the region where the flow is unrealizable.

It is possible to compute the minimum value the parameter C_{Swz} can take to respect the neutral boundary layer flows. Assuming that the flow is unidirectional and the axial velocity is fully developed and only a function of height Eq. (A.18), p.140, the Schwartz inequality is reduced to

$$\left(\nu_t \frac{\partial U}{\partial z}\right)^2 < C_{\mathrm{Swz}} \left(\frac{2}{3}k\right)^2.\tag{6.10}$$

By using the neutraly stratified values for ν_t Eq. (A.22), U Eq. (A.18) and k Eq. (A.19), p.140, a minimum limit is found for the parameter C_{Swz}:

$$C_{\mathrm{Swz}} > \frac{9}{4}C_\mu.\tag{6.11}$$

This model is referred in the following sections as the Realizability model. Note that the model only has a physical basis for the constant $C_{\mathrm{Swz}} = 1.0$.

6.2.4 The Wind Turbine Canopy Model

Section 5.5.3 showed that there was only a small difference between the time averaged forces and the forces based on the time averaged velocities. However, as it was showed in Section 5.5.5, the nonlinearity of the forces also affects the derivations of the k and ε-equation. This section demonstrate how to derive a theoretical estimation of the force terms in the k and ε-equation. This derivation introduces the Wind Turbine Canopy model based on a modelling of these terms.

Theoretical Analysis

The actuator disc forces are nonlinear functions of the velocity at the disc. Section 5.5.3 showed that the time-averaged forces are not directly equivalent to the forces based on the time-averaged velocities $\overline{\mathbf{F}(\mathbf{U_D})} \neq \mathbf{F}(\overline{\mathbf{U_D}})$.
To investigate this effect, the forces can be modelled as a local drag forces Eq. (6.12)

$$\mathbf{F} = -\mathbf{C_F}(\mathbf{x})(\mathbf{U} \cdot \mathbf{n})^2,\tag{6.12}$$

where $\mathbf{n}$ is the normal vector to the disc and $\mathbf{C_F}$ is a vectorial force coefficient accounting for the thrust and torque of the wind turbine that is function of the position relative to the center of the disc. The vectorial force coefficient is defined as a local actuator disc force coefficient multiplied by the corresponding cell area and the density,

$$\mathbf{C_F}(r) = \frac{1}{2}\rho A(\mathbf{x})\mathbf{C_T}(\mathbf{x}),\tag{6.13}$$

where the thrust and torque coefficient $\mathbf{C_T}$ and the area A depends on the position on the actuator disc. This formulation gives a simple inhomogeneous force distribution, which does not have to rely on a more complex Blade Element Method (BEM) formulation that would become impractical in the following derivations.

The vectorial notation can be expressed using the Einstein notation:

$$F_i = -C_{Fi} \left(U_j n_j \right)^2 . \tag{6.14}$$

The velocity is then split into the averaged and fluctuating parts,

$$F_i = -C_{Fi} \left(\overline{U}_j n_j + u'_j n_j \right)^2 , \tag{6.15}$$

which can be expanded to

$$F_i = -C_{Fi} \, n_j n_k \left(\overline{U}_j \overline{U}_k + 2\overline{U}_j u'_k + u'_j u'_k \right) . \tag{6.16}$$

When the forces are averaged with respect to time, the $\overline{U} u'$ terms disappear

$$\overline{F_i} = -C_{Fi} \, n_j n_k \left(\overline{U}_j \overline{U}_k + \overline{u'_j u'_k} \right) . \tag{6.17}$$

Eq. (6.17) confirms the observation of Section 5.5.3 that the added term is relatively small compared to the square of the mean velocity ($\overline{u'_j u'_k} \ll \overline{U}_j \overline{U}_k$) and can be neglected most of the time.

However, as presented in Section 5.5.5, four terms have also been neglected in the k- and ε-equations, i.e. $\overline{F_k}$, $\overline{F_\varepsilon}$, $\overline{\Pi_k}$, $\overline{\Pi_\varepsilon}$,

$$\overline{F_k} = \overline{u'_i F_i} \quad \text{and} \quad \overline{F_\varepsilon} = 2\nu \overline{\frac{\partial F_i}{\partial x_j} \frac{\partial u'_i}{\partial x_j}}, \tag{6.18}$$

$$\overline{\Pi_k} = -\overline{u'_i \frac{\partial P}{\partial x_i}} \quad \text{and} \quad \overline{\Pi_\varepsilon} = -2\nu \overline{\frac{\partial^2 P}{\partial x_i \partial x_j} \frac{\partial u'_i}{\partial x_j}}. \tag{6.19}$$

Starting from the expression of F_i in Eq. (6.16), it is straightforward to derive $\overline{F_k}$ Eq. (6.21) and $\overline{F_\varepsilon}$ Eq. (6.22).
The k-equation is derived by taking the dot product of the Navier-Stokes Equations with the velocity vector U_i and time-averaging:

$$\overline{F_E} = -C_{Fi} \, n_j \, n_k \left(\overline{U}_i \overline{U}_j \overline{U}_k + 2\overline{u'_i u'_k} \, \overline{U}_j + \overline{u'_i u'_j u'_k} \right), \tag{6.20}$$

where there is a triple summation over i, j, k. The final step is then to remove the mean energy part, i.e. the triple mean velocity terms,

$$\overline{F_k} = -C_{Fi} \, n_j \, n_k \left(2\overline{u'_i u'_k} \, \overline{U}_j + \overline{u'_i u'_j u'_k} \right) . \tag{6.21}$$

Similarly, the ε-equation is derived from the Navier-Stokes Equations by differentiating with $\partial/\partial x_j$, then multiplying by $\partial u_i'/\partial x_j$ and time-averaging,

$$\overline{F_\varepsilon} = -2\nu \left[2\overline{\frac{\partial}{\partial x_l} \left(u_k' \overline{U_j} C_{Fi} \right) \frac{\partial u_i'}{\partial x_l}} + \overline{\frac{\partial}{\partial x_l} \left(u_j' u_k' C_{Fi} \right) \frac{\partial u_i'}{\partial x_l}} \right] n_j n_k, \qquad (6.22)$$

where there is a quadruple summation over i, j, k, and l.

From this point, it becomes difficult to justify further approximations without a in-depth knowledge of turbulence modelling.

Canopy Modelling

Forest and urban canopies can also be modelled by accounting for the effect of the obstacles with body forces. A significant effort has been made on modelling atmospheric boundary layer turbulence together with the canopy flow. The k-ε model has also been used in that context and extended using a similar theory as that introduced in the previous section. A common approach (Sanz [77], Sogachev et al. [87, 86]) is to neglect the terms $\overline{u_i' u_j' u_k'}$ and $\overline{\frac{\partial u_j' u_k'}{\partial x_l} \frac{\partial u_i'}{\partial x_l}}$ and to model the other terms using k and ε. They also add a source term of turbulence based on the cube of the local mean velocity. The following formulas are quoted from [77] and are related to Eq. (6.21) and Eq. (6.22), wheb the flow is assumed to be directly normal to the wind turbine disc. S_k is the added source/sink term to the k-equation,

$$S_k = C_F \left(\beta_p U^3 - \beta_d U k \right), \qquad (6.23)$$

where C_F is the canopy drag, equivalent to the force coefficient and β_p and β_d are two modelling parameters (where $_p$ stands for production and $_d$ for dissipation).
S_ε is the added source/sink term of the ε-equation,

$$S_\varepsilon = C_F \left(C_{\varepsilon p} \beta_p \frac{\varepsilon}{k} U^3 - C_{\varepsilon d} \beta_d U \varepsilon \right), \qquad (6.24)$$

where $C_{\varepsilon p}$ and $C_{\varepsilon d}$ are two model closure parameters.

In the previous derivations Eq. (6.21) and Eq. (6.22), the source term in the k-equation does not retain the triple mean velocity terms $\overline{U}_i \overline{U}_j \overline{U}_k$, as they are considered to be extracted from the mean kinetic energy of the flow. Although, as noticed in the full rotor computation Section 3.3.2, part of the energy extracted by the wind turbine from the mean kinetic energy

is transformed into small-scale turbulence. For this reason, the parameter β_p is positive and included between $[0, 1]$. As a large part of the energy is extracted from the system as mechanical work of the generator, or directly lost through frictions as heat, only a fraction of the energy is transfered as turbulence ($\beta_p \ll 1$).

However, the reason of the appearance of the term U^3 in the ε-equation is less clear. Sanz [77] uses the Kolmogorov relation to explain how the source term in the ε-equation S_ε is found. A source of turbulence eventually decays and, therefore, introduces somehow a source of dissipation.

The intended effect of this model is illustrated on Fig. 6.1. The added turbulence induced by the rotor geometry (modelled by the U^3 terms) occurs in the small-scale part of the u-spectrum, where the frequency are high. On the large-scale part of the spectrum, the turbine extracts some the energy at lower frequencies (modelled by the kU and εU terms). However, in the k-ε model, all the turbulence scales are modelled at the same time in the k and ε values. It is therefore not directly possible to control the effect of removed large scales or added small scales other than changing the values of k and ε.

Sogachev [86] argues that in forests these two quantities of energy are identical and cancel each other. For this effect to be true, it would mean that no energy is lost as heat or extracted from the turbulence and that the small-scale vortex structures generated by the trees contain exactly the amount of energy contained in the atmospheric large-scale eddies broken down by the forest.

However, the full-rotor computation in Section 3.3.2 showed that even with a laminar inflow, turbulence vortex structures appear in the wake, so that their energy does come from the mean kinetic energy independently from the large-scale turbulence. Similarly, the LES showed that the sink of large-scale turbulence can exist without a conversion into small-scale turbulence. These two independent observations show that it is unlikely that the two numbers cancel each other in the case of wind turbines.

Application of the Canopy Model for Wind Turbines

The modified k-ε for canopy can be applied almost directly for the wind turbine case, although the β_p parameter is expected to be much lower than in the case of a forest. Unfortunately, the model only acts at the position where the forces are applied, while the wind turbine is expected to influence the turbulence on a wider region upstream and downstrem of the wind turbine, through the work of the pressure gradient. In order to model, as well, the influence of the induced pressure gradient over the local turbulence,
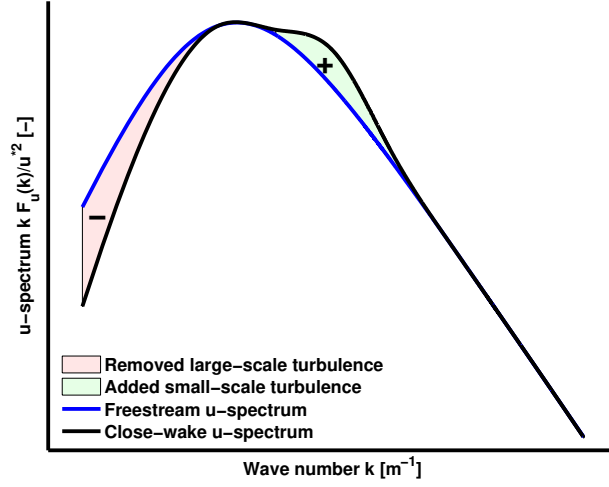
Figure 6.1: Illustration of the modelled u-spectrum in the close wake-region.

the two terms Π_k and Π_ε need to be modelled based on the wind turbine characteristics.

The Π_* terms have a smoothing effect over their corresponding force terms F_*, where they tend to counter act the effect of the force terms locally, while adding some more effect in the vicinity of the forces. This effect is similar to the effect of the pressure gradient with respect to the discrete forces at the actuator disc position. When the discrete forces are applied in the Navier-Stokes Euqations, the pressure gradient is acting as a smoothing function to redistribute gradually the force action spatially (Fig. 6.2).

In order to reproduce this effect, the forces component calculated using the adapted canopy model are spread out using a smoothing distribution under the condition that the sum of the effect is conserved. With this approach, Eq. (6.23) becomes Eq. (6.25) and Eq. (6.24) becomes Eq. (6.26).
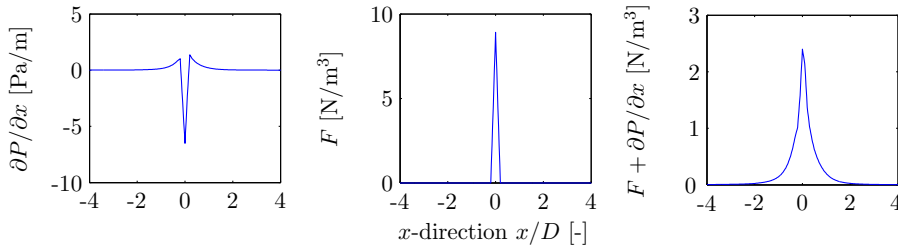

Figure 6.2: The pressure gradient smooths the discrete forces

$$S_k = C_F \left[\beta_p U^3 - \beta_d U k \, \mathcal{G} \left(\frac{\mathbf{x} - \mathbf{x_D}}{D} \right) \right], \tag{6.25}$$

and

$$S_\varepsilon = C_F \left[C_{\varepsilon p} \beta_p \frac{\varepsilon}{k} U^3 - C_{\varepsilon d} \beta_d U \varepsilon \, \mathcal{G} \left(\frac{\mathbf{x} - \mathbf{x_D}}{D} \right) \right], \tag{6.26}$$

where $\mathcal{G}$ is a smoothing function. Note that the spreading function only concerns the sink of turbulence and dissipation (i.e. kU and εU terms). The source terms primarily act at the position of the disc.

6.3 Results

The different models introduced in the previous section are compared with the LES_{VF} model presented in Chapter 5 and with the measurements presented in Chapter 4. The mesh and setup used to obtain the results are the same as described previously.

6.3.1 Comparison to LES

As it was mentioned in Section 5.3.3, as the averaging time is small, the turbulence kinetic energy level is not as high as it should be. Consequently, the comparison is only qualitative and is focussed on the trends.

El Kasmi-Masson Model

The model of El Kasmi and Masson [35] has two independent parameters: the model constant $C_{\varepsilon 4}$ and the size of the region where the model is applied. In practice, some tests showed that increasing the region had a similar effect than increasing the model constant. The cases illustrated on Fig. 6.3 and Fig. 6.4 represents a parametric study on the model constant $C_{\varepsilon 4}$. In the cases considered, the region where the model is applied is a cylinder centered at the disc position. The cylinder's diameter and its length are two times larger than the rotor diameter.

By increasing the constant, the dissipation ε is increased in the region of large velocity shear. The direct effect is an immediate reduction of the eddy-viscosity (Fig. 6.3c).

The production of turbulence is also balanced by this increase of ε, which indirectly slows down the recovery of the eddy-viscosity (Fig. 6.4c).

Increasing the constant tends to preserve the axial velocity deficit over a longer distance (Fig. 6.3a and Fig. 6.4a). However, for an equivalent deficit and inflexion point to LES (e.g. $C_{\varepsilon 4} = 0.001$), the recovery of the wake occurs at a slower rate compared to LES_{VF}.

The TKE k of El Kasmi-Masson presents different trends according to the parameter used (Fig. 6.4b). However, they all are significantly different than

the TKE of LES_{VF}.

Moreover, the sudden increase of ε at the disc, visible in the El Kasmi-Masson model, is in complete disagreement with the LES_{VF} results (Fig. 6.4d). On the contrary, as it was noticed in the previous chapter, LES_{VF}'s ε has a very small decrease at the position of the disc and slowly increases to a peak located at $x = 5D$.

Figure 6.3: Parametric study on the El Kasmi-Masson model [35]. The added term in the ε-equation is applied in a cylindrical region surrounding the actuator disc ($\pm 1D$). Three different variables $C_{\varepsilon 4}$ are compared to LES_{VF}. The contours represent the axial velocity, TKE and eddy-viscosity ($\nu_t^{k\text{-}\varepsilon}$, ν_t^{LES2}), all normalized with corresponding inflow values. The contours are extracted on a horizontal plane at hub height. The white line shows the actuator disc position.
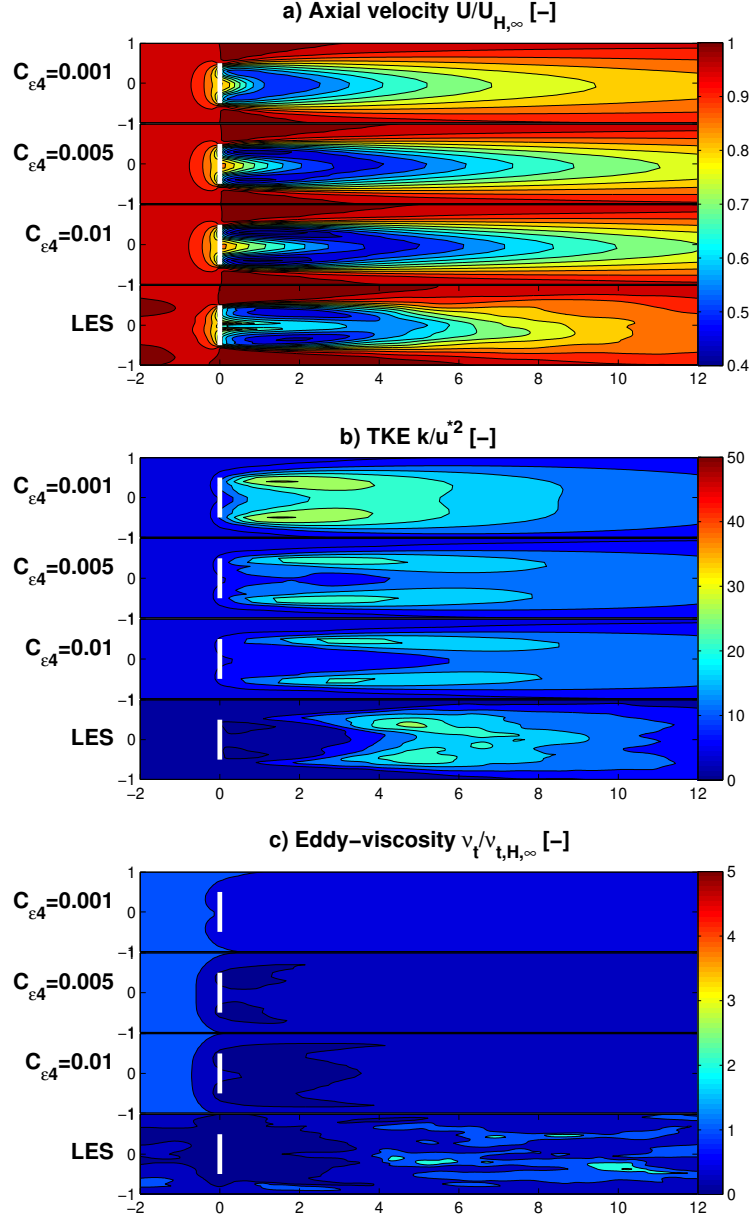
Figure 6.4: Parametric study on the El Kasmi-Masson model [35]. The added term in the ε-equation is applied in a cylindrical region surrounding the actuator disc ($\pm 1D$). Three different variables $C_{\varepsilon 4}$ are compared to LES_{VF} and standard k-ε. The lines represent the axial velocity, TKE, eddy-viscosity ($\nu_t^{k\text{-}\varepsilon}$, ν_t^{LES2}) and dissipation, all normalized with corresponding inflow values. The lines are extracted along a normal axis to the disc at hub height and $y = -0.25D$.

Adverse Pressure Gradient Model

The adverse pressure gradient (APG) model is based on a reduction of the eddy-viscosity in the region of adverse pressure gradient. The eddy-viscosity is reduced in a spherical region of given radius, centered around the position of the disc. Fig. 6.5 and Fig. 6.5 presents three test cases, with a different spherical radius.

The eddy-viscosity is reduced to its threshold value $\mu_{tsh} = 0.1$ in the corresponding spherical regions (Fig. 6.5c and Fig. 6.6c). However, as soon as the flow leaves this region, the eddy-viscosity is rapidly increased. This sudden increase is in clear contrast with the LES_{VF} results.

The APG model axial velocity follows the LES_{VF} trend inside the reduced eddy-viscosity region (Fig. 6.5a). Downstream of the low eddy-viscosity region, the wake is dissipated rapidly.

k and ε both present similar characteristics (Fig. 6.6b and d).

The poor performance of the APG model shows that it is not an appropriate way to model the turbulence. Simply cancelling the eddy-viscosity in the adverse-pressure gradient is not enough to influence the trend of the wake recovery outside the region where it is acting. As soon as the flow leaves the region of reduced eddy-viscosity, the eddy-viscosity based on k and ε takes over starts to act through the Reynolds-stresses.

This model only adresses the first assumption of the Boussinesq's approximation. In the region where it is acting, the different terms behave in very good agreement with the LES. However, the wake region downstream is clearly unphysical. This is in large part due to the velocity linearity assumption of the Boussinesq's approximation, which is not accounted by this model.
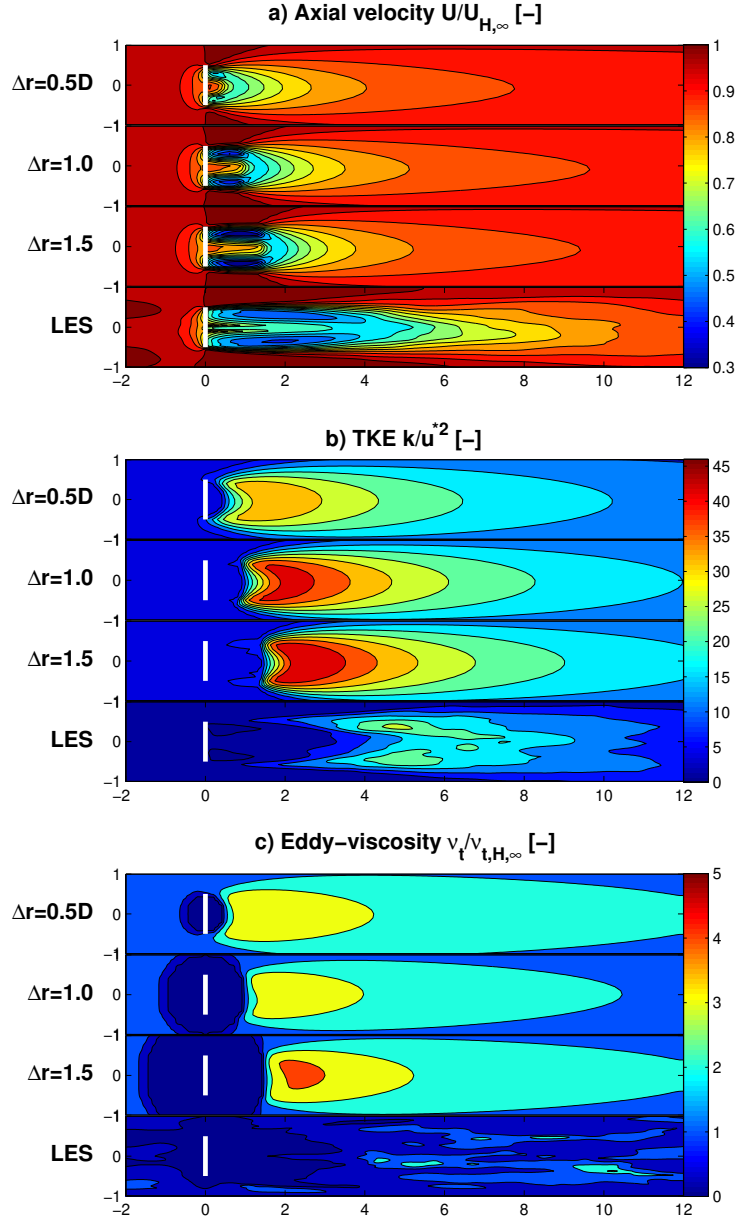
Figure 6.5:   Parametric study on the adverse pressure gradient model. The eddy-viscosity is reduced to the threshold value in a spherical region ($\Delta r = 0.5D, 1.0D, 1.5D$) and is compared to LES_{VF}. The contours represent the axial velocity, TKE and eddy-viscosity ($\nu_t^{k\text{-}\varepsilon}$, ν_t^{LES2}), all normalized with corresponding inflow values. The contours are extracted on a horizontal plane at hub height. The white line shows the actuator disc position.
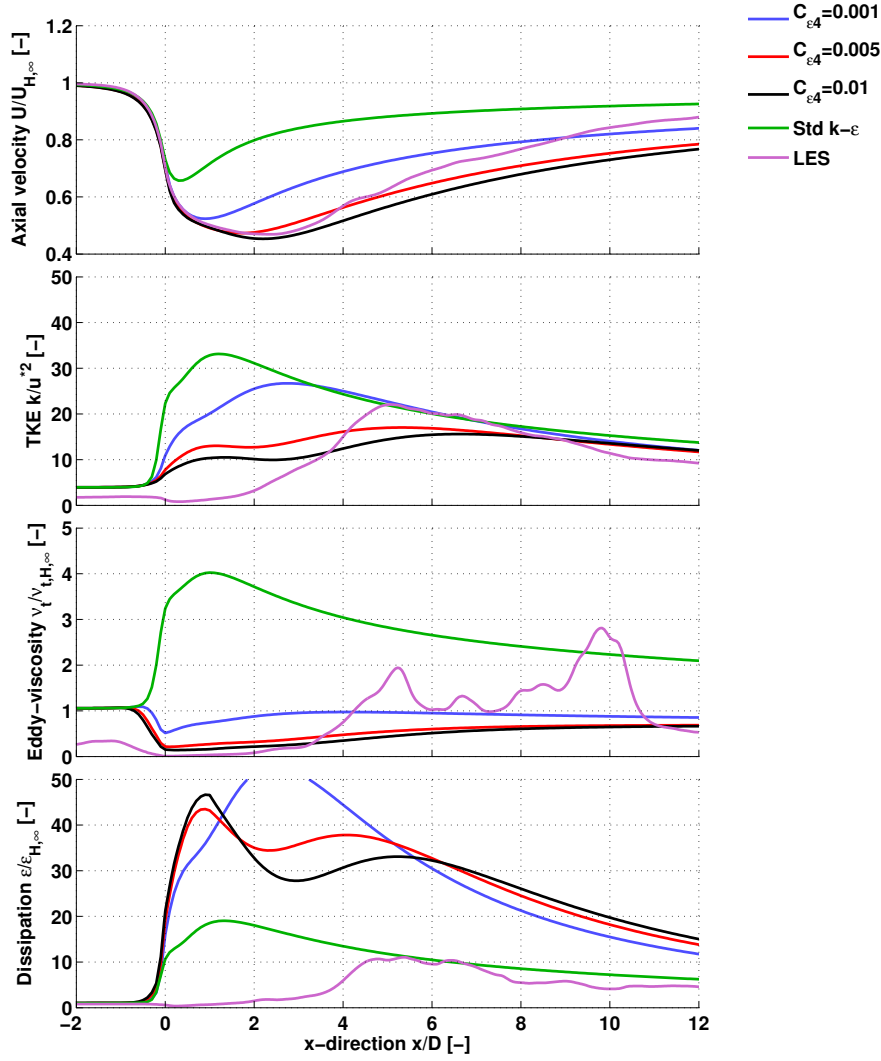
Figure 6.6: Parametric study on the adverse pressure gradient model. The eddy-viscosity is reduced to the threshold value in a spherical region ($\Delta r = 0.5D, 1.0D, 1.5D$) and is compared to LES_{VF} and standard k-ε. The lines represent the axial velocity, TKE, eddy-viscosity ($\nu_t^{k\text{-}\varepsilon}$, ν_t^{LES2}) and dissipation, all normalized with corresponding inflow values. The lines are extracted along a normal axis to the disc at hub height and $y = -0.25D$.

Realizability Model

Fig. 6.7 and Fig. 6.8 compare three different constants C_{Swz} to the LES_{VF}. The standard Realizability model, which corresponds to a constant $C_{\mathrm{Swz}} = 1.0$, reduces the eddy-viscosity to a value lower than the atmospheric inflow condition, in the region surrounding the disc (Fig. 6.7c). It presents similar trends compared to the APG model applied on a spherical region of radius $\Delta r = 1.0D$ (Fig. 6.8a,b,c,d and Fig. 6.6a,b,c,d).

When the constant C_{Swz} is reduced, the wake is preserved over larger distances (Fig. 6.7a) and the region of action of the low eddy-viscosity is increased as well (Fig. 6.7c). The model acts mainly in the high velocity shear regions such as at the interfaces of the wake and in the region of influence of the adverse pressure gradient. The model with a parameter value of $C_{\mathrm{Swz}} = 0.4$ gives a similar trend as the LES_{VF} for the axial-velocity (Fig. 6.8a). The TKE, however, starts to increase downstream of the disc position, which contrasts with the LES_{VF} results (Fig. 6.8b).

In the region where the model does not act, in the central part of the wake, the eddy-viscosity is increased to a relatively high level compared to the inflow values. This sudden increase is in contrast with the slower increase of the LES_{VF} (Fig. 6.7c).

The region of action of the model, at the interface of the wake, can extend up to $x = 10D$ with the parameter $C_{\mathrm{Swz}} = 0.4$.

The dissipation ε has a similar trend compared to the LES_{VF} (Fig. 6.8d). The Realizability model successfully avoids the build up of ε seen in the standard k-ε model (Fig. 5.10).
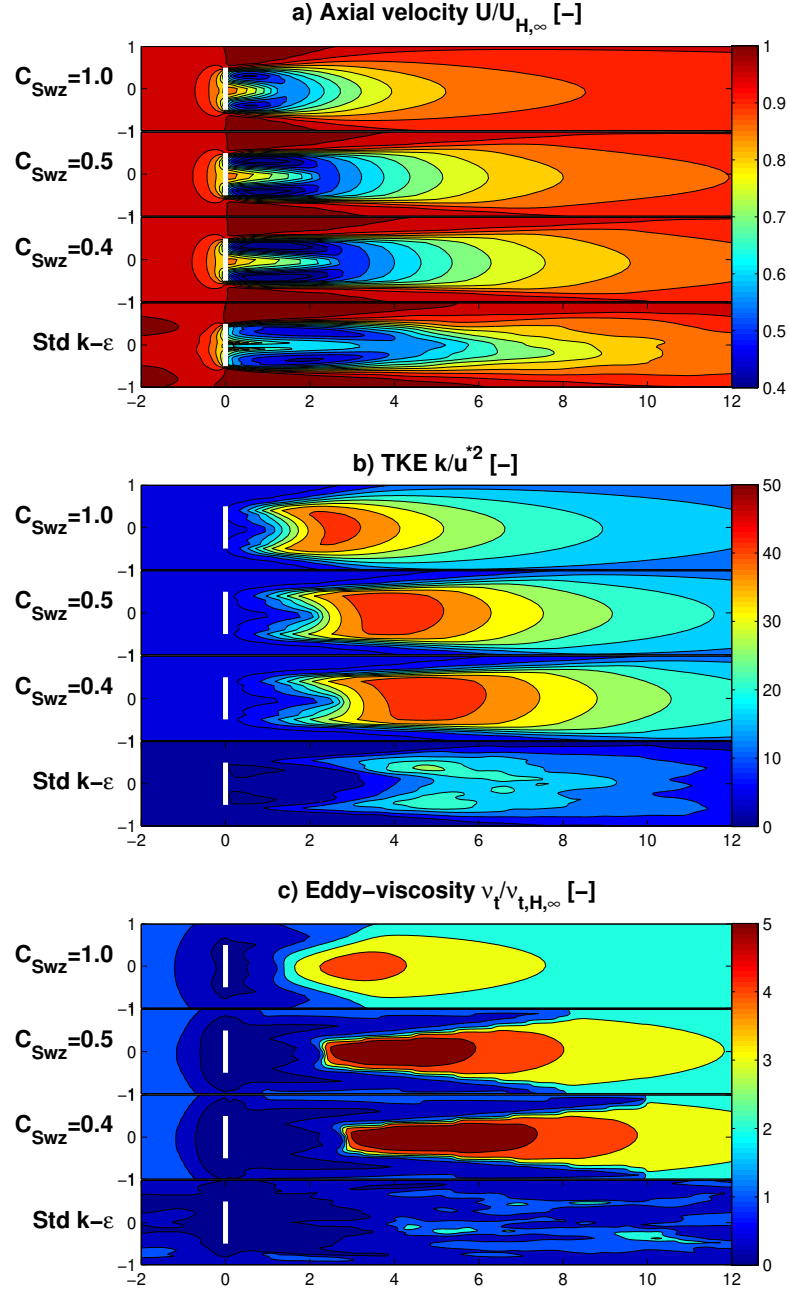
Figure 6.7: Parametric study on the Realizability model. Three scaling parameters ($C_{\text{Swz}} = 1.0, 0.5, 0.4$) are compared to LES_{VF}. The contours represent the axial velocity, TKE and eddy-viscosity ($\nu_t^{k\text{-}\varepsilon}$, ν_t^{LES2}), all normalized with corresponding inflow values. The contours are extracted on a horizontal plane at hub height. The white line shows the actuator disc position.
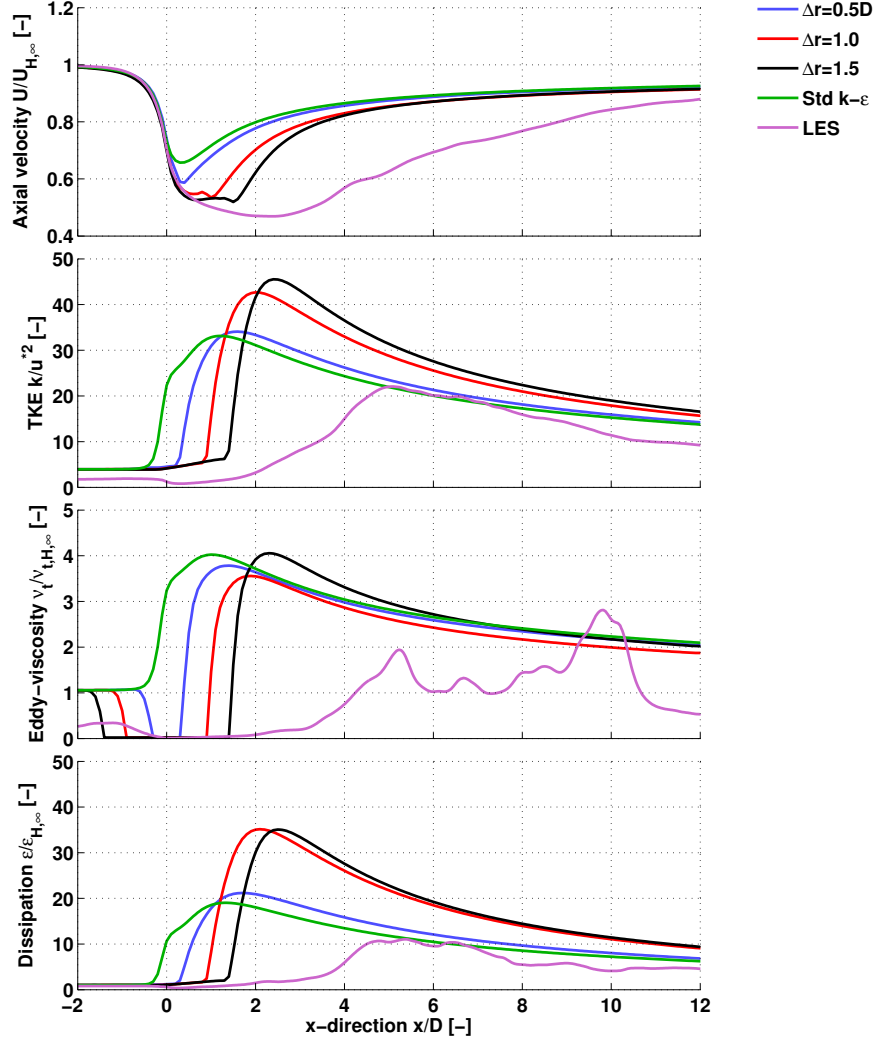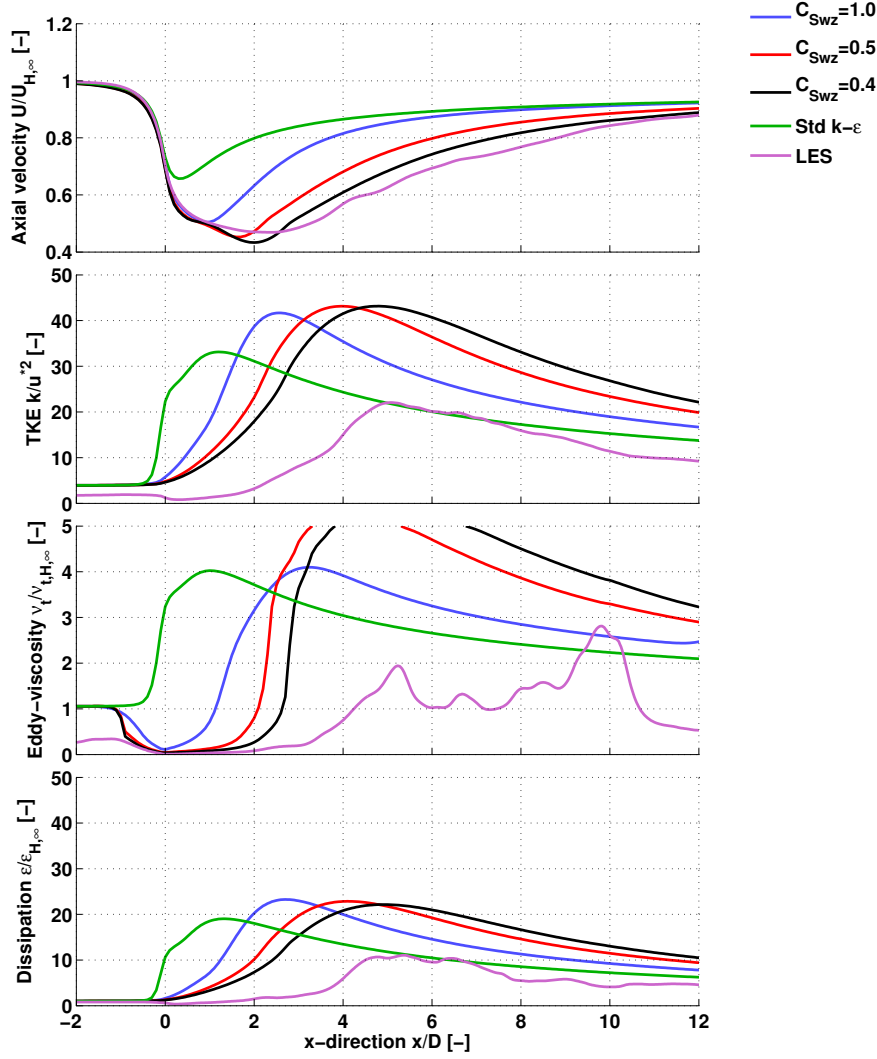
Figure 6.8: Parametric study on the Realizability model. Three scaling parameters ($C_{\mathrm{Swz}} = 1.0, 0.5, 0.4$) are compared to LES_{VF} and standard k-ε. The lines represent the axial velocity, TKE, eddy-viscosity ($\nu_t^{k\text{-}\varepsilon}$, ν_t^{LES2}) and dissipation, all normalized with corresponding inflow values. The lines are extracted along a normal axis to the disc at hub height and $y = -0.25D$.

Wind Turbine Canopy Model

The Canopy model of Sanz [77] is compared to the LES_{VF} model. Only the large-scale part of the model is considered (i.e. the dissipative terms in the k and ε equation). As there is no production of small-scale turbulence modelled in the LES_{VF}, it would not be a fair comparison to model them the k-ε model. The two production parameters are consequently set to zero ($\beta_p = 0.0$ and $C_{\varepsilon p} = 0.0$).

Three sets of parameters are presented in Fig. 6.9 and Fig. 6.10. The first set uses the constants $\beta_p = 1.0$ and $C_{\varepsilon p} = 1.0$ and is similar in trends with the standard k-ε model (Fig. 6.10).

There is a significant difference with the second set of constants considered, where the ε term is cancelled (i.e. $C_{\varepsilon d} = 0.0$). The TKE increase is significantly delayed to a position $x = 1D$ downstream of the wind turbine. This is an interesting result as it was observed in Section 5.5.5 that the dissipative term in the ε-equation is not expected to have a significant influence, as it is several orders of magnitude smaller than other terms such as the "dissipation stretching" ($C_{\varepsilon 2}\varepsilon^2/k$). This indicates that the parameter used $C_{\varepsilon d}$ should be small enough to make the term of negligible influence.

For a larger value for the parameter, $\beta_d = 2.0$ and no dissipative terms ($C_{\varepsilon d} = 0.0$), the TKE is significantly affected and even has a value lower than the inflow condition (Fig. 6.10b). While it does decrease the eddy-viscosity momentarily (Fig. 6.10c), it is not enough to preserve the wake in a similar fashion as the LES model (Fig. 6.10a).

Increasing further the parameter β_d can yield a negative k, which produces unphysical results.
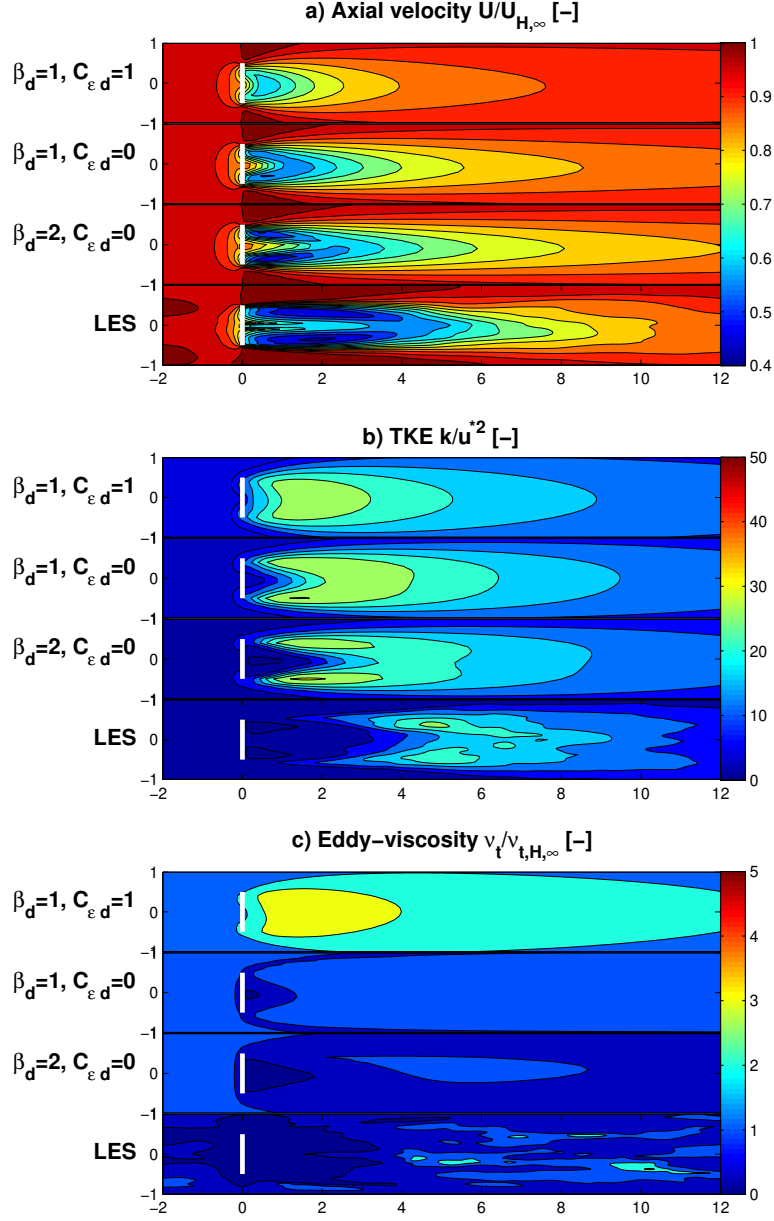
Figure 6.9: Parametric study on the Canopy model of Sanz. The U^3 terms are not considered ($\beta_p = 0$ and $C_{\varepsilon p} = 0$). Three cases (($\beta_d, C_{\varepsilon d}) \in \{(1.0, 1.0), (1.0, 0.0), (2.0, 0.0)\}$) are compared to LES_{VF}. The contours represent the axial velocity, TKE and eddy-viscosity ($\nu_t^{k\text{-}\varepsilon}$, ν_t^{LES2}), all normalized with corresponding inflow values. The contours are extracted on a horizontal plane at hub height. The white line shows the actuator disc position.
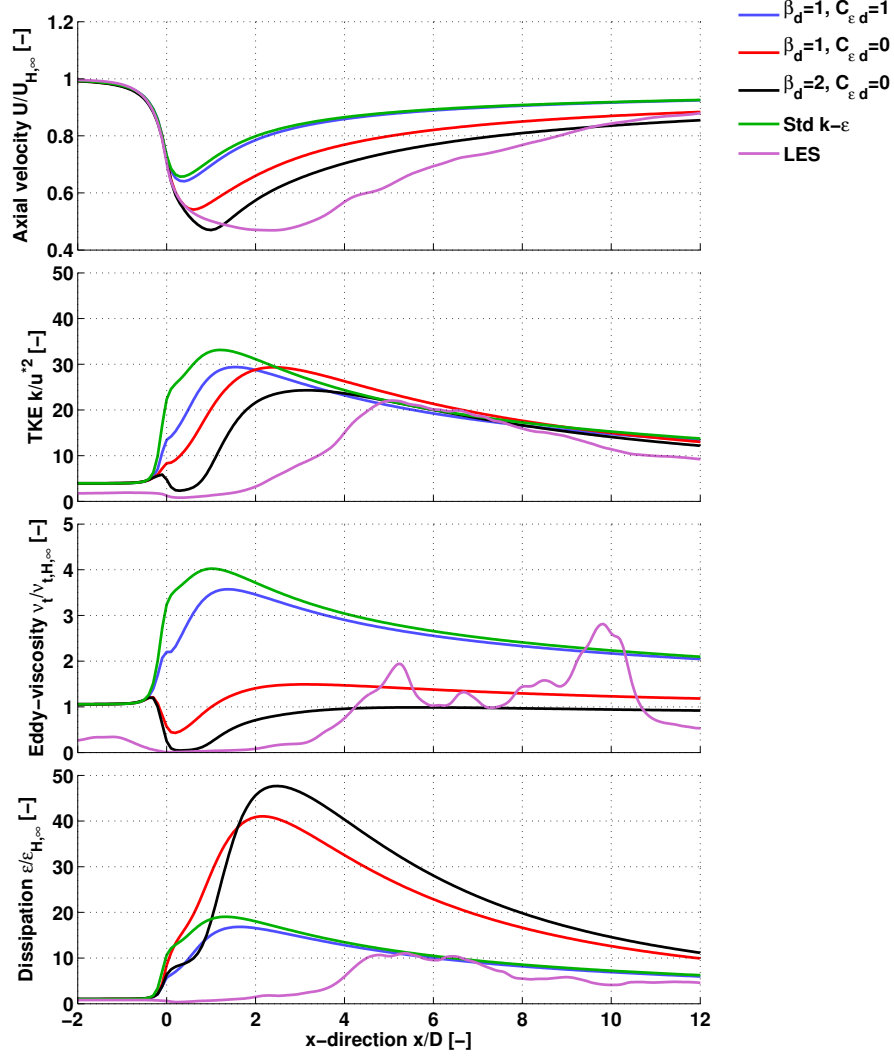
Figure 6.10: Parametric study on the Canopy model of Sanz. The U^3 terms are not considered ($\beta_p = 0$ and $C_{\varepsilon p} = 0$). Three cases (($\beta_d, C_{\varepsilon d}) \in \{(1.0, 1.0), (1.0, 0.0), (2.0, 0.0)\}$) are compared to LES_{VF} and standard k-ε. The lines represent the axial velocity, TKE, eddy-viscosity ($\nu_t^{k\text{-}\varepsilon}$, ν_t^{LES2}) and dissipation, all normalized with corresponding inflow values. The lines are extracted along a normal axis to the disc at hub height and $y = -0.25D$.

Realizability & Canopy Model

The Realizability model and the Canopy model are combined together and compared to LES_{VF}. Based on the observations made in the previous section, only the parameter β_p is kept non-null.

The standard Realizability model ($C_{\text{Swz}} = 1.0$), combined with the canopy model performs likewise as the standard Realizability model alone (Fig. 6.12 and Fig. 6.8). The main difference are visible on the trend of the eddy-viscosity (Fig. 6.12c and Fig. 6.8c) and the dissipation (Fig. 6.12d and Fig. 6.8d).

With smaller parameter values (e.g. $C_{\text{Swz}} = 0.5$), there is a visible improvement of the TKE (Fig. 6.12b and Fig. 6.8b). The initial behaviour of the TKE downstream of the wind turbine is in better agreement with the LES_{VF}. The eddy-viscosity also has a slower increase downstream of the region where the model acts directly.

The combination of the two models does not modify significantly the axial velocity in the wake compared to the Realizability model. However it does contribute to smoothing out the rapid increase of turbulence and eddy-viscosity that occurred when the flow left the region of influence of the model. Finally, the shape of the contour look slightly more similar to the LES_{VF}.
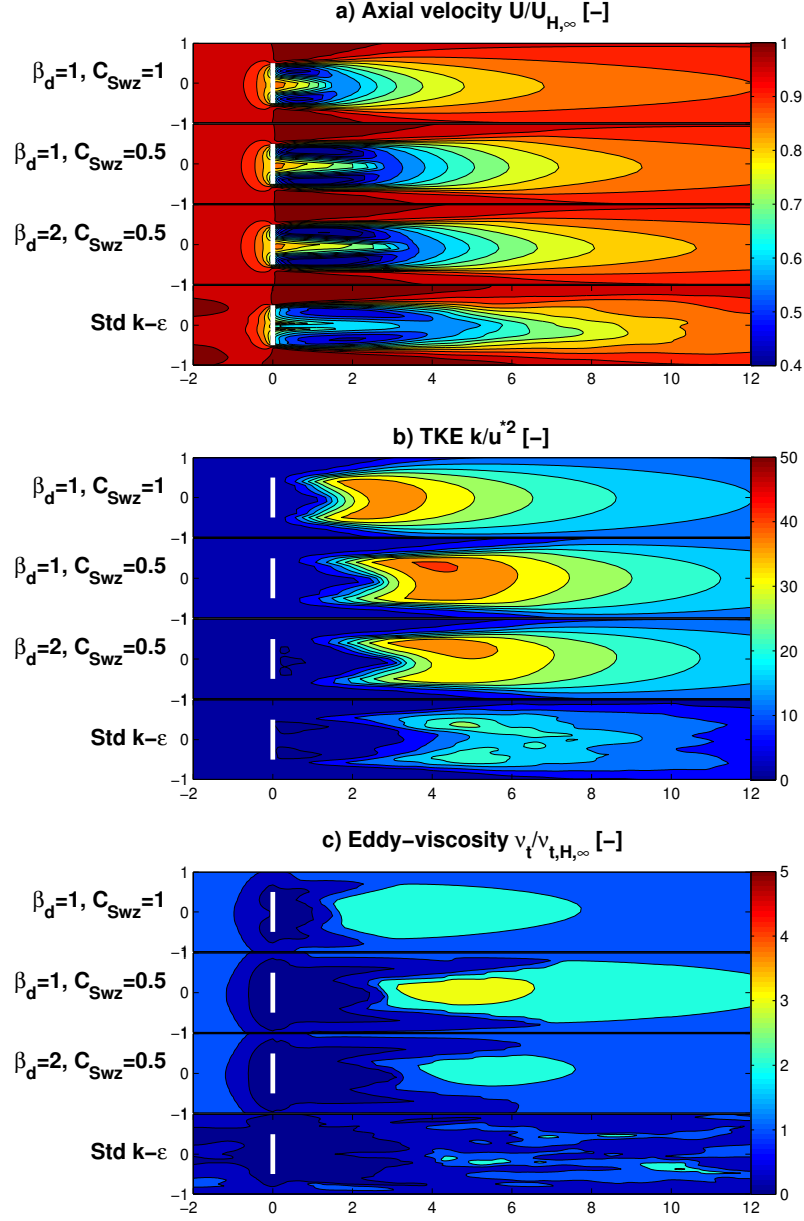
Figure 6.11: Parametric study on the combination of the Canopy and the Realizability model. Three sets of parameters are compared to LES_{VF} (($\beta_d, C_{\varepsilon d}, C_{\mathrm{Swz}}) \in \{(1.0, 0.0, 1.0), (1.0, 0.0, 0.5), (2.0, 0.0, 0.5)\}$). The contours represent the axial velocity, TKE and eddy-viscosity ($\nu_t^{k\text{-}\varepsilon}$, ν_t^{LES2}), all normalized with corresponding inflow values. The contours are extracted on a horizontal plane at hub height. The white line shows the actuator disc position.
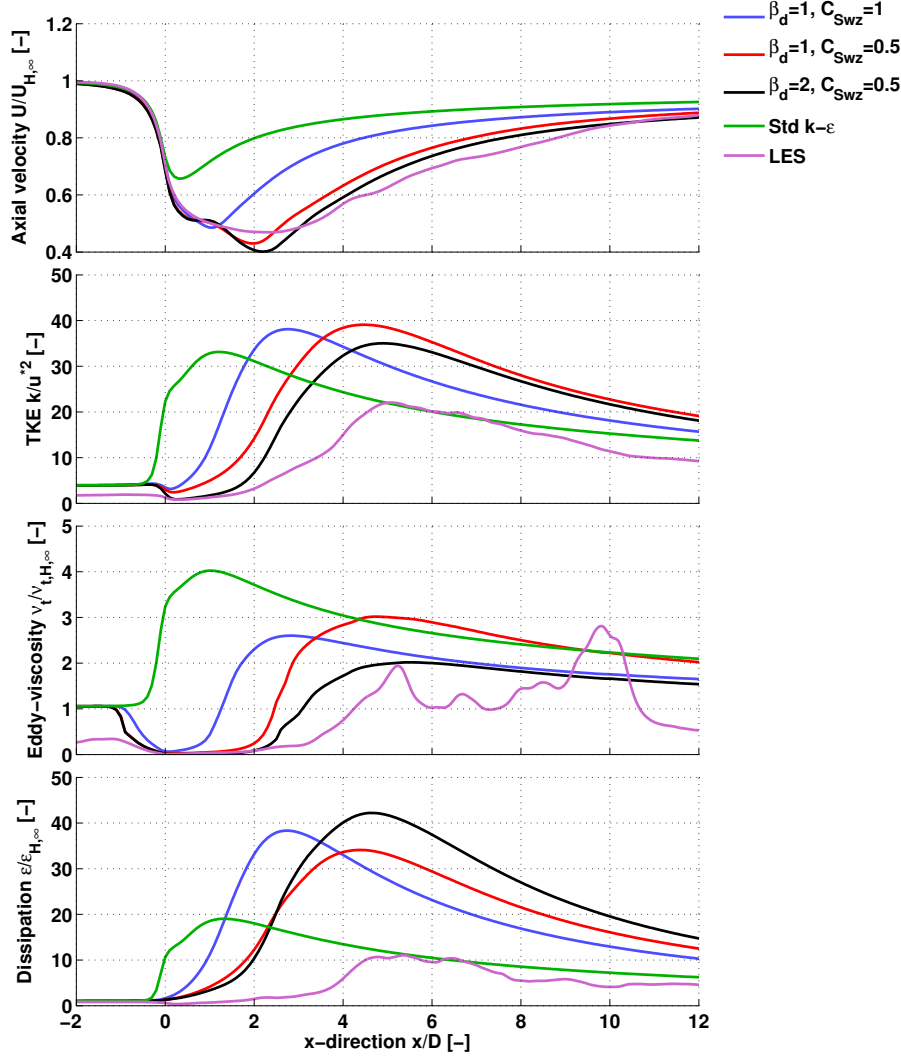
Figure 6.12: Parametric study on the combination of the Canopy and the Realizability model. Three sets of parameters are compared to LES_{VF} and standard k-ε $((\beta_d, C_{\varepsilon d}, C_{\mathrm{Swz}}) \in \{(1.0, 0.0, 1.0), (1.0, 0.0, 0.5), (2.0, 0.0, 0.5)\})$. The lines represent the axial velocity, TKE, eddy-viscosity ($\nu_t^{k\text{-}\varepsilon}$, ν_t^{LES2}) and dissipation, all normalized with corresponding inflow values. The lines are extracted along a normal axis to the disc at hub height and $y = -0.25D$.

6.3.2 Comparison to Measurements

The methods presented in the previous section are compared to single wake measurements from two wind turbines, Nibe [94] and Sexbierum [22]. The two datasets are presented in Section 4.3.

El Kasmi-Masson Model

The El Kasmi-Masson model is able to preserve the wake deficit until the first met.mast in the two datasets, which are both located at a distance $x = 2.5D$ downstream of the wind turbine (Fig. 6.13 and Fig. 6.14). Using the constant originally proposed by El Kasmi-Masson [35] ($C_\varepsilon = 0.37$), the axial velocity deficit at $x = 2.5D$ has the same magnitude as the measurements, in the two datasets. However, the wake does not recover fast enough to match the following two masts measurements.

The turbulence intensity, in the Sexbierum Test Case, is significantly lower than the measurements at the first met.mast. Decreasing the constant does increase the turbulence intensity, while at the same time it reduces the wake deficit. It does not seem possible to obtain a perfect fit that matches all the measurements at all the met.mast positions.
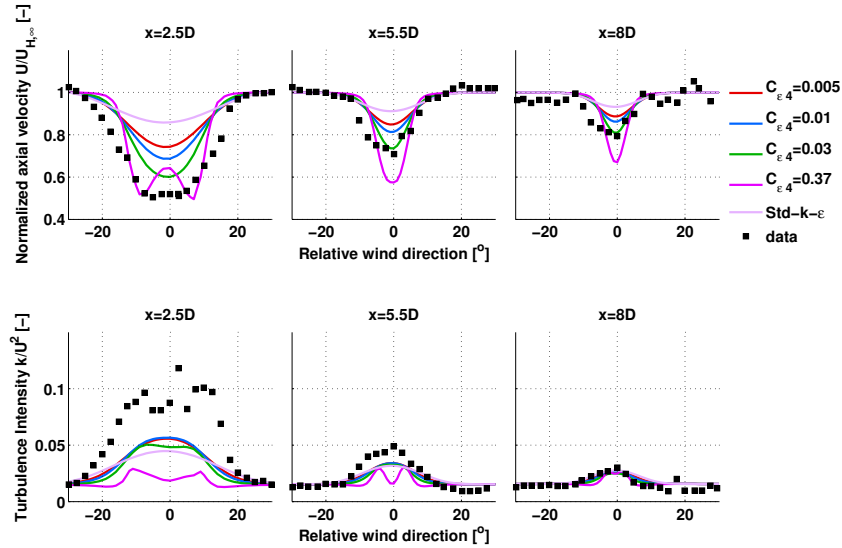
Figure 6.13: Sexbierum Test Case. Parametric study on the El Kasmi-Masson model. The added term in the ε-equation is applied in a cylindrical region surrounding the actuator disc ($\pm 1D$). Three different variables $C_{\varepsilon 4}$ are compared to the standard k-ε model. The axial velocity ($U/U_{H,\infty}$) and the turbulence intensity (k/U^2) horizontal profile is plotted at the position of three met.masts downstream of the wind turbine.

Figure 6.14: Nibe Test Case. Parametric study on the El Kasmi-Masson model. The added term in the ε-equation is applied in a cylindrical region surrounding the actuator disc ($\pm 1D$). Three different variables $C_{\varepsilon 4}$ are compared to the standard k-ε model. The axial horizontal and vertical velocity profile is plotted at the position of three met.masts downstream of the wind turbine. The vertical inflow profile is indicated as a black dot line.

Realizability Model

The standard Realizability model ($C_{\mathrm{Swz}} = 1.0$) performs slightly better than the standard k-ε model (Fig. 6.15 and Fig. 6.16). It is, however, not enough to obtain satisfying results, in comparison to the measurements both in terms of axial velocity deficit and in terms of turbulence intensity.

By decreasing the parameter C_{Swz}, it is possible to obtain an axial velocity deficit in better agreement with the measurements. However, it is difficult to obtain an axial velocity correct both for the first and second mast. The best fit is obtained using the parameter value $C_{\mathrm{Swz}} = 0.3$ for both sets of measurements.

The wake width is significantly larger in the measurements of the Sexbierum Test Case than in the computation. The Realizability model does not seem to be able to preserve the central wake deficit and at the same time having a sufficient wake spreading.

Figure 6.15: Sexbierum Test Case. Parametric study on the Realizability model. Four different parameters C_{Swz} are compared to the standard k-ε model. The axial velocity ($U/U_{H,\infty}$) and the turbulence intensity (k/U^2) horizontal profile is plotted at the position of three met.masts downstream of the wind turbine.
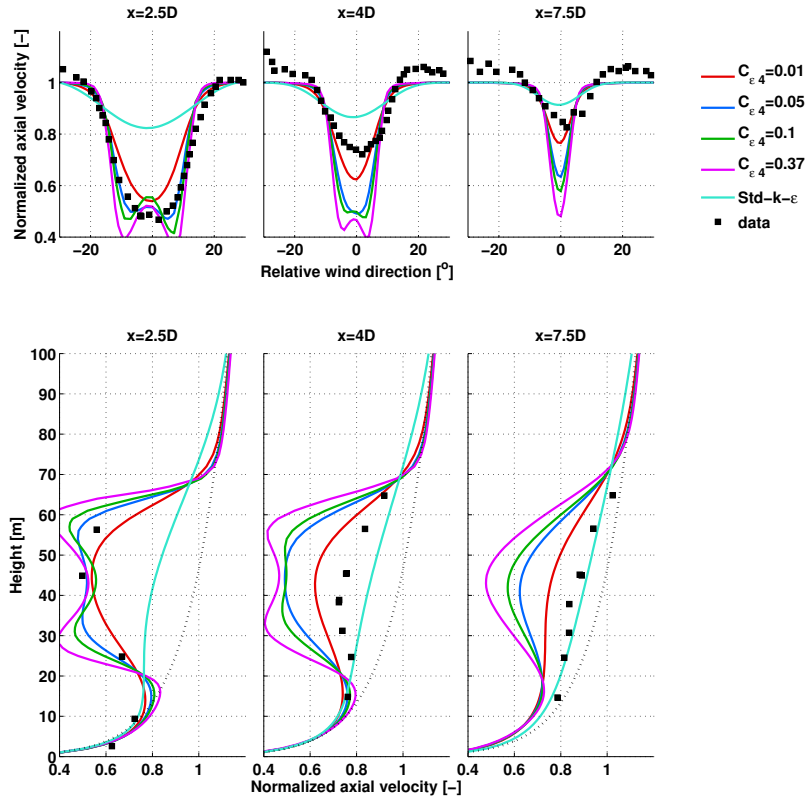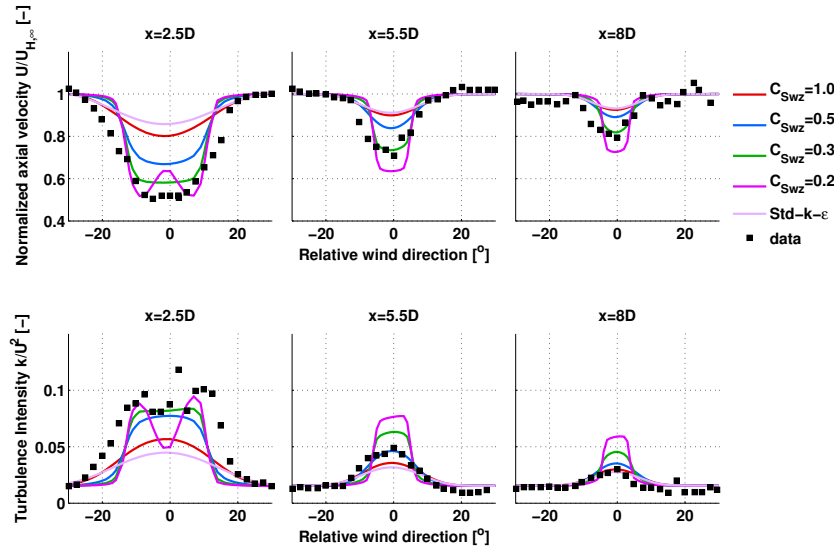
Figure 6.16: Nibe Test Case. Parametric study on the Realizability model. Five different parameters C_{Swz} are compared to the standard k-ε model. The axial horizontal and vertical velocity profile is plotted at the position of three met.masts downstream of the wind turbine. The vertical inflow profile is indicated as a black dot line.

Realizability-Canopy Model

The combination of the Realizability model and the Canopy model gives equivalent results compared to the Realizability model alone for the axial-velocity (Fig. 6.17 and Fig. 6.15). However, the turbulence intensity in the wake is significantly smaller than the measurements. The Realizability-Canopy model has a slightly larger wake width and a more realistic vertical wake shape than the Realizability model (Fig. 6.18 and Fig. 6.15).

The best fit with the measurements is obtained using the set of parameters $C_{\mathrm{Swz}} = 0.3$ and $\beta_d = 1.0$ for the Sexbierum dataset and $C_{\mathrm{Swz}} = 0.5$ and $\beta_d = 1.0$ for the Nibe dataset.

It is important to note that, here, the production terms of the Canopy model, as well as the dissipative term of the ε-equation have been neglected ($\beta_p = 0.0$, $C_{\varepsilon p} = 0.0$ and $C_{\varepsilon d} = 0.0$). There is a contribution from the added small-scale turbulence to the wake characteristics, that could potentially influence the wake recovery. However, adding these terms is in practice equivalent to reducing the dissipative terms and, therefore, does not make sense in the context of a parametric study.
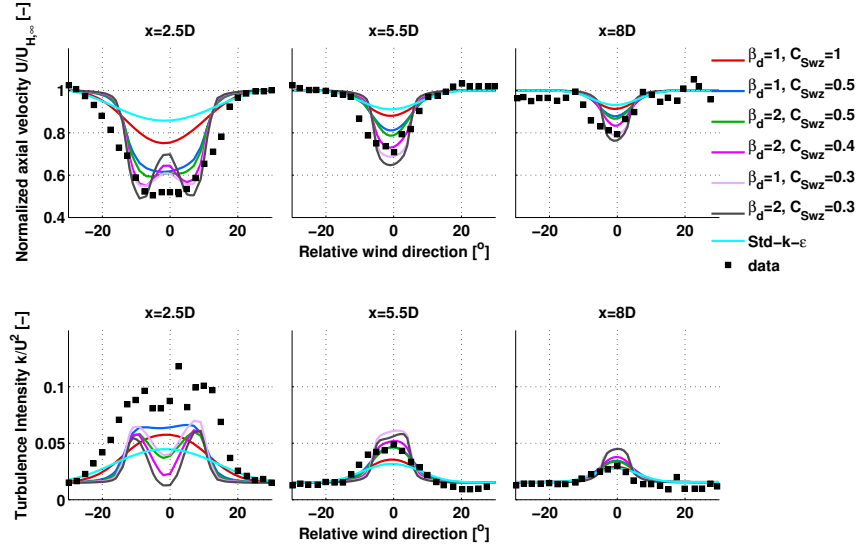
Figure 6.17: Sexbierum Test Case. Parametric study on the Realizability-Canopy model. Only the k term is considered in the Canopy model ($C_{\varepsilon d} = 0.0$, $\beta_p = 0.0$, $C_{\varepsilon p} = 0.0$). Six different sets of parameters are compared to the standard k-ε model. The axial velocity ($U/U_{H,\infty}$) and the turbulence intensity (k/U^2) horizontal profile is plotted at the position of three met.masts downstream of the wind turbine.
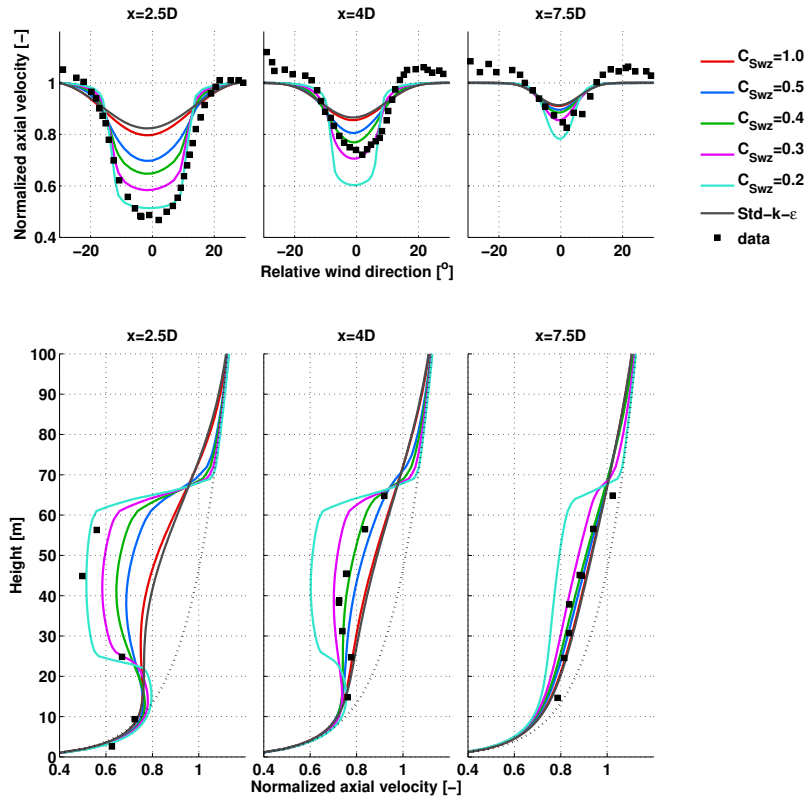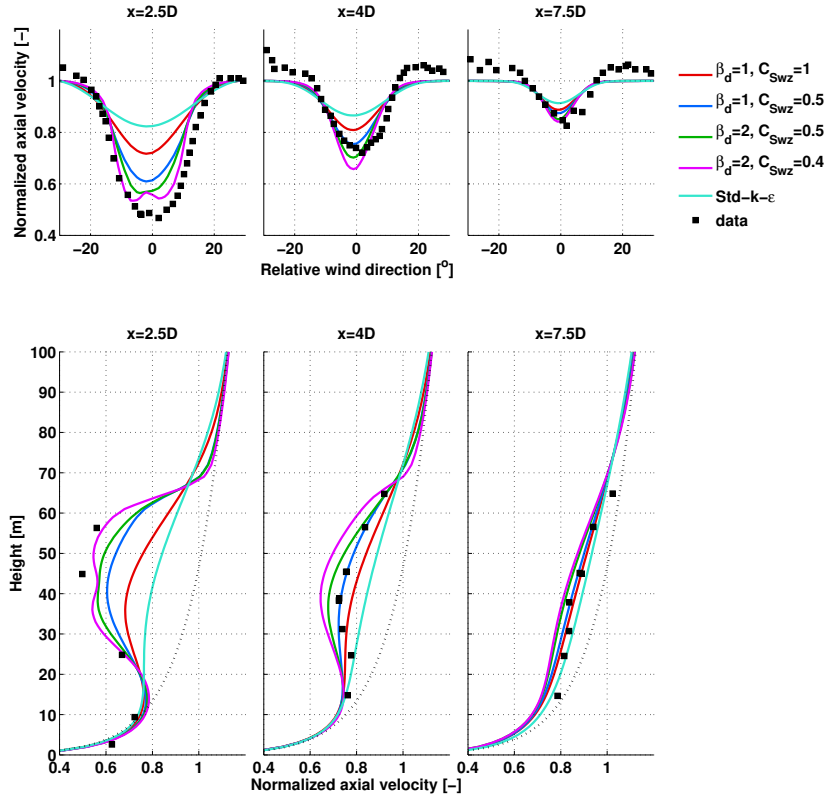
Figure 6.18: Nibe Test Case. Parametric study on the Realizability-Canopy model. Only the k term is considered in the Canopy model ($C_{\varepsilon d} = 0.0$, $\beta_p = 0.0$, $C_{\varepsilon p} = 0.0$). Four different sets of parameters are compared to the standard k-ε model. The axial horizontal and vertical velocity profile is plotted at the position of three met.masts downstream of the wind turbine. The axial velocities are normalized with the hub height inflow velocity. The vertical inflow profile is indicated as a black dot line.

6.4 Discussion

The different methods presented previously are found to perform poorly in comparison to the measurements and the LES.

Cabezon et al. [18] found that the El Kasmi-Masson model could not give the appropriate wake deficit in the case of the Nibe turbine and the Sexbierum wind farm. The results (Fig. 6.14) show that it is possible to obtain an equivalent wake deficit at the first met mast by increasing the parameter. However, the wake does not recover fast enough to present a velocity in agreement with the following masts. A similar result is obtained by Rados et al. [68] on the Nibe turbine data set. They also applied the El Kasmi-Masson model using a k-ω model and obtained a better result on the first two met.mast of the Nibe turbine data set (the results at met.mast $7.5D$ were not presented).

The increase of dissipation introduces a low eddy-viscosity, which remains too low, in the wake, in comparison to the LES (Fig. 6.4c). The consequence is that the Reynolds-stresses are too low and do not recover the wake as fast as they should.

Another issue is that the LES showed that there was nearly no influence of the actuator disc on the dissipation in the region close to the disc (Fig. 6.4d), which is in complete disagreement with what the El Kasmi-Masson model practically does. The findings of Chapter 5, indicate that a model based only on the modification the k and ε cannot give a complete picture of the wake dynamics. Modifying k or ε cannot directly correct the invalid assumptions of the Boussinesq's approximation. By reducing k or increasing ε it is possible to practically reduce the eddy-viscosity locally. However, this can introduce an unphysical error in the two values, which is transported downstream.

It is demonstrated in Section 5.5.5 that there is a reduction of k and of ε in the region close to the rotor disc. However this effect is small in comparison to the error made by the invalid assumptions of the Boussinesq's approximation and is not enough to correct the k-ε model (see the comparison of LES_{VF} and LES_{CF} Fig. 5.6). This is illustrated by the poor performance of the Canopy model applied for the wind turbine. The model reduces k and consequently also the eddy-viscosity. This effect delays the wake recovery, yet not enough in comparison to the LES results (Fig. 6.10).

The adverse pressure gradient and the high nonlinearity of the flow in the wake region are found to be the main source of error in the Boussineq's approximation (see Section 5.5.4). The APG model, which follows the simple approach of reducing the eddy-viscosity in the region surrounding the wind turbine, shows that the axial velocity and turbulence development in this region is in agreement with the trends of the LES model (Fig. 6.6).

This is, however, not enough to correct the flow development after the region of influence of the adverse pressure gradient. As soon as the flow leaves this region and that the eddy-viscosity returns to its original formulation, based on the ratio of the k and ε, the wake dissipates very rapidly. The high nonlinearity of the flow in the wake produces an overestimation of the Reynolds-stresses based on the Boussinesq's approximation.

The Realizability model, which is based on the Schwartz inequalities, has the feature to detect the regions of high nonlinearity and provides a simple solution to limit the eddy-viscosity in those regions. The standard model, which is based on the constant $C_{\mathrm{Swz}} = 1.0$ is enforcing that the Reynolds stresses have a relation that respects the Schwartz inequalities. It provides an upper-limit for the eddy-viscosity, so that the relationship between the Reynolds-stresses is more statistically correct. As the Boussinesq's invalid assumptions produce an overestimation of the Reynolds-stresses in the region of high velocity shear, the Realizability model acts in those region by reducing the eddy-viscosity. The standard model successfully accounts for the adverse pressure gradient area and obtains a performance similar to the APG model. However, the standard model does not give results satisfying enough in comparison to the LES (Fig. 6.8) and the measurements (Fig. 6.16 and Fig. 6.15). A likewise observation was made by Cabezon et al. [18] on the Sexbierum dataset.
Better results can be obtained by applying a parameter to the standard Realizability model to reduce even further the eddy-viscosity. Nonetheless, it is important to note that this is not justifiable theoretically. There is in fact little chances that the value found to fit the measurements is applicable for different types of turbines, inflow conditions, or in multiple wake cases.
The region of action of the wake extends far downstream ($x > 10D$) in the cases of the low parameters. In the case of multiple wakes, which are not presented here, the downstream turbine can be in the region of influence of the first turbine, which can create unrealistic results.

Combining the Canopy model with the Realizability model is justifiable theoretically, as they act on two different issues. However, the Canopy model mainly delays the development of the turbulence development and does not provide a significant difference in comparison to the Realizability model alone.
The comparison with measurements shows that the Realizability model alone obtains closer turbulence values to the Sexbierum Test Case, than the Realizability-Canopy model.
Finally it is important to note that the measurements test cases considered have been done 15–20 years ago. While the measurements have been extensively documented, the original data is not available anymore. Even at Risø-DTU, where the Nibe measurement data analysis took place. The

number of cases to compare with the models are, therefore, limited. Moreover, the measurements were done on small of wind turbines roughly half the size of modern wind turbines. This is a problem because the error caused by the Boussinesq approximation is linked to the eddy-viscosity, which is increasing with height (see Fig. 4.5). In order to fully validate the models, new measurement campaigns are needed on single and multiple large wind turbine wake, with many met.masts downstream and upstream the wind turbine.

6.5   Summary

This chapter presents different models intended to correct the k-ε model in the context of modelling wind turbine wake with atmospheric turbulence. All the models are based on the idea to reduce directly or indirectly the eddy-viscosity. The El Kasmi-Masson model increases the dissipation ε proportionally to the turbulent production. The Realizability model reduces the eddy-viscosity to enforce the Reynolds-stresses to respect the Schwartz inequalities. Finally, the Canopy model acts on both the turbulent kinetic energy and the dissipation in order to account for the extraction of energy from the turbulence by the wind turbine.

A parametric study is carried out for each model and compared to the LES test case of Chapter 5 and the measurements presented in Chapter 4. The El Kasmi-Masson model can to obtain a similar wake deficit to the measurements in the close wake region ($x = 2.5D$). However, the turbulence level is found to be too low in comparison to the measurements. This can partially explain why the wake development is too slow in comparison to the LES results and the measurements farther downstream.

The Realizability model, using a low parameter, gives better results in comparison to the LES and the measurements, both in terms of axial velocity and turbulence intensity. However, it is important to note that the model is only justifiable theoretically for a parameter $C_{\mathrm{Swz}} = 1.0$. Consequently, the parameter found to give the best fit with the measurements is not expected to be necessarily appropriate for different wind turbine kind, or inflow conditions. Especially, the cases of multiple wakes have not been considered in the current study and is expected to presents some issues, as the area of influence of the model can extend to the downstream turbine.

The Canopy model performs best when keeping only the dissipative k term. Its action is however too small to be able to correct the k-ε model. When combined with the Realizability model, the two models produce too little turbulence in the wake in comparison to the measurements.

The modifications of the k-ε model investigated in this chapter were not found to be appropriate to correct the issues presented in Chapter 5. More turbulence modelling efforts are needed to develop a robust steady-state model of wind turbine wakes in atmospheric turbulence.

7

Conclusions

Contents

7.1 Forces Treatment

Chapter 2 presented a method to implement discrete body forces into a finite-volume flow solver with collocated variables. The method avoids the pressure-velocity decoupling that is numerically created by the discretization of the Navier-Stokes Equations. The discrete body forces are redistributed over three successive cells, with a pressure jump term acting at the common faces between the cells. The method is successfully validated with several test cases where analytical solutions are known.

The previous method used in EllipSys was to smooth the discrete forces over several cells using a Gaussian distribution. The current method reduces significantly the number of cells necessary for doing a wind turbine wake computation.

The method is flexible and can be used in all kind of flows where body forces are necessary, e.g. immerse boundary methods, forest and urban canopy, object's drag forces.

7.2 Actuator Disc Method

A generic and flexible method to redistribute shapes of body forces into a finite-volume computational domain is presented in Chapter 3. The method is based on three layers of discretization, the shape discretization, the domain discretization and the intersectional discretization between the two first ones. This formulation is very flexible and lets the shape be distributed in any kind of computational mesh.

The special case of actuator disc model is presented and compared with two different models, an analytical solution for Conway's heavily loaded actuator disc and a full rotor computation in CFD. They are both in very good agreement with the method presented, even with a coarse discretization (10 cells per rotor diameters).

The actuator disc model of Conway has been successfully implemented in MatLab. The solution of the Bessel-Laplace Integrals necessary for the special case of parabolic axial velocity in the wake have been derived and are available in the Appendix B.

7.3 Turbulence Modelling

The standard k-ε model is not adapted to do wind turbine wake computation in atmospheric turbulent flows. This is demonstrated by a comparison to two single wind turbine wake measurements in Chapter 4. A parametric study on the eddy-viscosity in Chapter 4 shows that there is a threshold value under which the error caused by the eddy-viscosity concept is negligible.

A comparison with LES, which can operate under the eddy-viscosity threshold value, gives some insight on where the issues of the k-ε model come from (Chapter 5). The Boussinesq's approximation, which relates the Reynolds-stresses with the local velocity gradients and the eddy-viscosity, is found to be an important contribution to these issues. It is found to be invalidated in the region where the wind turbine applies an adverse pressure gradient to the flow and in the major part of the wake, where the velocity distribution is highly nonlinear over distances related to the turbulent length-scale. This is an important results that shows that wind turbine wake in atmospheric turbulence is outside of the envelop of the k-ε model assumptions.

Moreover, as the wind turbine can adapt its forces to the local velocity changes, it can extract energy from the TKE. The standard k-ε model does not take care of this issue. This assumption is found to have a small, yet significant, influence on the wake characteristics.

Different strategies to modify the k-ε model are investigated in Chapter 6. The El Kasmi-Masson model, which is the only method available in the literature to correct the k-ε model in wind turbine wake cases, is increasing the dissipation proportionally to the production of turbulence. This is found to be in contrast with the trends observed in the LES results.
The Realizability model, based on the same idea of the k-ε Realizable model, gives better results in term of turbulence kinetic energy and dissipation. However, the model is not physical and is not expected to be robust enough to work in all kind wind turbine wake cases without the need to be recalibrated.
Finally, the Wind Turbine Canopy model is presenting an interesting way to account for the turbulence extraction of the wind turbine. However, it does not account for the invalid assumptions of the Boussinesq's approximation, which have a dominant effect on the flow development.

In conclusion, a physical steady-state wind turbine wake model is not yet feasible with any of k-ε model correction investigated. More turbulence modelling efforts are needed to perform steady-state wind turbine wake computation with CFD.

7.4   Measurements

While the measurements analysis is not the main focus of this thesis, an extensive work has been done on analyzing several wind farms data. It is very difficult to obtain statistically representative results out of the wind farm measurements for numerous reasons, which are presented in Appendix C.
The general conclusions are that more wind farm measurements are needed to obtain more robust statistics in order to validate the wake models. More single and multiple wind turbine wake cases are also needed to calibrate the CFD wake models and have to be done for modern types of turbines, offshore as well as onshore, in different types of inflow conditions, of surface roughness lengths and over larger distances.
Moreover, it is very important to be very careful while the measurements are recorded, calibrated, reported and archived, in order to preserve the quality of the measurement and to simplify the data analysis.
Finally, some measurements are needed for the study of the shadow effect of a wind farm on another one. In that context, it is important to be able to study the measurements from wind farms build at close distances, such as, for example, the wind farms located Horns Rev and Nysted in Denmark.

7.5 Future work

The tools developed during this study give the possibility to investigate many different aspects of the wind turbine wake phenomenon and other fluid dynamics problems, such as:

- Comparison of the far wake of an actuator disc and an actuator line model.

- Comparison of multiple wind turbine wakes between LES and k-ε.

- Study of the influence of the tangential forces (i.e. the wake rotation) over the wake development.

- Study of the influence of the inhomogeneous force distribution in contrast with the homogeneous force distribution.

- Study of the applicability of Reynolds stresses transport model, not based on the Boussinesq approximation [98], to wind turbine wake in atmospheric flow.

- Study of non-local turbulent closure models, such as Stull's transilient turbulence model [91], to wind turbine wake in atmospheric flow.

- Comparison of k-ε and LES for forest and urban canopy modelling, following the same approach as Chapter 5.

Bibliography

[1] *IEC 61400-12: Wind-turbine Generator Systems, Part 12:- Wind-turbine Power Performance Testing (2006).*

[2] WAsP - the wind atlas analysis and application program. URL `http://wasp.dk`.

[3] Wind resources at horns rev. Technical Report D-160949, Eltra PSO-2000 Proj. Nr. EG-05 3248, 2000.

[4] J. F. Ainslie. Development of an eddy viscosity model for wind turbine wakes. *EWEA*, 1985.

[5] I. Ammara, C. Leclerc, and C. Masson. A viscous three-dimensional differential/actuator disc method for the analysis of wind farms. *ASME J. Sol. Energy Eng.*, 124(4):345–356, 2002.

[6] R. J. Barthelmie, S. T. Frandsen, L. E. Jensen, M. Mechali, and P.-E. Réthoré. Verification of efficiency model for very large wind turbine clusters. *EOW Conference, Copenhagen*, 2005.

[7] R. J. Barthelmie, S. T. Frandsen, N. M. Nielsen, S. C. Pryor, P.-E. Réthoré, and H. E. Jørgensen. Modelling and measurements of power losses and turbulence intensity in wind turbine wakes at middelgrunden offshore wind farm. *Wind Energy*, 10:217–228, 2007.

[8] R. J. Barthelmie, S. T. Frandsen, P.-E. Réthoré, and L. E. Jensen. Analysis of atmospheric impacts on the development of wind turbine wakes at the nysted wind farm. *EOW Conference, Berlin*, 2007.

[9] R. J. Barthelmie, S. T. Frandsen, P.-E. Réthoré, S. C. Pryor, M. Mechali, L. E. Jensen, and P. Sørensen. Modelling and measurements of offshore wakes. *Offshore Wind Energy in Mediterranean and Other European Seas, Rome*, pages 31–43, 2006.

[10] R. J. Barthelmie, K. Hansen, S. T. Frandsen, O. Rathmann, J. G. Schepers, W. Schlez, J. Phillips, K. Rados, A. Zervos, E. S. Politis, and P. K. Chaviaropoulos. Modelling and measuring flow and wind turbine wakes in large wind farms offshore. *Wind Energy*, (12):431–444, 2009.

[11] A. Bechmann. *Large-Eddy Simulation of Atmospheric Flow over Complex Terrain.* PhD thesis, DTU-MEK, Denmark, 2007.

[12] A. Bechmann and N. N. Sørensen. Hybrid RANS/LES method for wind flow over complex terrain. *Wind Energy*, 2009.

[13] P. S. Bernard, M. A. Asgmawey, and R. A. Handler. An analysis of particle trajectories in computer-simulated turbulent channel flow. *Phys. Fluids*, 1(9), September 1989.

[14] P. S. Bernard and R. A. Handler. Reynolds stress and the physics of turbulent momentum transport. *Journal of Fluid Mechanics*, 220:99–124, 1990.

[15] P. S. Bernard and M. Wallace. *Turbulent Flow*. Wiley, 2002.

[16] M.J. Boussinesq. *Théorie de l'écoulement tourbillonnant et tumultueux des liquides*. Gauthier-Villars et fils, 1897.

[17] T. Burton, D. Sharpe, N. Jenkins, and E. Bossanyi. *Wind Energy Handbook*. Wiley, 2001.

[18] D. Cabezon, J. Sanz, I. Marti, and A. Crespo. CFD modeling of the interaction between the surface boundary layer and rotor wake. comparison of results obtained with different turbulence models and mesh strategies. *EWEC Marseille*, 2009.

[19] G. Castro and A. Gravdahl. CFD wake modeling using a porous disc. *EWEC Brussels*, 2008.

[20] Y. S. Chen and S. W. Kim. Computation of turbulent flow using an extended turbulence closure model. Technical Report NASA CR-179204, NASA Contractor Report, 1987.

[21] M. B. Christiansen. *Wind Energy Applications of Synthetic Aperture Radar*. PhD thesis, Risø-DTU, Roskilde, Denmark, 2006.

[22] J.W. Cleijne. Results of Sexbierum wind farm; single wake measurements. Technical Report 93-082, 112324-22420, TNO-report, 1993.

[23] J. T. Conway. Application of an exact nonlinear actuator disk theory to wind turbines. *ICNPAA 2002, Melbourne, Florida, USA*, 15 -17 May 2002.

[24] J. T. Conway. Analytical solutions for the actuator disc with variable radial distribution of load. *J. Fluid Mech.*, 297:327–355, 1995.

[25] J. T. Conway. Exact actuator disk solutions for non-uniform heavy loading and slipstream contraction. *J. Fluid Mech.*, 356:235–267, 1998.

[26] J. T. Conway. Prediction of the performance of heavily loaded propellers with slipstream contraction. *CASI J.*, 44:169–174, 1998.

[27] J. T. Conway. Analytical solutions for the newtonian gravitational field induced by matter within axissymmetric boundaries. *Mon. Not. R. Astrom. Soc.*, 316:540–554, 2000.

[28] J. T. Conway. Exact solutions for the magnetic fields of axisymmetric solenoids and current distributions. *IEEE Transactions on Magnetics*, 37:2977–2988, 2001.

[29] G. P. Corten and P. Schaak. More power and less loads in wind farms: "heat and flux". *EWEC London*, 2004.

[30] A. Crespo, J. Hernandez, and S.T. Frandsen. Survey of modelling methods for wind turbine wakes and wind farms. *Wind Energy*, (2):1–24, 1999.

[31] A. Crespo, F. Manuel, D. Moreno, E. Fraga, and J. Hernandez. Numerical analysis of wind turbine wakes. *Workshop on Wind Energy Applications, Delphi, Greece*, 1985.

[32] DNV/Risø. *Guidelines for design of wind turbines*, 2nd edition, 2002.

[33] I. Dobrev, F. Massouh, and M. Rapin. Actuator surface hybird model. *Journal of Physics: Conference Series*, 75, 2007.

[34] P. W. Egolf. Difference-quotient turbulence model: A generalization of prandtl's mixing-length theory. *Physical review*, 49(2), Februrary 1994.

[35] A. El Kasmi and C. Masson. An extended $k - \epsilon$ model for turbulent flow through horizontal-axis wind turbines. *J. Wind Eng. Ind. Aerodyn.*, 96:103–122, 2008.

[36] S. T. Frandsen. Turbulence and turbulence-generated structural loading in wind turbine clusters. Technical Report Risø-R-1188(EN), Risø-DTU, Roskilde, Denmark, January 2007.

[37] S. T. Frandsen, R. J. Barthelmie, O. Rathmann, H. E. Jørgensen, J. Badger, K. Hansen, S. Ott, P.-E. Réthoré, S. E. Larsen, and L. E. Jensen. The making of a second-generation wind farm efficiency model-complex. *Wind Energy*, 2009.

[38] S. T. Frandsen, R. J. Barthelmie, O. Rathmann, H. E. Jørgensen, J. Badger, K. Hansen, S. Ott, P.-E. Réthoré, S. E. Larsen, and L. E. Jensen. Summary report: The shadow effect of large wind farms: measurements, data analysis and modelling. Technical Report Risø-R-1615(EN), Risø-DTU, 2009.

[39] S. T. Frandsen, R. J. Barthelmie, O. Rathmann, S. Ott, H. E. Jørgensen, J. Badger, P.-E. Réthoré, S. E. Larsen, and L. E. Jensen. The making of a second generation wind farm efficiency model-complex. *EWEC Brussels*, 2008.

[40] L. Gilling, N. N. Sørensen, and P.-E. Réthoré. Imposing resolved turbulence by an actuator in a detached eddy simulation of an airfoil. *EWEC Marseille*, 2009.

[41] R. Gomez-Elvira, A. Crespo, E. Migoya, F. Manuel, and J. Hernandez. Anisotropy of turbulence in wind turbine wakes. *Anisotropy of turbulence in wind turbine wakes*, 93(10):797–814, October 2005.

[42] M.O.L. Hansen. *Aerodynamics of wind turbines.* James&James, 2000.

[43] J. O. Hinze, R. E. Sonnenberg, and P. J. H. Builtjes. Memory effect in a turbulent boundary-layer flow due to a relatively strong axial variation of the mean-velocity gradient. *Appl. Sci. Res.*, 29, January 1974.

[44] J. Højstrup and M. S. Courtney. Turbulence in wind farms. *EWEC Travemunde*, pages 383–386, 1993.

[45] S. S. A. Ivanell. *Numerical computation of wind turbine wakes.* PhD thesis, Royal Institute of Technology, SE-100 44 Stockholm, Sweden, January 2009.

[46] N. O. Jensen. A note on wind generator interaction. Technical Report M-2411, Risø, Roskilde, Denmark, 1983.

[47] C. Koning. *Aerodynamic theory: A general review of progress - Vol.IV. Division M, Influence of the propeller on other parts of the airplane structure, p.366.* Peter Smith, 1976.

[48] B. Lange, H.-P. Waldl, R. J. Barthelmie, A. G. Gerrero, and D. Heinemann. Modelling of offshore wind turbine wakes with the wind farm program FLaP. *Wind Energy*, 6:87–104, 2003.

[49] G. C. Larsen, H. A. Madsen, F. Bingöl, J. Mann, S. Ott, J. N. Sørensen, V. Okulov, N. Troldborg, M. Nielsen, K. Thomsen, T. J. Larsen, and R. Mikkelsen. Dynamic wake meandering modeling. Technical Report R-1607(EN), Risø-DTU, Roskilde, Denmark, 2007.

[50] B. E. Launder and D. B. Spalding. *Mathematical models of turbulence.* Academic Press, London, 1972.

[51] C. Leclerc and C. Masson. Wind turbine performance predictions using a differential actuator-lifting disk model. *J. Sol. Energy Eng.*, 127(2):200–208, May 2005.

[52] B. P. Leonard. A stable and accurate convective modelling procedure based on quadratic upstream interpolation. *Comp. Meth. in Appl. Mech. and Engrng.*, 19: 59–98, 1979.

[53] P. B. S. Lissaman. Energy effectiveness of arbitrary arrays of wind turbines. *J. Energy*, 3(6):323–328, 1979.

[54] J. L. Lumley. Towards a turbulent constitutive relation. *J. Fluid Mech.*, 41(2): 413–434, 1970.

[55] H. A. Madsen. Application of actuator surface theory on wind turbines. *IEA R&D WECS, Joint action on Aerodynamics of wind turbines, Lyngby, Denmark*, nov 1988.

[56] H. A. Madsen, R. Mikkelsen, S. Øye, C. Bak, and J. Johansen. A detailed investigation of the blade element momentum (BEM) model based on analytical and numerical results and proposal for modifications of the BEM model. *Journal of Physics: Conference Series*, 75, 2007.

[57] J. Mann. *Models in Micrometeorology*. PhD thesis, Risø National Laboratory, Roskilde, Denmark, 1994.

[58] C. Masson, A. Smaili, and C. Leclerc. Aerodynamic analysis of HAWTs operating in unsteady conditions. *J. Wind Energy*, 4:1–22, 2001.

[59] M. Mechali, L. E. Jensen, R. J. Barthelmie, S. T. Frandsen, and P.-E. Réthoré. Wake effects at Horns Rev and their influence on energy production. *EWEC Athens*, 2006.

[60] J. Mencinger and I. Zun. On the finite volume discretization of discontinuous body force field on collocated grid: Application to VOF method. *Journal of Computational Physics*, 221:524–538, 2007.

[61] F. R. Menter. Zonal two equation k- turbulence models for aerodynamic flows. *AIAA Journal*, (93-2906), 1993.

[62] J. A. Michelsen. Basis3D - a platform for development of multiblock PDE solvers. Technical report afm 92-05, Technical University of Denmark, Lyngby, 1992.

[63] R. Mikkelsen. *Actuator Disc Methods Applied to Wind Turbines*. PhD thesis, Technical University of Denmark, Mek dept, 2003.

[64] H. A. Panofsky and J. A. Dutton. *Atmospheric Turbulence Models and Methods for Engineering Applications*. John Wiley & Sons, 1984.

[65] S. V. Patankar and D .B. Spalding. A calculation procedure for heat, mass and momentum transfer in three-dimensional parabolic flows. *Int. J. Heat Mass Transfer*, 15:1787–1972, 1972.

[66] A. Peña, S.-E. Gryning, C. B. Hasager, and M. S. Courtney. Extending the wind profile much higher than the surface layer. *EWEC Marseille*, 2009.

[67] S. B. Pope. *Turbulent Flows*. Cambridge University Press, 2005.

[68] K. G. Rados, J. M. Prospathopoulos, N. Ch. Stefanatos, E. S. Politis, P. K. Chaviaropoulos, and A. Zervos. CFD modeling issues of wind turbine wakes under stable atmospheric conditions. *EWEC Marseille*, 2009.

[69] O. Rathmann, S. T. Frandsen, and R. J. Barthelmie. Wake modelling for intermediate and large wind farms. *EWEC Milano*, 2007.

[70] P.-E. Réthoré, A. Bechmann, N. N. Sørensen, S. T. Frandsen, J. Mann, H. E. Jørgensen, O. Rathmann, and S. E. Larsen. A CFD model of the wake of an offshore wind farm: using a prescribed wake inflow. *Journal of Physics: Conference Series*, 75, 2007.

[71] P.-E. Réthoré, N. A. Johansen, S. T. Frandsen, R. J. Barthelmie, K. Hansen, L. E. Jensen, M. A. B. Bækgaard, and J. R. Kristoffersen. Systematic wind farm measurement data reinforcement tool for wake model calibration. *EOW Conference, Stockholm*, 2009.

[72] P.-E. Réthoré, N. N. Sørensen, A. Bechmann, and F. Zahle. Study of the atmospheric wake turbulence of a CFD actuator disc model. *EWEC Marseille*, 2009.

[73] P.-E. Réthoré and N.N. Sørensen. Modification of a Rhie-Chow/SIMPLE pressure correction algorithm to handle a pressure jump. 3^{rm} *EAWE Semina, CENER, Pamplona, Spain*, 2007.

[74] P.-E. Réthoré and N.N. Sørensen. Actuator disc model using a modified Rhie-Chow/SIMPLE pressure correction algorithm. *EWEC Brussels*, 2008.

[75] C. M. Rhie and W. L. Chow. Numerical study of the turbulent fow past an airfoil with trailing edge separation. *AIAA Journal*, 21:1525–1532, 1983.

[76] B. Sanderse. Aerodynamics of wind turbine wakes - literature review. Technical Report ECN-E–09-016, ECN, Netherlands, 2009.

[77] C. Sanz. A note on $k - \epsilon$ modelling of vegetation canopy air-flows. *Boundary-Layer Meteorology*, 108:191–197, 2003.

[78] A. P. Schaffarczyk and J.T. Conway. Comparison of a nonlinear actuator disk theory with numerical integration including viscous effects. *CASI J.*, 46:209–215, 2000.

[79] J. G. Schepers. Validation and improvement of ECNs wake model. Technical Report ECN-C–03-034, ECN, 2003.

[80] F. G. Schmitt. About Boussinesq's turbulent viscosity hypothesis: historical remarks and a direct evaluation of its validity. *C. R. Mecanique*, 355:617–627, 2007.

[81] U. Schumann. Realizability of Reynolds-stress turbulence models. *The Physics of Fluids*, 20(5), May 1977.

[82] D. J. Sharpe. A general momentum theory applied to an energy-extracting actuator disc. *Wind Energy*, 7:177–188, 2004.

[83] W. Z. Shen, J. H. Zhang, and J. N. Sørensen. The actuator surface model: A new navier–stokes based model for rotor computations. *J. Sol. Energy Eng.*, 131(1), 2009.

[84] T.-H. Shih, J. Zhu, and J. L. Lumley. A new Reynolds stress algebraic equation model. *Comput. Methods Appl. Mech. Engrg.*, 125:287–302, 1995.

[85] C. Sibuet Watters and C. Masson. Modeling of lifting-device aerodynamics using the actuator surface concept. *Int. J. Numer. Meth. Fluids*, 2009.

[86] A. Sogachev. A note on two-equation closure modelling of canopy. *Boundary-Layer Meteorology*, 130:423–435, 2009.

[87] A. Sogachev and O. Panferov. Modification of two-equation models to account for plant drag. *Boundary-Layer Meteorology*, 121:229–266, 2006.

[88] J. N. Sørensen and W. Z. Shen. Numerical modelling of wind turbine wakes. *Journal of Fluids Engineering*, 124(2):393–399, 2002.

[89] N. N. Sørensen. *General Purpose Flow Solver Applied to Flow over Hills.* PhD thesis, Technical University of Denmark, 1994.

[90] N. N. Sørensen and J. Johansen. UPWIND, aerodynamics and aero-elasticity rotor aerodynamics in atmospheric shear flow. *EWEC Milano*, 2007.

[91] R. B. Stull. *An Introduction to Boundary Layer Meteorology.* Kluwer Academic Publishers, Amsterdam, 1988.

[92] D. B. Taulbee. An improved algebraic Reynolds-stress model and corresponding nonlinear stress model. *Phys. Fluids*, 1992.

[93] S. Tavoularis and S. Corrsin. Experiments in nearly homogeneous turbulent shear flow with a uniform mean temperature gradient. part1-2. *J. Fluid Mech.*, 104:311–367, 1981.

[94] G. J. Taylor. Wake measurements on the Nibe wind turbines in Denmark. Technical Report ETSU WN 5020, National Power, 1990.

[95] H. Tennekes and J. L. Lumley. *A first course in Turbulence.* MIT Press, Cambridge, MA, 1972. Chap 2.

[96] N. Troldborg. *Actuator Line Modeling of Wind Turbine Wakes.* PhD thesis, DTU-MEK, Denmark, 2008.

[97] L. J. Vermeer, J. N. Sørensen, and A. Crespo. Wind turbine wake aerodynamics. *Progress in Aerospace Sciences*, 39:467–510, 2003.

[98] D. C. Wilcox. *Turbulence modeling in CFD.* DCW, 2006.

[99] J. W. Wrench. Review of: Heuman lambda function. *Mathematics of Computation*, 20:627–628, 1966.

[100] F. Zahle. *Wind Turbine Aerodynamics Using an Incompressible Overset Grid Method.* PhD thesis, Imperial College, London, 2007.

[101] F. Zahle and N.N. Sørensen. Characterisation of the unsteady flow in the nacelle region of a modern wind turbine. *EWEC Marseille*, 2009.

A

Description of EllipSys

A.1 Introduction

EllipSys [89, 62], is a flow solver based on a finite-volume spatial and temporal discretization of the incompressible Navier-Stokes Equations formulated in general curvilinear coordinates. The variables are colocated in the cell centers to enable computations using complex geometrical meshes. The SIMPLE method is used to solve the Navier-Stokes Equations system (Patankar and Spalding [65]). The pressure correction method is based on the Rhie-Chow algorithm [75] and is accelerated using a multigrid technique [62]. The flow is solved successively over three levels of discretization in order to accelerate the convergence and to ensure a grid independent solution. The equations can be discretized using different schemes. In the present report the high order QUICK scheme (Leonard [52]) is used in all the simulations. The method is based on a multiblock framework [62] which gives the possibility to decompose the mesh and solve it on different processors.

In the following sections, the main constitutive equations are expressed in Cartesian coordinate, using the Einstein summation rule.

A.2 Navier-Stokes Equations

The incompressible Navier-Stokes Equations are composed of the Continuity Equation,

$$\frac{\partial U_i}{\partial x_i} = 0, \tag{A.1}$$

where U_i is the velocity vector and the Momentum Equations,

$$\frac{\partial U_i}{\partial t} + \frac{\partial U_i U_j}{\partial x_j} = -\frac{1}{\rho}\frac{\partial P}{\partial x_i} + 2\frac{\partial \nu S_{ij}}{\partial x_j}, \tag{A.2}$$

where P is the pressure, ρ is the density, ν is the kinematic molecular viscosity and S_{ij}, is the strain-rate tensor, defined as

$$S_{ij} = \frac{1}{2}\left(\frac{\partial U_i}{\partial x_j} + \frac{\partial U_j}{\partial x_i}\right). \tag{A.3}$$

A.3 Reynolds-averaged Navier-Stokes

Reynolds-averaged Navier-Stokes Equations

Each variable can be time-averaged using the following rule

$$\overline{\Omega}(\mathbf{x}) = \lim_{T\to\infty}\frac{1}{2T}\int_{-T}^{T}\Omega(\mathbf{x},t)\,\mathrm{d}t, \tag{A.4}$$

where $\Omega(\mathbf{x},t)$ is a dummy variable at the position $\mathbf{x}$ and the time t. Each variable can be decomposed with a time-averaged part and a fluctuation part,

$$\Omega(\mathbf{x},t) = \overline{\Omega}(\mathbf{x}) + \omega'(\mathbf{x},t). \tag{A.5}$$

The Reynolds-averaged Navier-Stokes (RANS) Equations are derived applying Eq. (A.4) and Eq. (A.5) to Eq. (A.1) and Eq. (A.2),

$$\frac{\partial \overline{U}_i}{\partial x_i} = 0, \tag{A.6}$$

$$\frac{\partial \overline{U}_i}{\partial t} + \frac{\partial \overline{U}_i\overline{U}_j}{\partial x_j} = -\frac{1}{\rho}\frac{\partial \overline{P}}{\partial x_i} + \frac{\partial}{\partial x_j}\left[2\nu\overline{S}_{ij} - \overline{u_i'u_j'}\right], \tag{A.7}$$

with $\overline{S}_{ij}$ is derived as

$$\overline{S}_{ij} = \frac{1}{2}\left(\frac{\partial \overline{U}_i}{\partial x_j} + \frac{\partial \overline{U}_j}{\partial x_i}\right). \tag{A.8}$$

Reynolds-stresses Tensor

The Reynolds-stresses tensor is defined as

$$R_{ij} = \overline{u_i'u_j'}. \tag{A.9}$$

Turbulence Kinetic Energy

The Turbulent Kinetic Energy (TKE), k, is defined as the trace of the Reynolds-stress tensor:

$$k = \frac{1}{2}R_{ii}. \tag{A.10}$$

Eddy-viscosity Concept / Boussinesq's Approximation

According to the eddy-viscosity concept, the Reynolds-stresses are defined as

$$R_{ij} = \frac{2}{3}k\delta_{ij} - 2\nu_t\overline{S}_{ij}, \tag{A.11}$$

where ν_t is the kinematic eddy-viscosity and δ_{ij} is Kronecker's function. The k term is in practice absorbed in the pressure term in EllipSys (see Sørensen [89]).

A.3.1 Eddy-viscosity / Kinematic eddy-viscosity

The eddy-viscosity μ_t is the kinematic eddy-viscosity ν_t multiplied by the density ρ,

$$\mu_t = \rho\nu_t \tag{A.12}$$

A.4 k-ε Model

Eddy-viscosity

In the k-ε model, the eddy-viscosity is defined as

$$\nu_t = C_\mu \frac{k^2}{\varepsilon}. \tag{A.13}$$

The turbulent length-scale ℓ is defined as

$$\ell = \frac{k^{3/2}}{\varepsilon}. \tag{A.14}$$

$$\nu_t = C_\mu \ell \sqrt{k}. \tag{A.15}$$

Turbulence Kinetic Energy k-equation

The TKE equation is given as,

$$\frac{\partial k}{\partial t} + U_j \frac{\partial k}{\partial x_j} = -R_{ij}\frac{\partial U_i}{\partial x_j} + \frac{\partial}{\partial x_j}\left[\left(\nu + \frac{\nu_t}{\sigma_k}\right)\frac{\partial k}{\partial x_j}\right] - \varepsilon, \tag{A.16}$$

where σ_k is a model constant given in Table A.1.

Dissipation ε-equation

The dissipation equation is given as,

$$\frac{\partial \varepsilon}{\partial t} + U_j \frac{\partial \varepsilon}{\partial x_j} = -C_{\varepsilon 1} \frac{\varepsilon}{k} R_{ij} \frac{\partial U_i}{\partial x_j} - C_{\varepsilon 2} \frac{\varepsilon^2}{k} + \frac{\partial}{\partial x_j} \left[\left(\nu + \frac{\nu_t}{\sigma_\varepsilon} \right) \frac{\partial \varepsilon}{\partial x_j} \right], \quad (A.17)$$

where σ_ε, $C_{\varepsilon 1}$ and $C_{\varepsilon 2}$ are model constants given in Table A.1.

Neutral Boundary Layer Values

The main direction mean wind speed profile follows the log-law,

$$U = \frac{u^*}{\kappa} \ln \left(\frac{z}{z_0} \right), \quad (A.18)$$

where κ is the von Kármán constant, z_0 is the surface roughness length and u^* is the friction velocity.
The TKE k, the dissipation ε, the length-scale ℓ and the kinematic eddy-viscosity ν_t are found as,

$$k = \frac{u^{*2}}{\sqrt{C_\mu}}, \quad (A.19)$$

$$\varepsilon = \frac{u^{*3}}{\kappa z}, \quad (A.20)$$

$$\ell = \frac{\kappa z}{C_\mu^{3/4}}, \quad (A.21)$$

$$\nu_t = \kappa z u^*. \quad (A.22)$$

Model constants

Table A.1: k-ε model constants for atmospheric flows [89].

κ	C_μ	σ_k	σ_ε	$C_{\varepsilon 1}$	$C_{\varepsilon 2}$
0.40	0.03	1.00	1.30	1.21	1.92

The model constants are given in Table A.1. The parameter C_μ can be used to adapt the TKE level. In that case, the parameter $C_{\epsilon 1}$ is modified as

$$C_{\epsilon 1} = C_{\epsilon 2} - \frac{\kappa}{C_\mu^{1/2} \sigma_\epsilon}. \quad (A.23)$$

A.5   Hybrid LES-k-ε Model

The following equations are found in Bechmann [11, 12].

The LES turbulent length-scale is given as,

$$\ell_{LES} = C_\Delta \Delta, \tag{A.24}$$

where C_Δ is a model constant (Table A.2) and the mesh maximum cell size Δ is found as,

$$\Delta = \max\left(\Delta x, \Delta y, \Delta z\right). \tag{A.25}$$

The hybrid LES-k-ε model switches between LES and RANS according to the length-scale value,

$$\ell = \min\left(\frac{k^{3/2}}{\varepsilon}, C_\Delta \Delta\right). \tag{A.26}$$

In the LES region, k and ε are still solved using the k-ε model. However, the dissipation term in the k-equation is modelled directly using the k and ℓ,

$$\frac{\partial k}{\partial t} + U_j \frac{\partial k}{\partial x_j} = -R_{ij} \frac{\partial U_i}{\partial x_j} + \frac{\partial}{\partial x_j}\left[\left(\nu + \frac{\nu_t}{\sigma_k}\right)\frac{\partial k}{\partial x_j}\right] - \frac{k^{3/2}}{\ell}. \tag{A.27}$$

The eddy-viscosity is still found using k and ε and Eq. (A.13). When the k and ε are in balance, the eddy-viscosity can be approximated to a Smagorinsky model,

$$\nu_t = (\Delta C_s)^2 |\overline{S}|, \tag{A.28}$$

where C_s is a model constant (Table A.2) and $\overline{S}$ is the local strain rate defined by $\overline{S} = (2\overline{S_{ij}S_{ij}})^{1/2}$.

Neutral Boundary Layer Values

In neutrally stratified atmospheric flows, the strain rate is approximately

$$|S| = \left|\frac{u*}{\kappa z}\right|. \tag{A.29}$$

The eddy-viscosity can, therefore, be approximated to

$$\nu_t = (\Delta C_s)^2 \frac{u*}{\kappa z}. \tag{A.30}$$

Model Constants

The model constants used in the present work are presented in Table A.2.

Table A.2: k-ε model constants for atmospheric flows (for more details, see Bechmann [11]).

κ	C_μ	σ_k	σ_ε	$C_{\varepsilon1}$	$C_{\varepsilon2}$	C_Δ	C_s
0.40	0.03	1.00	1.30	1.21	1.92	1.26	0.144

Resolved Turbulent Kinetic Energy

The resolved TKE is the trace of the resolved Reynolds-stresses

$$k = \frac{1}{2}\overline{u_i' u_i'}. \tag{A.31}$$

Resolved Dissipation

The resolved dissipation ε is found by taking the time-average of the following expression

$$\varepsilon = \nu \overline{\frac{\partial u_i'}{\partial x_k} \frac{\partial u_i'}{\partial x_k}}. \tag{A.32}$$

B

Bessel-Laplace Integrals

Conway [24, 27] has developed a recursive method to express the Bessel-Laplace integrals (BLI) of type $I_{(\lambda,\mu,\nu)}$ Eq. (3.6) using elliptic integral function to derive a numerical solution.

In order to solve the parabolic wake case, only three basic BLIs are needed ($I_{(-1,2,1)}$, $I_{(0,2,0)}$ and $I_{(0,2,1)}$). While the analytical expression of $I_{(-1,2,1)}$ is given in [28], the analytical expression of $I_{(0,2,0)}$ and $I_{(0,2,1)}$ could not be found in the literature. The recursive method is therefore used to derive them. The algorithm used to implement this method is briefly summarized in the following.

First of all, it is interesting to notice the symmetrical property of the Bessel-Laplace integrals [27],

$$I_{(\lambda,\mu,\nu)}(R,r,z) = I_{(\lambda,\nu,\mu)}(r,R,z). \tag{B.1}$$

Furthermore, the Bessel-Laplace integrals can be related to each other through recursive relations and some initial start formulae. The recursive relations are given as [27],

$$I_{(0,\nu,\nu)} = \frac{4(\nu-1)\omega}{2\nu-1}I_{(0,\nu-1,\nu-1)} - \frac{2\nu-3}{2\nu-1}I_{(0,\nu-2,\nu-2)}, \tag{B.2}$$

$$I_{(1,\nu,\nu)} = \frac{(2\nu-1)|z|k^4}{8Rr(1-k^2)}\left(I_{(0,\nu-1,\nu-1)} - \omega I_{(0,\nu,\nu)}\right), \tag{B.3}$$

$$I_{(0,\nu+1,\nu)} = \frac{r}{R}I_{(0,\nu,\nu-1)} + \frac{r}{2\nu}\left(I_{(1,\nu+1,\nu+1)} - I_{(1,\nu-1,\nu-1)}\right), \tag{B.4}$$

which is only valid for $\nu \neq 0$,

$$\begin{aligned}
I_{(0,\mu,\nu)} = {} & \frac{2(\nu+1)|z|}{r(\nu+1-\mu)}I_{(0,\mu,\nu+1)} - \frac{2(\nu+1)R}{r(\nu+1-\mu)}I_{(0,\mu-1,\nu+1)} \\
& + \frac{(\nu+1+\mu)}{(\nu+1-\mu)}I_{(0,\mu,\nu+2)},
\end{aligned} \tag{B.5}$$

and

$$I_{(\lambda,\mu,\nu)} = \frac{R}{2\mu} \left(I_{(\lambda+1,\mu+1,\nu)} - I_{(\lambda+1,\mu-1,\nu)} \right), \tag{B.6}$$

which is only valid for $\lambda < 0$ and where $\omega = (R^2 + r^2 + z^2)/(2rR)$ is the parameter of an associated Legendre function and $k = \sqrt{4rR/[(R+r)^2 + z^2]}$ is the modulus of an elliptic integral.

The initial start formulae are $I_{(0,0,0)}$, $I_{(0,1,0)}$ and $I_{(0,1,1)}$ and can be found in [28],

$$I_{(0,0,0)}(R,r,z) = \frac{k\mathbf{K}(k)}{\pi\sqrt{rR}}. \tag{B.7}$$

$$I_{(0,1,0)}(R,r,z) = \frac{1}{R} \left[1 - \frac{|z|k\mathbf{K}(k)}{2\pi\sqrt{rR}} - \frac{\Lambda_0(|\beta|,k)}{2} \right] \quad (r < R),$$

$$= \frac{1}{R} \left[-\frac{|z|k\mathbf{K}(k)}{2\pi\sqrt{rR}} + \frac{\Lambda_0(|\beta|,k)}{2} \right] \quad (r > R), \tag{B.8}$$

$$I_{(0,1,1)}(R,r,z) = \frac{(2-k^2)\mathbf{K}(k) - 2\mathbf{E}(k)}{\pi k\sqrt{rR}} \tag{B.9}$$

where $\beta = \arcsin(|z|/\sqrt{(|z|-R)^2 + z^2})$ is the Jacobi amplitude, $\mathbf{K}(k)$ is the complete elliptic integral function of the first kind, $\mathbf{E}(k)$ is the complete elliptic integral function of the second kind and $\Lambda_0(\beta, k)$ is Heuman's Lambda function defined as [27, 99],

$$\Lambda_0(\beta, k) = \frac{2}{\pi} \left[\mathbf{E}(k)F(\beta, k') + \mathbf{K}(k)\Big(E(\beta, k') - F(\beta, k') \Big) \right], \tag{B.10}$$

where $k' = \sqrt{1-k^2}$ is the complementary modulus for an elliptic integral of modulus k.

Using the recursive laws and the start formulae, it is possible to create a recursive algorithm to express any Bessel-Laplace integral in terms of elliptic integral functions. The procedure suggested is to first use the relation $I_{(\lambda,\mu,\nu)}$ Eq. (B.6) to find an expression where $\lambda = 0$. Then use relation $I_{(0,\mu,\nu)}$ Eq. (B.5) to reduce the gap between μ and ν in order to use the relation $I_{(0,\nu+1,\nu)}$ Eq. (B.4) and finally $I_{(0,\nu,\nu)}$ Eq. (B.2). Whenever possible, a shortcut in the recursion can be taken, using the symmetrical relation Eq. (B.1). This procedure is only valid for $\lambda \leq 0$, yet this encompasses all the cases described by Conway's actuator disc model.

In order to test the algorithm, one can compare to some of the Bessel-Laplace integral solutions given in [28].

Using this algorithm it is possible to express $I_{(-1,2,1)}$, $I_{(0,2,0)}$ and $I_{(0,2,1)}$ with respect to elliptic integral functions. $I_{(-1,2,1)}$ is also given in [28],

$$
\begin{aligned}
I_{(-1,2,1)}(R, r, |z|) &= \mathbf{E}(k)\Theta^E_{(-1,2,1)} + \mathbf{K}(k)\Theta^K_{(-1,2,1)} \\
&\quad + \frac{r}{R^2}\left(\frac{z\Lambda_0(\beta, k)}{2} - |z|\right) \quad (r < R), \\
&= \mathbf{E}(k)\Theta^E_{(-1,2,1)} + \mathbf{K}(k)\Theta^K_{(-1,2,1)} \\
&\quad + \frac{rz}{2R^2}\Lambda_0(\beta, k) \quad (r > R),
\end{aligned}
\tag{B.11}
$$

where the coefficients $\Theta^E_{(-1,2,1)}$ and $\Theta^K_{(-1,2,1)}$ are given as,

$$
\Theta^E_{(-1,2,1)} = \frac{1}{k}\frac{1}{2\pi}\sqrt{\frac{r}{R}}\left[\frac{4r}{R} - \frac{8(2-k^2)}{3k^2}\right],
\tag{B.12}
$$

$$
\Theta^K_{(-1,2,1)} = \frac{k}{2\pi}\sqrt{\frac{r}{R}}\left[\frac{(4-k^2)(4-3k^2)}{3k^4} - \frac{r^2}{R^2}\right].
\tag{B.13}
$$

$I_{(0,2,0)}$ is found using the recursive rules,

$$
\begin{aligned}
I_{(0,2,0)}(R, r, |z|) &= \frac{1}{k^3\pi(rR)^{5/2}}\left[\mathbf{E}(k)\Theta^E_{(0,2,0)} + \mathbf{K}(k)\Theta^K_{(0,2,0)}\right] \\
&\quad - \frac{\Lambda_0(\beta, k)|z|}{R^2} \quad (r > R), \\
&= \frac{1}{k^3\pi(rR)^{5/2}}\left[\mathbf{E}(k)\Theta^E_{(0,2,0)} + \mathbf{K}(k)\Theta^K_{(0,2,0)}\right] \\
&\quad + \frac{\left[\Lambda_0(\beta, k) - 2\right]|z|}{R^2} \quad (r < R),
\end{aligned}
\tag{B.14}
$$

where the coefficients $\Theta^E_{(0,2,0)}$ and $\Theta^K_{(0,2,0)}$ are found as Eq. (B.15) and Eq. (B.16).

$$
\Theta^E_{(0,2,0)} = -4rR\left[R\left(2\left(-2+k^2\right)r + k^2R\right) + k^2|z|^2\right],
\tag{B.15}
$$

$$
\begin{aligned}
\Theta^K_{(0,2,0)} &= rR^2\Big[\left(-16 + 16k^2 - 3k^4\right)r - 2k^2\left(-2+k^2\right)R\Big] \\
&\quad + r\Big[k^4(r-2R) + 4k^2R\Big]|z|^2.
\end{aligned}
\tag{B.16}
$$

$I_{(0,2,1)}$ is also found using the recursive rules,

$$
\begin{aligned}
I_{(0,2,1)}(R, r, |z|) &= \mathbf{E}(k)\Theta^E_{(0,2,1)} + \mathbf{K}(k)\Theta^K_{(0,2,1)} \\
&\quad + \frac{\Lambda_0(\beta, k)r}{2R^2} \quad (r > R), \\
&= \mathbf{E}(k)\Theta^E_{(0,2,1)} + \mathbf{K}(k)\Theta^K_{(0,2,1)} \\
&\quad + \frac{\left[2 - \Lambda_0(\beta, k)\right]r}{2R^2} \quad (r < R),
\end{aligned}
\tag{B.17}
$$

where the coefficients $\Theta^E_{(0,2,1)}$ and $\Theta^K_{(0,2,1)}$ are given as,

$$\Theta^E_{(0,2,1)} = \frac{2|z|}{k\pi R\sqrt{rR}}, \tag{B.18}$$

$$\Theta^K_{(0,2,1)} = -\frac{|z|\left(k^2(r-2R)-4R\right)}{2k\pi R^2\sqrt{rR}}. \tag{B.19}$$

Systematic Wind Farm Measurement Data Reinforcement Tool for Wake Model Calibration

Pierre-Elouan Réthoré[1,2,*]**, Nick A. Johansen**[1]**, Sten T. Frandsen**[1]**,**
Rebecca Barthelmie[3] **Kurt S. Hansen**[4]**, Leo E. Jensen**[5]**, Mikkel**
A.B. Bækgaard[5]**, Jesper R. Kristoffersen**[6]

[1] Wind Energy Department, Risø National Laboratory for Sustainable Energy, DTU - Technical University of Denmark, DK-4000 Roskilde, Denmark
[2] Department of Civil Engineering, Aalborg University, Sohngaardsholmsvej 57, DK-9000 Aalborg, Denmark
[3] Department of Geography, Indiana University, Bloomington, USA
[4] Department of Fluid Mechanics, DTU, Lyngby, Denmark
[5] DONG Energy, Denmark
[6] Vattenfall, Denmark
* pire@risoe.dtu.dk

Abstract

Wind farm wake data analysis is a complex process that requires filtering over many different types of sensors located at different geographical positions. The complexity of the task is increased by the different types of data corruption that can be present. Unfortunately, dealing with wind farm data corruption has rarely been addressed in the literature.

This chapter presents different methods intended to reinforce a wind farm dataset. These methods have been applied on several onshore and offshore wind farms.

C.1 Introduction

Wind farm wake data analysis requires wind information from meteorological (met.) masts inside and outside wind farms as well as the wind turbines status. This type of data gives invaluable information to inspire and validate the development of wake models. However, such a dataset are very complex and composed of hundreds of sensors. The first step of a successful data analysis is to make sure that the data by itself is free of corruption. The term data corruption used here is broad and refers to all the cases where the data values are not equal to what they are intended to represent. This corruption can come from various origins (e.g. sensor incorrectly mounted, measuring device incorrectly calibrated, data conversion errors, sensor failure, obstacles on the wind path, unexpected external conditions).
With the number of wind farms and their respective size increasing, the amount of sensor measurements in databases rapidly increases. Consequently, the probability of occurrence of sensor failures or sensor drifting offsets that affect the end goal of the data analysis is also considerably increased. While a preventive methodology designed to mitigate these types of problems is necessary, it is interesting to have as well, robust methods that systematically detect, exclude or correct these events.

While extensive work has been carried out on wind turbine data analysis methods (the IEC 61400 standards series [1]), the source of documentation concerning specifically wind farm data analysis is relatively scarce (Barthelmie [10]). There are no clear guidelines concerning the data corruption that arises when combining several types of sensors located sometimes at several kilometers from each other. In order to mitigate this need, we propose a set of methods to reinforce a wind farm dataset. The methods are based on general knowledge on wind turbine (DNV/Risø guidelines [32], the Wind Energy Handbook [17]) and the practical wind farm data analysis experience accumulated over several years.

The methods presented are divided into 3 sections. The first section is a recommendation concerning the organisation of the data structure. The second section deals with the calibration of sensors using neighbouring sensors. The last section deals with sensor failure detection and correction.

C.2   Methods

C.2.1   Organizing the Data Structure

Description

A large part of the sensor failure arises human error. And in that part, the data analyst carries a large responsibility. For this reason, it is important to have a data structure that is designed so that mistakes can be spotted and recovered easily. The first generation databases contains the original data supplemented with an individual signal quality parameter. We propose to extend this data structure in order to include the different types of errors detected in the data we investigated.

In order to assess the sensor quality, some neighbouring sensors are generally used. It is important to document as well, which sensors are associated to a quality check.

Many types of sensors can be subject to time-drifting gain and/or offset. When those values have been determined, they should be stored independently of the raw data.

Similarly, the signals from sensors can be recorded on different monitoring devices, which potentially have incorrect or incompatible time and date stamps. So ideally there should also be a way to store the time offset value independently from the raw data.

Eventually, the sensor itself can have a failure or the data can be corrupted numerically. In this case, the raw data itself does not represent any valuable information, yet an alternative way to estimate its measurement can potentially be derived using neighbouring sensors. There should also be a way to store this estimation as well as the reference to the method used and the sensors used in that process.

Proposed Data Structure

- Date & Time and period (e.g. 1-minute, 2-minute, 10-minute)

- Raw data (Mean, Maximum, Minimum, Standard deviation)

- Quality code (with sensors associated)

- Mean gain & offset (when available)

- Time offset

- Corrected data (Mean, Maximum, Minimum, Standard deviation)

- Methods used for correction (with sensors associated)

Storing all this added information increases dramatically the amount information, which represents a significant storing cost. However, having access to all this information is recommended for the long term. It is often seen that, after some time, the engineer responsible for the setting up the database and doing the preprocessing work is no longer available. If the data processing has not been documented both inside the database and on a reference report, the end user is left to guess what has been done and faced with the extra work to correct data errors.

C.2.2 Sensor Calibration

Wind Direction Offsets

A wind farm database has generally many accurate wind direction sensors available. However, it is often seen that some of the sensors have not been calibrated properly and operate with a biased offset with respect to the standard wind direction definition. When a reference wind direction is available on site and is believed to be properly calibrated, all the wind direction sensor offsets can be adjusted using the reference sensor.
One particular issue to be aware of during this process is the wind direction dependency to height due to the Coriolis forces. It is important to take this into account when deriving the sensor offset.
Moreover chances are that the offset in wind direction is time dependent. This can come, for example, from a maintenance operation that affected the sensor calibration.

The method proposed to determine a wind direction offset using a reference wind direction is based on a sliding time-window smoothing technique. The difference between the two sensors is plotted with respect to time.
If the difference is noisy, a large time-window is first chosen (typically a week, or a month) to obtain a general idea of the trend of the offset. If an offset jump is spotted during this process, the region of the jump is scanned recursively using a reduced time-window at each step, until an estimate of the offset jump amplitude and the time stamp is determined.
Fig. C.1 illustrates a very large yaw offset jump between two close turbines.
Estimating a robust reference wind direction can be difficult, especially in offshore context where access to the site is limited. Several types of information can contribute to determining the offset of a wind direction sensor. For a wind turbine yaw sensor, the wind turbine power production and geographical location can potentially provide a way to determine an offset. This can be done by calculating the mean power ratio of two aligned turbines, with the first turbine having a free stream wind direction. If the turbines are relatively close (e.g. between 2 and 10 rotor diameters), a distinct power deficit caused by the wake of the first turbine on the second one can be
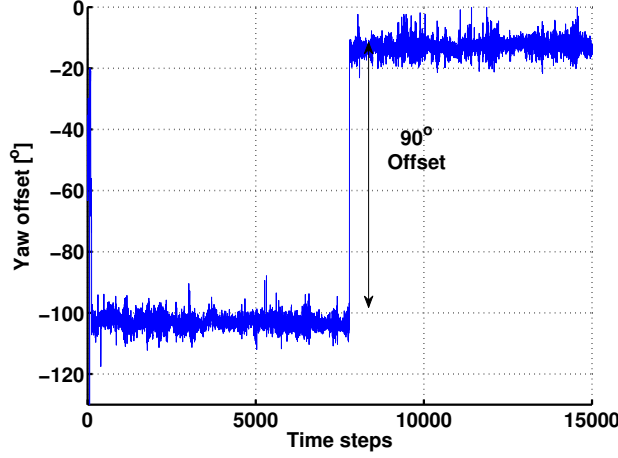
APPENDIX C. WIND FARM DATA REINFORCEMENT TOOL

Figure C.1: Yaw difference between two close wind turbines.

measured at wind speed corresponding to high C_T (e.g. 5–10 m/s). It is possible to estimate with a few degrees accuracy the yaw sensor offset by running an average smoothing algorithm or fitting a Gaussian distribution. In order to avoid missing time dependent offsets, this process can be carried out on a sliding time window.

For a met.mast, the same procedure as for the yaw sensors can be used, if some wind turbines are located at a relatively short distance to the met.mast. Fig. C.2 illustrates this method by comparing the wind direction sensor of a met.mast to the power ratio of two close turbines on the edge of the wind farm (on the first and second row) aligned in the direction of the free stream wind speed.
Note that if the met.mast is located in close periphery of the wind farm, there might be some park effects affecting the local wind speed and direction (e.g. blockage effect). This method might then give an offset dependent with wind direction.

If the mast schematics are available, the position of the sensors on the mast can also provide a way to determine the wind direction offset. The idea is to use a wind speed measurement sensor (e.g. cup anemometer, sonic anemometer) that is not placed on top of the met.mast, to determine the offset of a wind vane on the same mast. The method is to plot the turbulence intensity for different wind speed bins, with respect to the wind direction. This plot should present a peak in the direction angle corresponding to the shadow of the met.mast seen by the anemometer.
In order to spot a potential dependency of the offset with time, this method
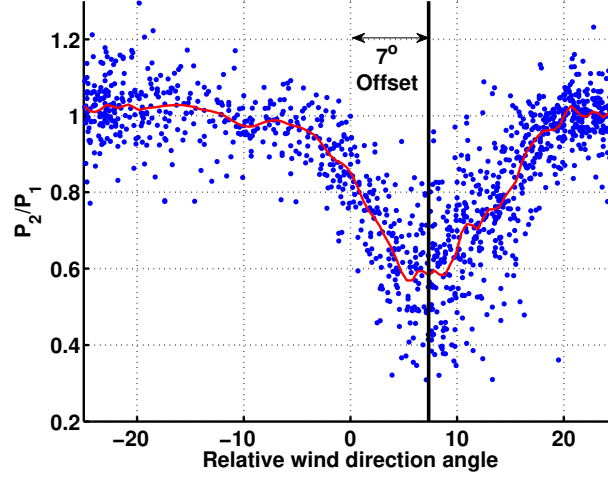
Figure C.2: Power difference between two close wind turbines compared to a neighbouring met.mast wind vane. The wind direction is centered on the wind turbines alignement direction angle.

should be applied over a sliding time window. Fig. C.3 illustrates a small dependency of the offset with time that was observed on an offshore met.mast. There are 3 visibly distinct peak angle locations over time, where the offset jump is between 2 and 4 degrees.

As mentioned previously, the relative height between the two sensors is an important parameter, since the wind direction is expected to be height dependent.

In this method, one has to be careful not to mistake the wind farm added turbulence intensity with the met.mast shadow turbulence intensity.

Time Offsets

Time offsets generally occur when measurement from several different recording devices are gathered in the same database. If the recording devices were not synchronized to the same time and the time offsets were not corrected during the gathering process, the resulting database is unusable. It can sometimes be a rather small time offset (e.g. a few hours) which can be difficult to detect, yet large enough to corrupt the data analysis.

In order to determine precisely the time offset, we propose to use the time correlation between two similar neighbouring sensors located on different recording devices. The time correlation function indicates how the two sensors are correlated with respect to the time offset. If the two sensors
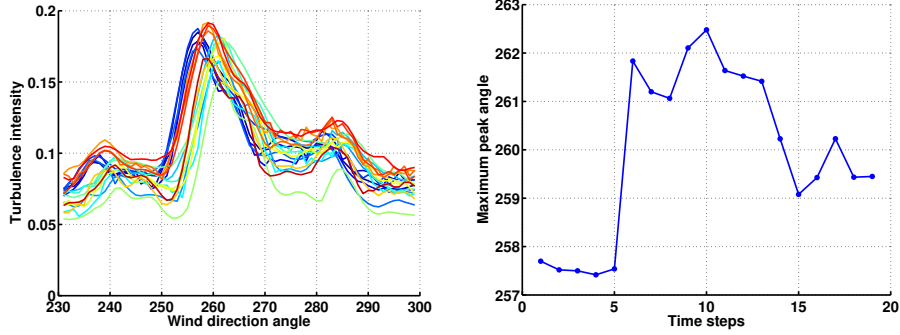
(a) Turbulence intensity versus the wind direction measured on a met.mast at different time periods. The peak corresponds to the shadow angle of the tower.

(b) Time history of the maximum turbulence intensity peak angle location

Figure C.3: Illustration of a small time drifting wind vane offset on an offshore met.mast.

are next to each other and synchronized to the same time, the correlation function has a maximum peak at 0 seconds. If there is a time offset, it is indicated by the maximum peak location. As this time offset can also be time dependent, it is necessary to do a sliding time-window analysis in the same fashion described in the previous section.

Fig. C.4 shows a time offset between a nacelle anemometer and a met.mast anemometer. The two sensor data were originally recorded on two different systems and gathered manually every month. During one month an offset of 50–60 minutes was apparently introduced by a careless operation.

Note that the time correlation is related to the distance between the two sensors and the wind speed. As most of the relevant information are convected by the wind, if the sensors are located far apart and/or the wind speed is small, it might be that the time for the information to reach the second sensor is greater than the 10-minute averaging time window. In that sense, an offset found to be under 20 minutes in a wind farm has to be treated with caution. In Fig. C.4, the time offset has a precision of 10 minutes and oscillates between 0–10 minutes in the first part. As the two sensors where located far apart, it is expected that their relative time offset should be between 0–10 minutes.

C.2.3 Sensor Failure

The type of sensor failure of interest here is when a sensor is producing a value, which is unexpected from the values of other related neighbouring sensors. The idea is that each sensor should be related to some neighbouring sensors through a specific model within a degree of uncertainty.
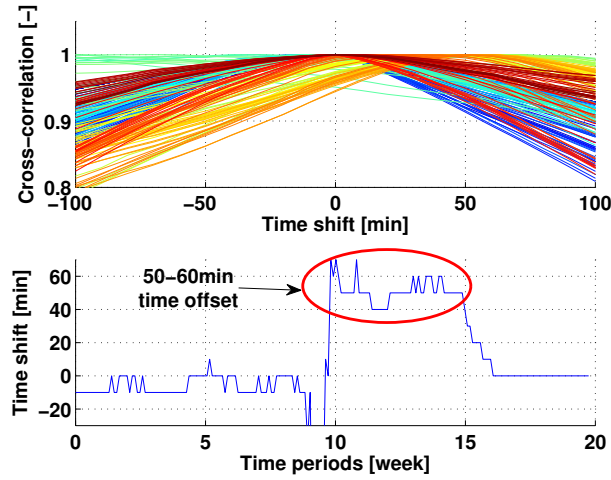
Figure C.4: Time offset found in a wind farm by comparing a nacelle anemometer and a met.mast anemometer. The top plot is the cross-correlations between the two signals. The bottom plot is the time history of the cross-correlation peak location, indicating the time offset. The signals are 10-min means, therefore, the cross-correlation precision is 10 min, which explains the spikes. There is a clear time offset of 50–60 min during 5 weeks.

For example, wind turbines, when they are not externally controlled, have usually a rather predictable control algorithm. In most cases, there is a clear correlation between some of the main sensors (e.g. Power, RPM, Pitch angle can all be reduced to a function of wind speed).
If there is a sensor that suddenly loses this correlation, the chances are that the sensor has failed or that the external conditions are no longer "normal" (e.g. exceptional wind condition, wind turbine shut down).

The challenge is, therefore, to determine a set of robust rules that associate each kind of sensor with its neighbouring sensors. Depending on, which rule is violated, an action is determined. For example, not using the sensor or using an estimate of the sensor based on its neighbouring sensors. Individual power curves based on the nacelle wind speed for each individual wind turbine can be used to qualify the power recordings or to eliminate outliners (e.g. start/stop sequences, anemometer errors).. First generation rules for screening wind speed measurements have been formulated in [3].

Met. Mast Anemometer

Anemometers mounted on met.masts are meant to record the local wind speed yet might experience systematic bias under specific conditions. It is, therefore, interesting to determine when those conditions occur and to adopt an appropriate mitigation method.

One of the most important issues with met.mast anemometry is caused by the met.mast itself. If the anemometer is not mounted according to the standards [1], the anemometer might be systematically biased. For a data analyst who does not have access to the site, it is difficult to estimate when this occurs. The best way is to compare to different wind speed recordings mounted on the same met.mast or at different locations and mounted in a different fashion.

Even if the anemometer is mounted according to the standards and if the anemometer is not mounted at the top, some wind directions yield a configuration where the anemometer is downstream of the tower. As it was described in the Wind direction offset Section, this phenomena can easily be determine by plotting the turbulence intensity with respect to the local wind direction. The peak indicates the wind direction angle where the wind speed measurements are affected by the met.mast tower shadow. In these wind directions it is preferable to use another anemometer on the same mast, at the same height and not located in the tower shadow.

Cup anemometers are instruments with a rotating part. The grease or oil used to enhance this motion naturally introduces a viscous moment opposite to the motion. The recordings are calibrated in a wind tunnel or in a met. test station to partly estimate this viscous moment. The problem is that the oil or grease used in the anemometer has a viscosity property dependent to the temperature and humidity. For example, under cold conditions the anemometer become iced and can completely stop working. These events can be spotted using the temperature sensor.

Other important failure types is lightning strikes, which can partly damage the bearings, yet such errors can be very difficult to identify. A proper data screening procedure is needed [3].

When a met.mast anemometer recording cannot be trusted, we recommend using the information from the other met.mast anemometers to estimate the correct wind speed information. At the sites we considered the terrain effects were minimum and the undisturbed wind profiles are modelled relatively easily using the surface roughness and standard atmospheric stability parameters. In those cases, when only one anemometer failed it was possible to estimate the measurement using an interpolation of the wind profile given by the other anemometers mounted on the same met mast.

The main difference is that their recordings are not influenced on such a big scale.

Met. Mast Wind Direction

Most of the recommendations above for anemometers are also valid for wind vanes. Measurements are also influenced by the met.mast itself, how they are mounted on it and the ambient temperature. Extreme temperatures may alter the wind vane reaction speed.
Spotting the met.mast shadow is also a bit more difficult. One way could be to try to see if there is a clear peak on the wind direction standard deviation when plotted against the wind direction. If this was not the case, we assumed that the wind direction sensor could be trusted even under the mast shadow.

When a wind direction sensor fails, we suggest to use the combined information from different wind vane sensors located on the same met.mast, or at a close distance. During this process it is important to keep in consideration that the wind speed is height dependent.

Wind Turbines Main Operational Sensors

The main operational sensors that are generally accessible on modern turbines are:

- Electrical power output

- Rotor rotation per minute (or eventually high speed shaft rotation per minute)

- Blade pitch angle

- Nacelle yaw direction (or yaw misalignment combined with the wind direction)

- Nacelle anemometer

- Eventually some strain gages to measure loads on different parts of the turbine (blades, tower, shaft)

The wind turbine control system of most modern wind turbines can be simplified on a 10-minute period to a simple relationship between the inflow wind conditions and all the operational sensors. However, because of the wake effect, the wind turbines inside a wind farm see a large variety of incoming flow conditions. In order to detect a sensor failure, it is ideal to know the complete incoming wind speed profile and to conduct a simulation of the wind turbine associated behaviour. Unfortunately, in most cases, there is only a nacelle anemometer (placed downstream of the rotor) and a

yaw sensor to estimate those different kind of inflow wind profiles. Nonetheless, we found that it was in most cases acceptable to use only the nacelle anemometer to generate a robust sensor curve. By using a sensor curve with respect to the nacelle anemometer, with an appropriate error acceptance, is is possible to effectively spot the exceptional events when the sensor (or the nacelle anemometer) is not recording a normal condition.

When one of the sensors on the wind turbine indicates a potential failure, the safest action is to ignore the specific 10-minute data, as there are good chances that they indicate a time when the wind turbine did not operate under normal conditions. However, if this represents a significant amount of data, it might be necessary to determine if this is indeed a recording failure and that the wind turbine was actually operating normally. In this case it is better to deactivate the pre-filter based on this sensor during a manually set time period.
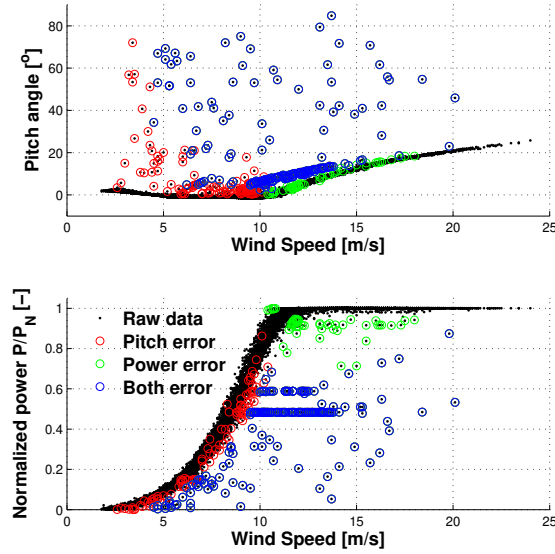

Figure C.5: Outliers on the pitch and power curves. The outliers are found by computing the distance between the point and the corresponding averaged value. Some outliers on one curve are not found on the other curve.

Note that this method is not sufficient to filter out the cases when the wind turbine is externally controlled, for example when the grid operator wants to reduce the power fluctuation on its network. If the wind turbine is systematically externally controlled, the original sensor curve might be completely blurred by the external control. In that case it is necessary to

have an indication of when the external control happens.

Fig. C.5 illustrates this method on the pitch and power curve of a wind turbine in the middle of an offshore wind farm. Some of the outliers found with one curve are not found on the other curve.
The outliers spotted in this example represents roughly one percent of the wind turbine data, when the wind turbine works without external control. However, as each of the wind turbine operates to a large extend independently, applying this criterion to the whole wind farm can reduce dramatically the amount of data remaining. For example, the probability that 100 wind turbines operate under optimum conditions at the same time, when each turbine has a reliability of 99% is $P = 99\%^{100} = 36.6\%$. For this reason, it might not be the best solution to apply this method on all the turbines at the same time.

C.3 Conclusion

Different methods have been presented in order to reinforce and to organize a wind farm dataset. Such methods are particularly adapted to wind farm wake analysis and wind farm performance estimation.
The methods have been applied with success on several wind farm datasets. As the different sensors have independent probability of failure, the added probability that all the sensors operate under normal conditions at the same time becomes very unlikely as the number of wind turbine and met.mast considered increase. A compromise has, therefore, to be made between the quality and the quantity of data considered for the analysis.

D

A CFD Model of the Wake of an Offshore Wind Farm: Using a Prescribed Wake Inflow

P-E Réthoré[1,2,3]**, A Bechmann**[1]**, N N Sørensen**[1]**, S T Frandsen**[1]**, J Mann**[1]**, H E Jørgensen**[1]**, O Rathmann**[1]**, S E Larsen**[1]
[1] Wind Energy Department, Risø National Laboratory, Denmark Technical University, Roskilde, Denmark
[2] Civil Engineering Department, Aalborg University, Denmark
[3] pire@dtu.risoe.dk

Abstract

An CFD model of the wake of an offshore wind farm, expanding existing measurements is proposed. The method is based on solving the Navier-Stokes Equations in a large domain downstream an offshore wind farm. The inflow of the domain is estimated using existing met mast measurements from both free stream and directly in-wake conditions. A comparison between the simulation results and measurements from a met mast are presented and the shortcomings of the methods are discussed.

D.1   Introduction

The extension of two existing offshore wind farms, Horns Rev and Nysted, are currently planned in Denmark. These new extensions might be built at a relatively short distance from the original ones (less than 20 km), which causes two problems. What will be the wind power resources available for the new wind farm and how will the new wind farm affect the wind power resources of the original wind farm? To address these questions, there is an urgent need for a large offshore wind farm wake model applicable in those situations.

In this context several approaches are simultaneously investigated at Risø-DTU [38]. This article focuses on a method extending the data available from the existing wind farms, using a CFD analysis. The outcome of this method is meant to give extra information to calibrate engineering models, which can then be used in a systematic way.

The basic idea of the method presented here is to estimate the wind properties at the exit of a wind farm and to model the development of the wake downstream of the wind farm. The key element is how to specify the wind farm wake correctly at the computational inlet. The procedure followed is to use the measurements of two met masts placed at a relatively short distance from the farm, one in the free stream; and one directly downstream of the park. The free stream mast is used to define the region of the inlet, where the wind is undisturbed by the wind farm and the downstream met mast is used to model the wake region of the inlet.

The two offshore wind farms Horns Rev and Nysted were used as test cases as they both present a similar cluster and measurement mast setup. Because of confidential restrictions, only the results from Horns Rev are presented.

D.2 Method

D.2.1 Methodology

The method is meant to extend the available information from the existing wind farms to calibrate offshore wind farm downstream-wake engineering models. The data set available includes 3 meteorological masts surrounding the wind farm (one at a corner and two aligned with a row of turbines, see Fig. D.1). The two aligned masts give an idea on how the wind recovers from the influence of the wind farm, yet with only two locations, no trends can be seen. The idea is to use these two met masts to extrapolate a trend of the wind speed recovery downstream of the wind park.

A steady Computational Fluid Dynamics (CFD) code is used to model the wind exiting the wind farm. The domain modeled begins at the location of the first met mast downstream of the park and encompasses a large region downstream of the wind farm, including the second met mast (see Fig. D.1). The turbulence model used is the k-ε model, which implies that the inputs needed at the inlet are the mean wind speed Umean, turbulent kinetic energy k and dissipation distribution ε, the free stream friction velocity u^* and the roughness coefficient of the sea z_0. All these parameters are estimated from the met masts measurements whenever it is possible, or, otherwise, derived from physical considerations.
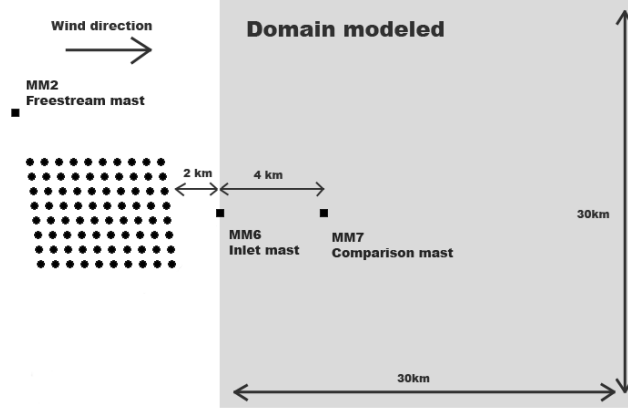
Figure D.1: Model setup.

D.2.2 Navier-Stokes Solver

The Navier-Stokes solver used is EllipSys, an in-house (Risø-DTU) CFD code under development for the last 15 years [89, 62]. The EllipSys3D code is a multiblock finite volume discretization of the incompressible RANS Equations. The approximations of the Reynolds terms are done using the first-order two-equations k- model originally introduced by Launder and Spalding [50]. The set of constants used in atmospheric conditions are given by Panofsky and Dutton [64]. The solver is used in steady state mode.

The main advantage of using such turbulence model is that it does not require a very fine mesh to resolve the flow near a wall. On the other hand, this model is also known to have a limited accuracy in boundary layers cases with adverse pressure gradient [98]. This aspect was nonetheless assumed to be negligible compare to the scale of the domain. Another potential limitation of this model is coming from the assumption that the eddy-viscosity is proportional with height in sheared flows. The effect of the eddy-viscosity on the development of a wake needs further investigation.

D.2.3 Computational Mesh

Two types of meshes are considered, a 3D mesh of 30 km × 30 km × 1.2 km (around 4,000,000 points) and a 2D mesh of 30 km × 1.2 km (around 300,000 points). In order to obtain a satisfying convergence speed, the mesh was stretched to obtain the highest precision at the location of the highest gradients. One of the key restrictions concerning the design of the mesh is the size of the cells close to the wall boundary, which needs to be of the same order of magnitude as the roughness length of the sea z_0.

D.2.4 Boundary Conditions

The side BCs are taken as symmetric, while the top BC is taken as an inlet boundary and the bottom as a wall boundary with a no-slip condition. As previously mentioned, the inlet boundary is composed of two main regions, a free stream region, where the flow is assumed to be undisturbed by the wind farm and a wake region (see Fig. D.2). The wake region is defined as a rectangle of 5 km of width and 200 m of height. In addition a linear transition region of 100 m around the wake region is applied to smooth the resulting shear forces generating by the difference of wind speed from one region to another.
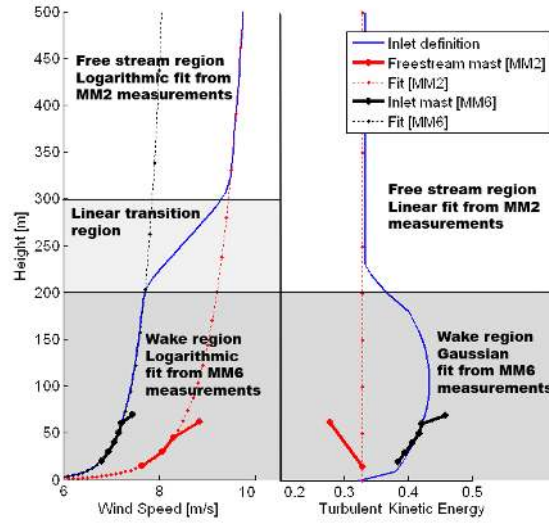
Figure D.2: Inlet specification.

The free stream region is defined in terms of mean flow velocity, turbulent kinetic energy and dissipation. It is based on the requirements necessary for obtaining a balanced logarithmic profile using the k-ε turbulence model. The mean velocity is, therefore, a logarithmic profile, while the turbulent kinetic energy is kept constant and the turbulent dissipation is inversely dependent of the height,

$$U_{mean} = \frac{u^*}{\kappa} \ln\left(\frac{z}{z_0}\right), \quad k = \frac{u^{*2}}{\sqrt{C_\mu}}, \quad \varepsilon = \frac{u^{*3}}{\kappa z}, \tag{D.1}$$

where U_{mean} is the mean axial velocity, κ is the von Kármán constant, z is the elevation, z_0 is the roughness length of the sea, u^* is the friction

velocity, k is the turbulent kinetic energy, ε is the turbulent dissipation and C_μ is a constant of the k-ε turbulence model. In order to determine the appropriate roughness length z_0 and the friction velocity u^*, measurement data from the free stream mast is fitted for a prescribed wind speed bin. In the case of the wind farm wake region, this inflow definition is modified in order to account for the wake inflow. The mean velocity at the downstream mast is found to be logarithmic and a new set of friction velocity u^* and roughness length applied in the mean velocity formula. The turbulent kinetic energy profile can be estimated from the met mast measurements of the wind speed fluctuation (i.e. the standard deviation of the wind speed during a 10-minute period). This is done under an assumption of neutral boundary layer stratification and using the similarity relationship lists given by Stull [91], which gives an empirical relationship between the different components of the wind fluctuations u', v' and w' and the friction velocity u^*,

$$\frac{\overline{u'^2}}{U^{*2}} = 6.1, \quad \frac{\overline{v'^2}}{U^{*2}} = 2.9, \quad \frac{\overline{w'^2}}{U^{*2}} = 1.7, \tag{D.2}$$

which gives a relationship between u', v' and w'.

$$v'^2 = 0.48 u'^2, \quad w'^2 = 0.24 u'^2. \tag{D.3}$$

The available measurements are recorded using standard cup anemometers, which are mainly influenced by the horizontal components of the wind velocity u and v. It is, therefore, assumed that the measured standard deviation σ_m can be expressed as

$$\sigma_m = \sqrt{u'^2 + v'^2}. \tag{D.4}$$

Using the relationship given by Stull between u' and v', the measured wind fluctuations are then

$$u'^2 = 0.68 \sigma_m^2. \tag{D.5}$$

Finally, the turbulent kinetic energy k can expressed as

$$k = \frac{1}{2} \left(u'^2 + v'^2 + w'^2 \right) = 0.88 u'^2 = 0.60 \sigma_m^2. \tag{D.6}$$

This relation is only valid in an undisturbed atmospheric flow, where the vertical fluctuations are relatively small compared to the two other components. In a wake situation this balance is changed and the turbulence is believed to be more isotropic. It is nonetheless difficult to say how this turbulence distribution is evolving in the wake, which makes it difficult to compare wind speed fluctuation measurements with the CFD results that

only give an estimate of the turbulent kinetic energy k. Ideally one would need more precise measurements of all the components of the wind speed fluctuation at different heights to have a more reliable comparison data set. As the met masts only give measurement until hub height, some extra assumptions have to be taken considering how to match the free stream and the wake profile. The assumption taken was to fit a Gaussian distribution, centered around hub height, over the turbulent kinetic energy profile, derived from the measurements. This solution is not based on any physical evidence and is, therefore, expected to have a significant influence on the validity of the results. Finally the turbulent dissipation was kept to the same as in the free stream region. Again, this choice is not expected to be realistic, yet without any proper measurement of turbulence, or a physical model of the wind farm wake region, it was found to be the most appropriate solution.

D.3 Measurements

Horns Rev is an offshore wind farm located on the west coast of Denmark. It is composed of 80 Vestats V80 2 MW turbines arranged in a cluster of 10×8 (see Fig. D.1). The measurements available are recorded at three locations around the wind farm. The met mast MM2 is used as the free stream reference wind speed, while the met mast MM6 is used as the wake region reference, for constructing the inlet profile. The met mast MM7, 4 km downstream MM6, is used to compare to the results of the method.
The reference wind direction chosen was $270° + / - 3°$, which is the direction angle of the row of turbines for the west wind direction. The two downstream masts are also aligned on this direction, yet not directly in line with a row of turbine. The reference hub height wind speed chosen is 8.5 ± 0.5 m/s.
The measurements from the top anemometer in each 3 masts deviate with the rest of the anemometers. This effect is believed to come from the met mast geometry. These anemometers are, therefore, excluded from the curve fitting. The mean wind speed profiles are fitted using the logarithmic law (Eq. (D.1)) in order to extract the roughness length z_0 and the friction velocity u^*. The values found for the free stream profile are in agreement with the logarithmic law defined in the k- model, (see Eq. (D.1)) with an atmospheric set of constants ($C_\mu = 0.03$).

D.4 Results and Discussion

The 2D results are similar to the 3D results in the center plane of the domain. This indicates that most of the recovery of the wind farm wake is done from a transfer of momentum from the top. There is nonetheless also a horizontal recovery done on the side of the wake region, which is of smaller

influence. As a consequence, the spreading of the wake cross sectional profile are not following a Gaussian shape as it is usually seen in wake situations, with rectangular inflow profile (see Fig. D.5). The vertical mean wind speed distribution 4 km inside the domain is in good agreement with measurements (see Fig. D.6).
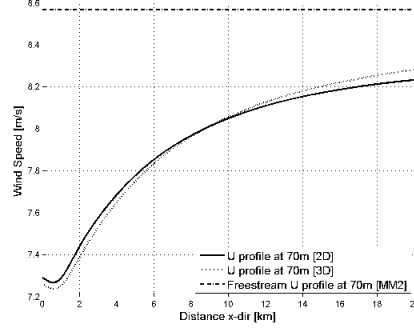

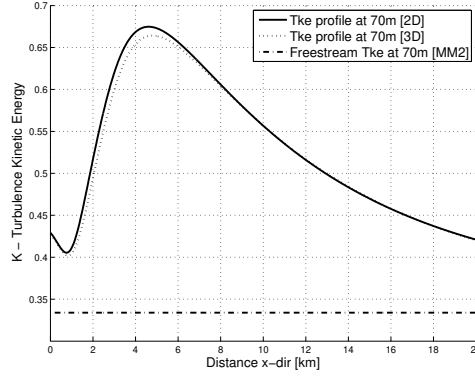**Figure D.3:** Mean velocity horizontal profile in the center plane at hub height (70 m).

Figure D.4: Turbulent Kinetic Energy horizontal profile in the center plane at hub height (70 m).

On the other hand the turbulence profile is largely different from the measurements (see Fig. D.7). In addition the expected trend of the turbulence would be to decrease constantly instead of increasing as in Fig. D.4. This turbulence plot clearly shows the weakness of this model. As there is no physical model of the balance between mean wind speed profile and turbulence profile at the inlet, the arbitrary wind shear of the transition region yields a dramatic increase of the turbulent kinetic energy and dissipation
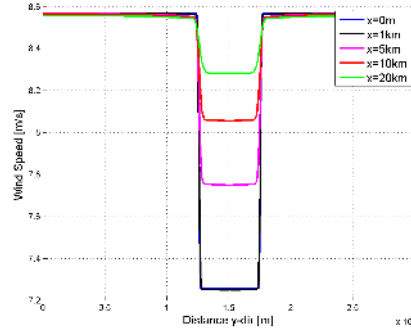
until they reach a balance and begin to decrease.

Figure D.5: Mean wind speed horizontal profile at hub height (70 m).

The horizontal evolution of the mean wind speed at hub height is converging asymptotically to a constant value (see Fig. D.3). This value, significantly lower than the free stream hub height wind speed, is linked to the ratio between the height of the domain considered and the wake region height, because of the conservation of mass and momentum in the domain considered. Increasing the height of the domain would also increase this value, making it converge to the free stream value. The height of the domain is nonetheless limited by the height of the planetary boundary layer (around 1000–1500 m).
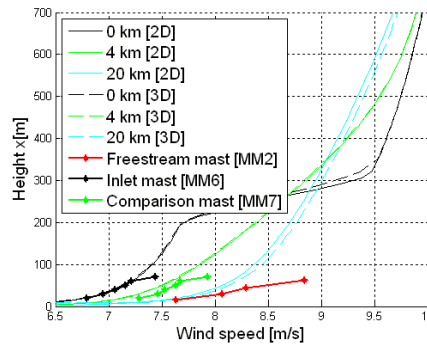

Figure D.6: Mean wind vertical profile in the center plane of the domain.
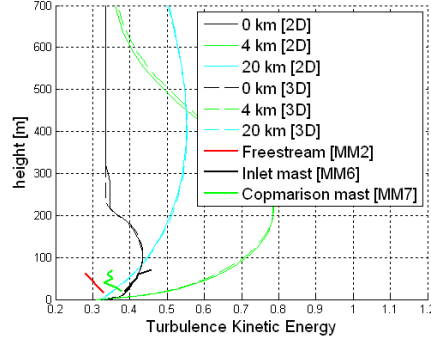
Figure D.7: Turbulent kinetic energy vertical profile in the center plane of the domain.

D.5 Shortcomings and Limitations of the Method

The rate of the wake recovery is directly dependent on the prescribed turbulent kinetic energy and dissipation. While the first one can be partly estimated from the available measurements, the second is totally unknown and requires a more detailed description.

Similarly, the transition region, defined as linear, is also unphysical. This high velocity gradient generates a high shear directly responsible for the unrealistic increase of turbulent kinetic energy that can be seen on Fig. D.4. In order to avoid this jump, this transition region also needs a better specification of the turbulence profile.

For these reasons, without a proper physical wake definition of a wind farm, or more detailed information on the flow leaving a wind farm, the method still needs further investigation to obtain reliable results.

D.6 Conclusion

A method to extend the measurement downstream an offshore wind farm is presented. Nonetheless the information needed as inputs are far too demanding compared to the available data sets. In consequence, without a more detailed setup and without a proper wind farm/ boundary layer model, this method cannot be used to give satisfying results.

In order to palliate this issue, a CFD model of an offshore wind farm wake, including the wind farm, is currently in development. This method, modeling the wind turbines as actuator discs, will hopefully reduce the amount of input necessary to extend the available measurements. The end goal of this method is to assist the development of an analytical expression of an offshore wind farm wake.

Acknowledgements

Recent publications in the DCE Thesis Series